# Experimental study on deep steel-concrete composite slabs using distributed strain measurements

Luc Gouw

Delft University of Technology

# Experimental study on deep steel-concrete composite slabs using distributed strain measurements

By

Luc Gouw

In partial fulfilment of the requirements for the degree of:

**Master of Science**
in Civil Engineering

at the Delft University of Technology,
to be defended publicly on Wednesday November 6, 2024 at 11:00 AM

| | | |
|---|---|---|
| Supervisor: | Prof. dr. ir. M. Veljkovic, | TU Delft (chair) |
| Thesis committee: | Dr. ir. F. Kavoura, | TU Delft |
| | MSc. Y. Zhang | TU Delft |
| | Dr. ir. Y. Yang, | TU Delft |
| | Ir. M. Koetsier, | TU Delft |

# Preface

This thesis investigates the structural performance of deep steel-concrete composite (SCC) slabs, while focussing on distributed strain measurements using distributed optical fibers. By analysing strain distribution, neutral axis position, buckling behaviour, and crack detection of SCC slabs, this research aims to expand the understanding of composite slab behaviour.

I was drawn to the research topic due to the innovative use of distributed optical fibers in SCC slabs. Integrating optical fiber technology in traditional construction methods promises to yield innovative insights. Another aspect that interested me was working on large-scale experiments in the lab, which provided a unique opportunity to apply theoretical knowledge in a practical environment. This allowed me to observe the behaviour of steel-concrete composite slabs under controlled testing conditions.

The research journey presented various technical challenges, including applying optical fibers to the steel sheeting and achieving consistent strain measurements throughout multiple testing stages. Through these obstacles, I gained valuable insights into large-scale experiments on SCC slabs and the practical applications and limitations of distributed optical fibers.

I would like to thank my thesis committee for their feedback and support in completing this thesis. A special thank you to Yufei who helped with the application process of the optical fibers which was a time-consuming process. I would also like to thank the staff of Stevin Lab II, who helped execute the experiments, and Mathieu who explained how to use the optical fibers.

# Abstract

Steel-concrete composite (SCC) slabs are extensively used in construction, particularly in multi-story buildings, due to their efficiency and structural performance. SCC slabs combine the strengths of steel and concrete, where steel provides tensile strength and concrete offers compressive resistance. This integration results in lightweight, robust structures that save costs and allow for taller buildings with larger spans.

New designs of steel-concrete composite slabs have to be extensively tested before the new designs are approved. It is therefore important that information is gathered during testing. Strain measurements are often done on composite slabs, for example, strain gauges have been applied to the steel sheeting and distributed optical fibers (DOFs) have been applied to the reinforcement rebars. However, there have never been distributed strain measurements on the steel sheeting of steel-concrete composite slabs. This research aims to gain new insights into the structural performance and behaviour of deep steel-concrete composite slabs using distributed strain measurements.

SCC slabs often have embossed regions of steel sheeting, these embossments or indentations transfer shear forces between the steel sheeting and the concrete. DOFs were applied on the embossed parts of the steel sheeting in the direction of the span in four composite slabs. The strain data showed oscillations in the strain values, and that the embossed/indented parts of the steel sheeting were in tension, while the flat areas were in compression. Local deformations, due to the geometry of the embossments, caused the oscillations.

The N.A. position was another critical focus of the study, which was determined using fiber data at five locations on the middle rib of three slabs. The N.A. was determined for three loading stages: initial, elastic, and plastic. The fibers captured the upward movement of the N.A. from the steel sheeting into the concrete during the initial and elastic stages, as expected according to theoretical calculations of the N.A. position. However, in the plastic stage, the N.A. shifted downward, back into the steel sheeting, instead of continuing its upward trajectory, as expected. This unexpected shift was attributed to partial shear interaction, where the steel sheeting and concrete began acting separately, leading to separate strain profiles.

Buckling of the steel sheeting was observed in two slabs, Slabs 10 and 11, with fibers providing critical insights into the timing and extent of buckling. In Slab 11, where four fibers were located in the buckling zone, two fibers showed early signs of buckling in the top flange at 97% and 98.3% of the peak load. The strain patterns indicated buckling before the peak load was reached, offering valuable data on the onset of this failure mode. For Slab 10, buckling was detected after the peak load.

Lastly, the research explored the use of DOFs for crack detection. Fibers were applied to the bottom of the ribs on one slab to identify crack locations based on strain data. While cracks typically cause localized peaks in strain, the results revealed limitations in the accuracy of crack detection using DOFs on steel sheeting.

In conclusion, this research demonstrates the potential of DOFs for strain measurement in steel-concrete composite slabs, offering valuable insights into strain distribution, N.A. position, and buckling behaviour. However, the crack detection capability of DOFs, particularly when applied to steel sheeting, requires further refinement to improve accuracy and reliability.

# Contents

# List of Figures

# List of Tables

# 1. Introduction

## 1.1. Relevance of Study

Steel-concrete composite (SCC) slabs are widely utilized in the construction industry due to their versatile applications and enhanced structural performance. These slabs are most commonly used as floor slabs in multi-story non-residential buildings, such as office buildings, commercial centers, and industrial facilities. The widespread adoption of SCC slabs is attributed to the advantageous composite interaction between steel and concrete, which enables efficient and lightweight structural designs.

The combination of steel and concrete in SCC slabs combines the strengths of both materials. Steel is renowned for its excellent tensile strength, making it an ideal choice for resisting tensile forces and providing structural ductility. Concrete, on the other hand, offers superior compressive strength, which is essential for withstanding compressive forces and distributing loads evenly. By integrating these materials, SCC slabs can achieve an optimal balance between tensile and compressive resistance, resulting in a robust and durable structural element.

In the construction of SCC slabs, the steel component serves multiple critical functions [1]. Firstly, it acts as formwork for the concrete during the casting process, eliminating the need for temporary formwork and thus reducing construction time and costs. Secondly, the steel provides additional reinforcement, enhancing the slab's overall load-bearing capacity and structural integrity. This dual functionality of steel in SCC slabs not only streamlines the construction process but also contributes to the long-term performance and sustainability of the structure. Furthermore, the composite nature of SCC slabs allows for more efficient material usage, resulting in lighter structures compared to traditional reinforced concrete slabs [2]. This weight reduction can lead to significant savings in foundation costs and enables the construction of taller buildings with fewer material resources. Figure 1.1 illustrates a typical steel-concrete composite floor slab and its components [3].

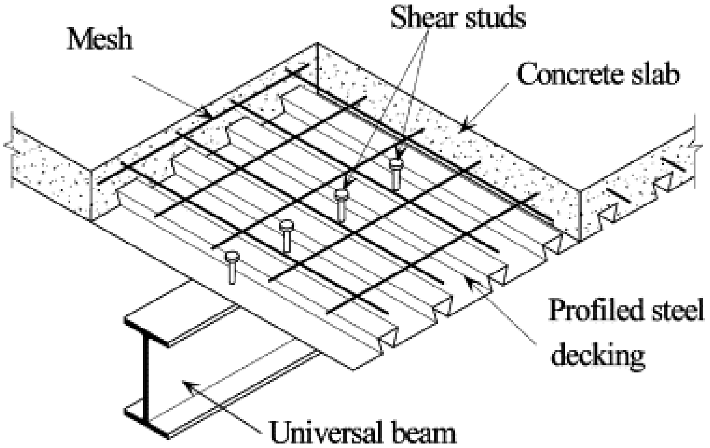

*Figure 1.1. Steel-concrete composite floor slab and its components [3].*

The composite interaction between steel and concrete presents several challenges that must be addressed to ensure the structural performance and safety of SCC slabs. Predicting and accurately modeling this interaction is complex due to the distinct mechanical properties of steel and concrete. According to Eurocode 4 [4], which provides guidelines for the design of composite steel and concrete structures, full-scale experiments are often required to verify the performance of new designs of steel sheeting. This requirement is particularly critical when calculating the longitudinal shear resistance of the slab, as the interaction between the steel and concrete under load is not straightforward to predict using theoretical models. When SCC slabs are subjected to loading, bending moments are induced, leading to the development of longitudinal shear stresses at the interface between the steel and concrete. These stresses can cause relative movement, or slip, between the two materials. To mitigate this slip and ensure the composite action, a longitudinal shear bond must be established. The longitudinal shear resistance of an SCC slab can be determined using the partial shear method or the m-k method, as outlined in Eurocode 4 [4]. To collect enough data for the partial shear method, at least four tests are necessary. Alternatively, the m-k method requires a minimum of six tests. These design verifications are explained in detail in section 2.1.4: Failure mechanisms. However, the design verifications of Eurocode 4 for SCC slabs are developed for shallow slabs [2], SCC slabs are classified as shallow if the height of the steel sheeting is less than 200 mm. Slabs with a height exceeding 200 mm are considered deep.

Consequently, the development and validation of new SCC slab designs can be relatively expensive and time-consuming due to the extensive testing required. Each test must be meticulously planned and executed to ensure that the results are reliable and applicable to real-world scenarios. Furthermore, these tests often involve large-scale setups that simulate actual loading conditions, adding to the overall cost and complexity. It is therefore important that as much insight is gained as possible from the experiments.

One key aspect is understanding the stress distribution throughout the slab. Stress data reveals which areas are under tension, which are under compression, and where and when the steel sheeting begins to yield, providing essential insights into potential failures. The transition from tension to compression occurs at the Neutral Axis (N.A.), Eurocode 4 [4] uses an estimated theoretical N.A. position for calculating failure modes. Comparing this theoretical N.A. position with actual test data could significantly enhance the accuracy of future designs.

However, stress cannot be measured directly, instead, it is calculated using strain measurements. Typically, strain is measured by strain gauges, which provide data at a single location. While effective, this method offers limited spatial information. An alternative technique is Digital Image Correlation (DIC), which measures strain across an entire surface by utilizing photogrammetry techniques. However, DIC is challenging to implement with deep SCC slabs due to the trapezoidal shape of the steel bottom, which complicates the application of this method. Figure 1.2 shows the application of three strain gauges on steel sheeting on the left and a surface that is prepped for DIC on the right.

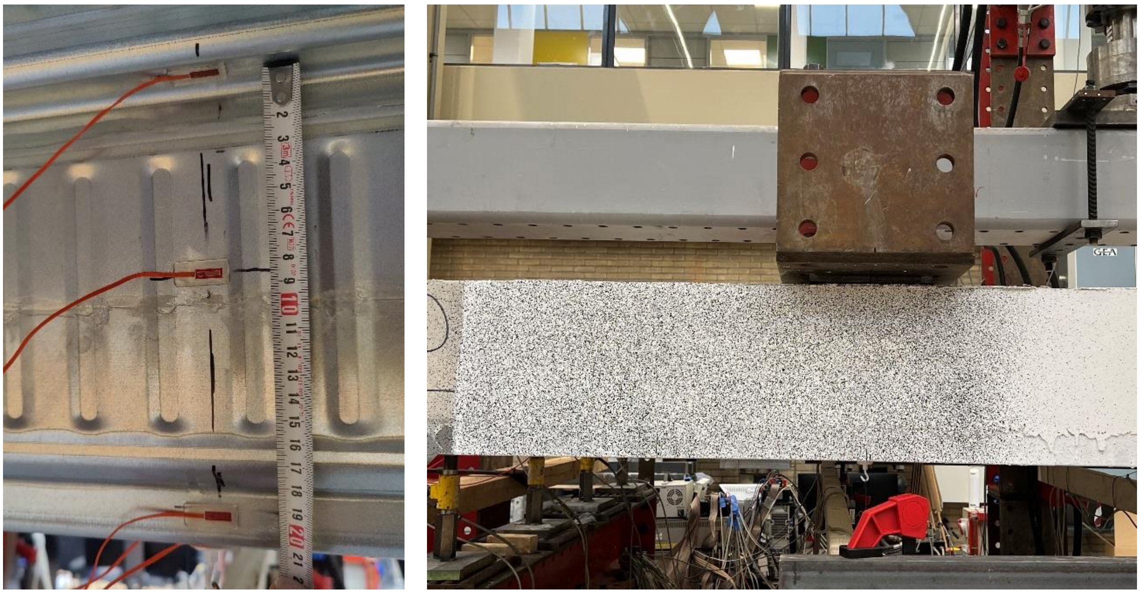

*Figure 1.2. Application of strain gauges (left), and a surface prepped for DIC (right).*

Alternatively, for this thesis, Distributed Optical Fibers (DOFs) will be employed to measure strain in multiple SCC slabs subjected to a four-point bending test. These fibers will be attached along the span of the steel bottom of the slabs. DOFs offer a significant advantage as they can measure strain continuously along the entire length of the fiber, with measurement points spaced as close as 0.65 mm apart. The fibers themselves are flexible and have a diameter of just 0.2 mm, making them suitable for installation in tight spaces.

DOFs have been successfully applied in various civil engineering applications, including steel-concrete composites. In prior research, DOFs have been embedded in or attached to steel reinforcement rebars to monitor strain [5]. Four different applications of the fibers applied onto a rebar have been illustrated in Figure 1.3 [5]. However, DOFs have never been applied directly to the steel bottom of an SCC slab. Applying fibers to the bottom of a slab is less complex than embedding them in or attaching them to a rebar. Additionally, connecting one end of the fiber to a measuring system is more straightforward when the fiber is on the exterior of the slab, reducing the risk of damage during concrete pouring and curing processes.

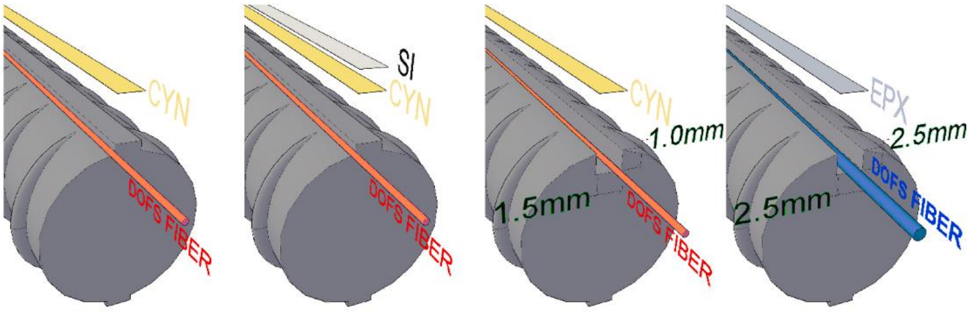

(a) (b) (c) (d)

*Figure 1.3. Application of Distributed Optical Fibers on reinforcement rebars [5].*

This innovative application of DOFs is expected to yield new insights into the behaviour of SCC slabs. By capturing detailed strain data along the steel bottom, it will be possible to get a better understanding of the composite action between steel and concrete, the development of stress under load, and the overall performance of the slabs. The spatial resolution provided by DOFs will facilitate a comprehensive analysis of strain distribution and structural responses, contributing valuable data for the optimization and design of future composite slabs.

## 1.2. Problem definition

New designs of steel-concrete composite slabs have to be extensively tested before the new designs are approved. It is therefore important that information is gathered during testing. Strain measurements are often done on composite slabs, for example, strain gauges are applied to the steel sheeting and distributed optical fibers (DOFs) have been applied to the reinforcement rebars. However, there have never been distributed strain measurements on the steel sheeting of steel-concrete composite slabs. Applying the DOFs on the steel sheeting could provide new insights into the structural performance and behaviour of composite slabs.

## 1.3. Research Objectives

The main objective of this thesis is to investigate the structural performance of deep steel-concrete composite slabs using distributed strain measurements on the steel sheeting, while focusing on four critical aspects: the strain distribution across embossed regions, the neutral axis position, the buckling behaviour, and the identification of concrete crack locations within the slab. The distributed strain measurements will be done by Distributed Optical Fibers (DOFs).

Firstly, this thesis aims *to analyse the strain distribution across the embossed regions* of the steel sheeting in steel-concrete composite slabs. Steel sheeting has embossments that transfer shear forces between the steel sheeting and concrete. Due to their geometry, the strain values in the embossed sections are expected to differ significantly from those in the flat areas of the steel sheeting. To accurately capture this strain behaviour, distributed optical fibers were applied to the embossed areas of the steel sheeting. This approach allows for a detailed examination of the strain distribution, helping to identify which regions of the embossments are under compression and which are experiencing tension.

The secondary aim of this thesis is *to determine the neutral axis position* within the composite slab using the strain data from the distributed optical fibers. The neutral axis is a fundamental concept in structural engineering, representing the line within the cross-section of a slab where the material experiences no longitudinal strain. Accurately determining the position of the neutral axis is crucial for analysing the bending behaviour and load distribution within the slab. The high-resolution strain data from the optical fibers will enable a precise calculation of the neutral axis, offering insights into the stress distribution and structural performance of the composite slab. The results from the strain data will be compared to theoretical calculations of the neutral axis at different load levels.

Another crucial aspect of this thesis is *to analyse the buckling behaviour* of the steel-concrete composite slab using strain data. Buckling is a critical failure mode for composite structures, especially under compressive loads, and understanding its onset and progression is essential for ensuring structural safety. The distributed nature of the optical fibers allows for the capture of strain variations over large areas, providing a comprehensive view of how the slab deforms under load. By correlating these strain measurements with the slab's load-bearing behaviour, this research aims to develop a better understanding of the buckling phenomena in composite structures.

Lastly, this thesis aims to utilize distributed optical fibers *to find the locations of concrete cracks* within the composite slab during loading. Concrete cracks cannot be detected visually during the testing of the slabs since the bottom is covered in steel sheeting. Distributed optical fibers can monitor strain along their entire length, if the cracks locally increase the deformation of the steel sheeting, then the fibers can detect the cracks. By applying these sensors to the composite slab, this research aims to enhance the detection and mapping of cracks inside the slab, thereby facilitating more effective maintenance and repair strategies.

## 1.4. Research Questions

Main Question:

*What insights into the structural performance of deep steel-concrete composite slabs can be found by distributed strain measurements on the steel sheeting during loading?*

The main research question will be answered by the following sub-questions:

- *What is the strain distribution across the embossed regions, how does it differ from flat parts of the steel sheeting, and what causes these differences?*
- *What is the position of the neutral axis of the slabs at different stages during loading, and how does it compare with theoretical predictions of the neutral axis position?*
- *At what point during loading is buckling of the steel sheeting detected?*
- *What are the locations of the concrete cracks, and how do they propagate through the slab?*

## 1.5. Report Structure

Chapter 2 provides a literature review, offering background information on steel-concrete composite slabs and distributed optical fibers. It also explores the current state of research in both fields, highlighting the latest advancements and applications.

Chapter 3 details the experimental setup used for the study. This chapter covers the location, preparation, and application of the optical fibers, ensuring a clear understanding of the methodology behind the experiments.

Chapters 4 through 7 present and analyse the results, addressing the research questions posed in this thesis. Each chapter discusses the findings in-depth, providing insights into the behaviour of the materials under investigation.

Lastly, Chapters 8 and 9 give a discussion, summarize the conclusions drawn from the research, and offer recommendations for future work, based on the outcomes of this study.

# 2. Literature review

## 2.1. Steel-concrete composite slabs

To provide a foundation for the topics discussed in this research, it is essential to understand steel-concrete composite (SCC) slabs. SCC slabs are a widely used structural system in modern construction, known for their efficiency, strength, and versatility. These slabs combine the tensile strength of steel with the compressive strength of concrete, resulting in a highly effective and adaptable construction method. These slabs consist of a combination of reinforced concrete and steel sheeting, the main components can be seen in Figure 2.1 [3].

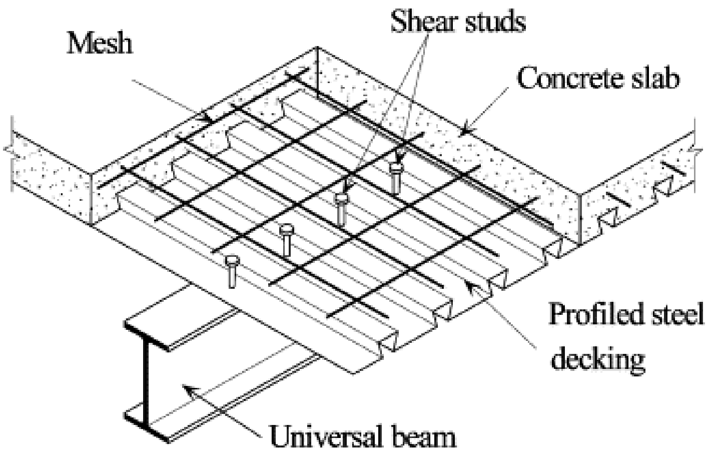

*Figure 2.1. Steel-concrete composite floor slab [3].*

### 2.1.1. Materials

**Profiled steel sheeting**

The profiled steel sheeting is cold-formed and zinc-coated. Steel grades from S280 to S450 are available, but S350 is most commonly used [6]. Buckling is a critical issue for steel sheeting in steel-concrete composite slabs because it can compromise structural integrity and load-bearing capacity. Under compressive stress, the thin steel sheets may deform laterally, leading to failure. The steel sheeting is mostly in tension, however, the top of the steel could be in compression. To increase the resistance to buckling, stiffeners can be made in the steel sheeting. The stiffeners are the small dents which are highlighted in Figure 2.2 [6].

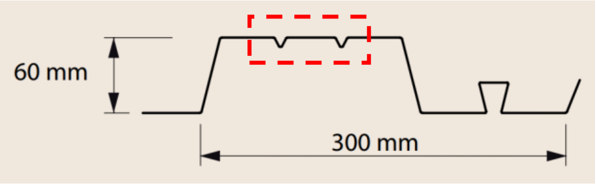

*Figure 2.2. Steel sheeting profile [6].*

After production of the profiled steel sheeting, it can be transported and installed on the construction site. The installation of the sheets is relatively easy due to their low weight, up to 400 m$^2$ can be installed a day [1]. There are two main shapes of steel sheeting, re-entrant sheeting and trapezoidal sheeting. These are shown in Figure 2.3 [2].

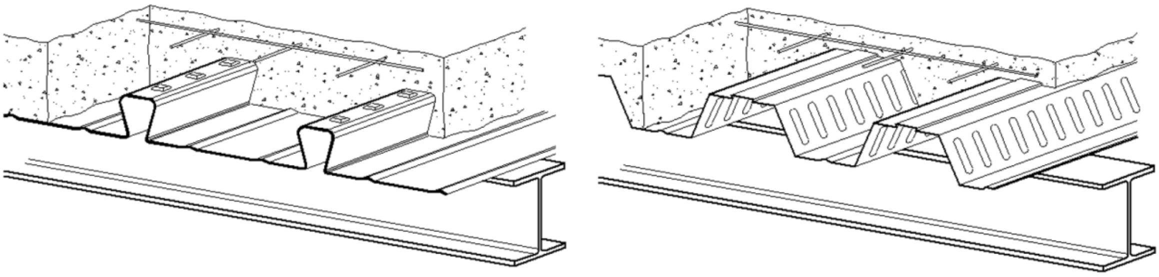

*Figure 2.3. Re-entrant (left) and trapezoidal (right) steel sheeting [2].*

There are numerous possibilities for the geometries of steel sheeting used in composite slabs, with the selection depending on factors such as the span and the desired height of the slab. According to Eurocode guidelines, the minimum height of a composite slab is 80 mm, and the height of the concrete above the steel sheeting must be at least 40 mm [4]. While the Eurocodes provide these minimum requirements to ensure structural integrity, they do not specify an upper limit for the height of the slab, allowing for flexibility in design to meet specific project needs.

Steel sheeting is considered deep when the height of the sheeting exceeds 200 mm [2]. This classification is important because increasing the depth of the steel sheeting can significantly enhance the structural performance of the slab. Deeper steel profiles can support longer spans, reducing the need for intermediate supports and allowing for more open and flexible floor plans in building designs. This capability is particularly beneficial in large-scale commercial or industrial buildings where unobstructed space is a key requirement.

**Reinforced concrete**

For SCC slabs normal concrete and lightweight concrete can be used. Lightweight concrete offers a weight reduction, thus longer span could be achieved. However, it also has a lower modulus of elasticity than normal concrete which causes larger deformations [7]. According to Eurocode 4 section 3, normal concrete strength classes C20/25 to C60/75 and lightweight concrete strength classes LC20/22 to LC60/66 can be considered for the design of composite structures [4].

Concrete has low tensile strength compared to steel. The steel sheeting at the bottom of the composite slab takes on the tensile forces in the slab, but there is also reinforcement needed in the transverse and longitudinal direction, according to Eurocode 4 [4]. This is often done with a mesh, this can be seen in Figure 2.1. The mesh is needed for crack control and is always located at the top of the slab, above the steel sheeting. Additional reinforcement could be applied inside the rib to improve fire resistance or to increase the resistance to a concentrated load [8].

The concrete can be cast onto the steel sheeting at the construction site, the steel sheeting acts as formwork, this can be seen in Figure 2.4 [1]. During the casting process, the steel sheeting has to bear the weight of the concrete as it is poured and set. There is no composite interaction between the steel and concrete until the concrete hardens.

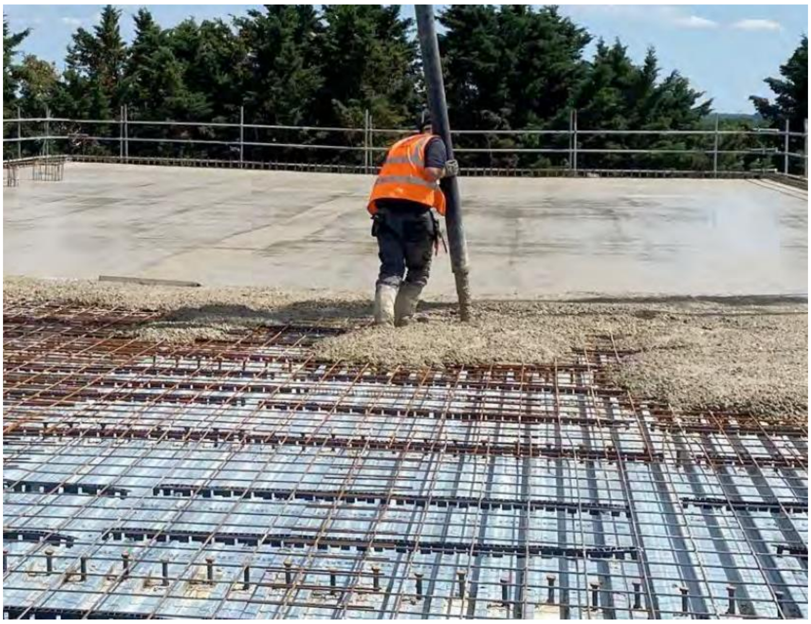

*Figure 2.4. Concrete poured onto the steel sheeting [1].*

### 2.1.2. Advantages and disadvantages

The following points are the advantages of steel-concrete composite slabs [1] [8].

- Speed of construction: The steel sheets are relatively low weight and can be installed by hand. Moreover, they serve as formwork for the concrete, eliminating the need for additional formwork, thus saving considerable time. With minimal reinforcement requirements, the production speed is further enhanced.
- Safety: The steel sheeting serves as a stable platform for workers to stand on, enhancing safety.
- Weight saving: The SCC slabs have a good effective cross-section, providing comparable strength and stiffness to various other floor systems while being lighter in weight. This results in an overall lighter structure, allowing for potential reductions in certain structural elements and leading to cost savings.
- Easy transport: The steel sheeting is light and can be packed together in bundles which means one lorry can transport up to 1000 $m^2$ of steel sheeting. The concrete can also be transported relatively easily but this is similar to other floor systems which utilise in-situ casting. However, it is significantly easier to transport than prefabricated concrete.
- Structural stability: During construction, the steel sheeting can as lateral restraint when properly connected to the beams and if the ribs run transversely. In the completed structure, the composite slab can act as a diaphragm.
- Easy installation of services: Installation of cables, pipes, and false ceilings can be conveniently attached to the steel sheeting using hangers.

The following points are the disadvantages of steel-concrete composite slabs [1] [8].

- One-way span: SCC slabs have ribs in one direction which makes it strong and stiff in this direction, but weak in the transverse direction. This makes the SCC slabs essentially a one-way slab.
- Low hogging bending moment resistance: The hogging bending moment occurs when there is a continuous floor over a support. In this scenario, the tensile forces occur at the top of the slab, rather than at the bottom. Since the steel sheeting is positioned at the bottom of the slab, the

reinforcement within the concrete must bear the tensile forces. This is undesirable as the reinforcement at the top of the slab would need to be increased.

### 2.1.3. Composite behaviour

Composite structures or elements are made from two or more materials with significantly different properties. In steel-concrete composite slabs, these materials are concrete, steel reinforcement bars, and steel sheeting. Due to their different properties, the materials can complement each other. For example, concrete has low tensile strength but high compressive strength, whereas steel possesses high tensile strength. By using steel reinforcement, the steel can withstand the tensile forces while the concrete bears the compressive forces. In steel-concrete composite slabs, shear forces are transferred between the concrete and the steel sheeting. Transferring shear forces between the concrete and steel sheeting can be done in several ways. Eurocode 4 gives 4 different types of shear connections, which are listed below, and illustrated in Figure 2.5 [4].

- 1: Mechanical interlocking due to deformations in the steel sheeting (embossments).
- 2: Frictional interlocking due to the re-entrant form of the profiles.
- 3: By end anchorage which is provided by either shear studs or another form of connection between the steel sheet and concrete. This shear connection is only applied in combination with option 1 or 2.
- 4: By end anchorage provided by deforming the ribs at the end of the span. This shear connection is only applied in combination with option 2.

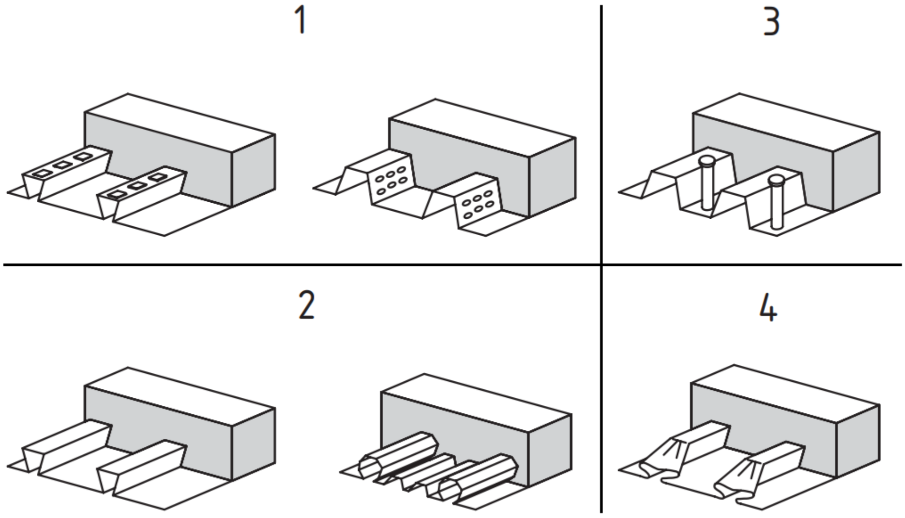

*Figure 2.5. Types of shear connection [4].*

### 2.1.4. Failure mechanisms

There are three failure mechanisms for steel-concrete composite slabs [9];

- Flexural failure
- Vertical shear failure
- Longitudinal shear failure

The following sections provide a detailed examination of these failure modes.

### *2.1.4.1. Flexural failure*

Flexural failure occurs when the ultimate bending moment capacity is reached. There are two bending moments, positive and negative. The positive bending moment is also referred to as sagging bending moment, this is due to the compression forces occurring at the top of the slab and the tensile forces occurring at the bottom of the slab. For simply supported slabs, only sagging bending moments occur. The negative bending moment is referred to as the hogging bending moment, which can occur if a slab is continuous over a support. Section 9.7.2 of Eurocode 4 gives formulas to calculate the sagging bending moment resistance of the slab [4]. The concrete above the neutral axis bears the compression forces, while the steel sheeting and reinforcement rebars below the neutral axis bear the tensile forces. Figure 2.6 [4] can be used to calculate the sagging bending moment resistance $M_{Pl,Rd}$ If the neutral axis is above the steel sheeting.

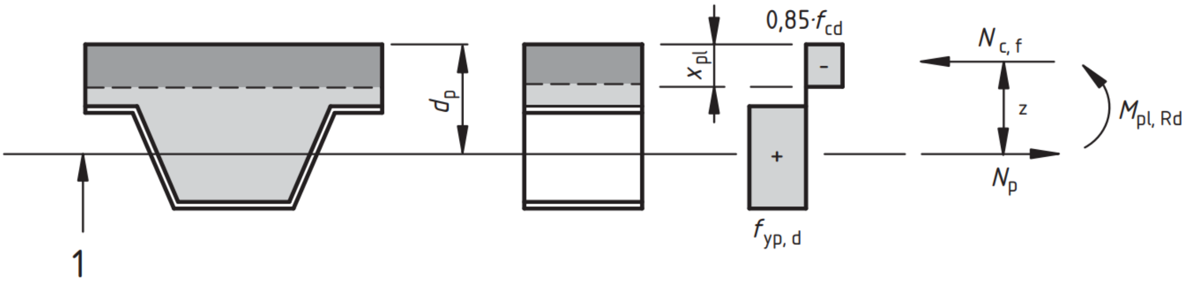

*Figure 2.6. Sagging bending moment resistance with the neutral axis above the steel sheeting [4].*

The following formulas can be used [10]:

$$x_{pl} = \frac{A_{pe} * f_{ypd}}{0.85 * b * f_{cd}}$$

*Equation 2-1*

$$N_p = A_{pe} * f_{yp,d}$$

*Equation 2-2*

$$M_{Pl,Rd} = A_{pe} * f_{ypd}(d_p - \frac{x}{2})$$

*Equation 2-3*

Where:

| | |
|---|---|
| $M_{Pl,Rd}$ | is the sagging bending moment resistance (N*mm). |
| $x_{pl}$ | is the depth of the concrete in compression, or the distance from the top of the slab to the neutral axis (mm). |
| $A_{pe}$ | is the effective area of the steel sheeting per unit width, the embossments should be neglected ($mm^2$). |
| $f_{yp,d}$ | is the design yield strength of the steel sheeting (MPa). |
| b | is the unit width of the slab (mm). |
| $f_{cd}$ | is the compressive design strength of the concrete (MPa). |
| $N_p$ | is the tensile force in the steel sheeting (N). |

$N_{c,f}$ is the design value of the compressive normal force (N).

$d_p$ is the distance from the top of the slab to the centroidal axis of the steel sheeting (mm).

The neutral axis could also be located inside the steel sheeting, the calculations for the sagging bending moment resistance change and can be seen in Figure 2.7 [4].

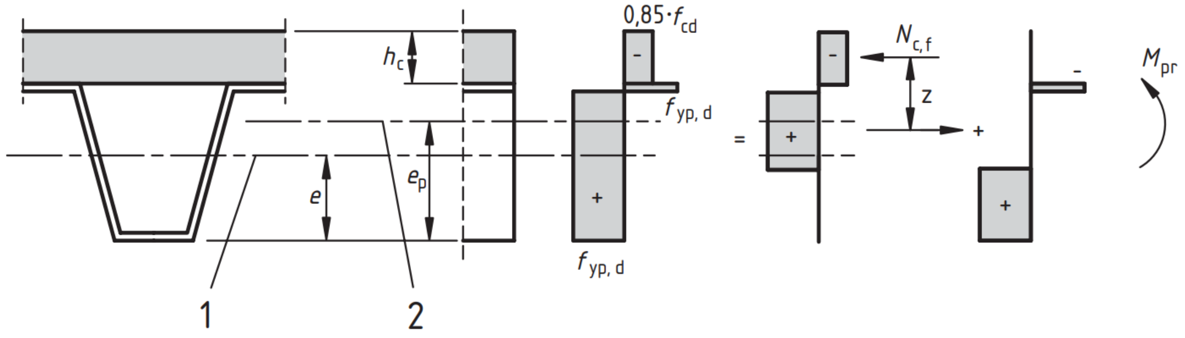

*Figure 2.7. Sagging bending moment resistance with the neutral axis below the steel sheeting [4].*

The following formulas can be used [10]:

$$z = h - 0.5 * h_c - e_p + \left(e_p - e\right) * \frac{N_{cf}}{A_{pe} f_{ypd}}$$

*Equation 2-4*

$$M_{pr} = 1.25 M_{Pa}\left(1 - \frac{N_{c,f}}{A_{pe} f_{yp,d}}\right)$$

*Equation 2-5*

$$M_{pl,Rd} = N_{c,f} * z + M_{pr}$$

*Equation 2-6*

Where:

$M_{Pl,Rd}$ is the sagging bending moment resistance (N*mm).

$e$ is the distance from the bottom of the slab to the centroidal axis of the steel sheeting (mm).

$e_p$ is the distance from the bottom of the slab to the neutral axis of the profile (mm).

The hogging bending moment resistance can also be calculated using section 9.7.2 of Eurocode 4. The slabs that are tested later in this research are simply supported so no hogging bending moment will occur, it will therefore not be shown how to calculate them here.

### *2.1.4.2. Vertical shear failure*

Vertical shear failure can occur when large vertical shear forces are caused by short spans and deep slabs. It should be avoided due to its brittle failure process [9]. Vertical shear resistance should be determined in accordance with EN 1992-1-1 section 6.2.2, according to Eurocode 4 section 9.7.5 [4]. The concrete area contributing to the shear resistance can be seen in Figure 2.8.

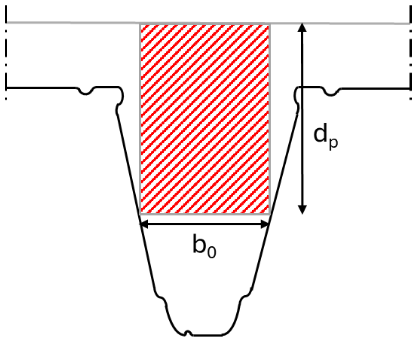

*Figure 2.8. Concrete area contributing to vertical shear resistance.*

The following formulas can be used to calculate the vertical shear resistance $V_{V,Rd}$ [10].

$$k = 1 + \sqrt{\frac{200}{d_p}} \leq 2$$

Equation 2-7

$$v_{min} = 0.035 * k^{3/2}\sqrt{f_{ck}}$$

Equation 2-8

$$V_{v,Rd} = V_{Rd,c} = v_{min} * b_0 * d_p$$

Equation 2-9

Where:

$d_p$ is the distance from the elastic neutral axis of the steel to the top of the slab (mm).

$f_{ck}$ is the characteristic cylinder compressive strength (MPa).

$b_0$ is the mean width of the concrete rib (mm).

### *2.1.4.3. Longitudinal shear failure for slabs without end anchorage*

Longitudinal shear failure occurs if the capacity of the slab is limited by the capacity of the shear connection [9], the available shear connections were discussed in section 2.1.3. There are two methods available to calculate the longitudinal shear resistance of a composite slab [4] [9], the m-k method and the partial shear method.

**m-k method:**

The m-k method is semi-empirical and can be applied when there is ductile and non-ductile longitudinal shear behaviour. According to Eurocode 4 the design resistance $V_{1,Rd}$ should be calculated with the following formula [4];

$$V_{1,Rd} = \frac{b * d_p}{\gamma_{VS}}\left(\frac{m * A_p}{b * L_s} + k\right)$$

Equation 2-10

Where:

$b$ is the width of the slab (mm).

$d_p$ is the effective depth of the slab (mm).

$\gamma_{VS}$ is the partial safety factor for the ultimate limit state.

$A_p$ is the nominal cross-section of the steel sheeting (mm$^2$).

$L_s$ is the shear span (mm).

$m, k$ are empirical factors that can be obtained from slab tests (N/mm$^2$).

The m and k factors have to be obtained by performing 6 slab tests [4]. Two separate groups of three identical slabs have to be tested in a four-point bending test, the deviation of an individual test can't exceed the mean of the group by more than 10%. Group A has a shorter span, and group B has a larger span. Figure 2.9 [4] needs to be used to determine the values for m and k. A line can be drawn between the values of groups A and B, the slope of this line is the value of m. The point where the line intersects the y-axis is the value of k.

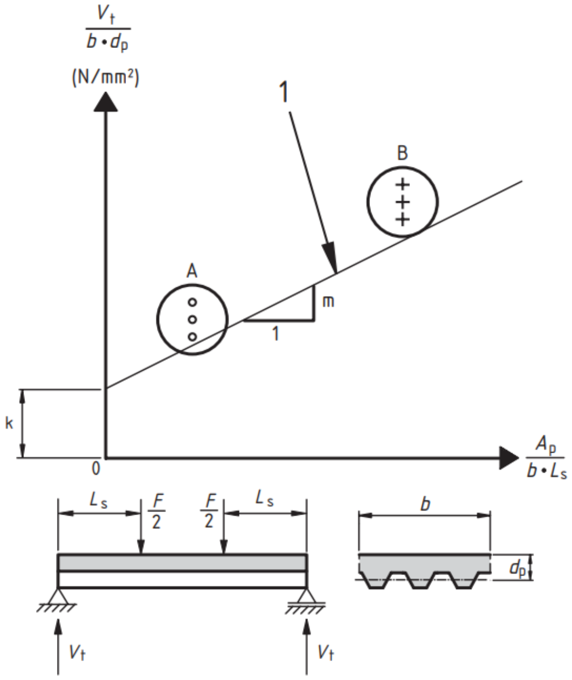

Note: b, $d_p$ and $L_s$ are in mm, $A_p$ is in mm$^2$, $V_t$ is in N.

*Figure 2.9. Determination of the m and k values [4].*

**Partial shear method**

The partial shear method can be used for composite slabs in case of ductile longitudinal shear behaviour. The behaviour may be considered ductile if the failure load exceeds the load which causes an end slip of 0.1 mm, by more than 10% [4]. If the maximum load is reached, and the midspan deflection exceeds L/50, then the failure load should be taken as the load that caused a midspan deflection of L/50 [4].

The partial shear method calculates the compressive normal force $N_c$, which replaces $N_{c,f}$ in Equation 2-5. $N_c$ can be calculated with the following formula [4];

$$N_c = \tau_{u,Rd} * b * L_x \leq N_{c,f}$$

*Equation 2-11*

Where:

$\tau_{u,Rd}$ is the design shear strength, which is obtained from slab tests (N/mm$^2$).

$b$ is the width of the slab (mm).

$L_x$ is the distance of the considered cross-section to the nearest support (mm).

Equation 2-4 which calculates the arm of the normal forces: z, changes into Equation 2-12 [4];

$$z = h - 0.5 * x_{pl} - e_p + \left(e_p - e\right) * \frac{N_c}{A_{pe} f_{yp,d}}$$

*Equation 2-12*

Then with Equation 2-6, the design bending resistance $M_{Rd}$ can be calculated.

### 2.1.5. Composite interaction

When SCC slabs are subjected to loading, bending moments are induced, leading to the development of longitudinal shear stresses at the interface between the steel and concrete. These stresses can cause relative movement, or slip, between the two materials. This slip is mitigated by a longitudinal shear bond. When this bond is “full”, the materials work together seamlessly, and the bond between the materials is infinitely stiff. In this case, the slab can be considered as one element and no slip occurs.

However, when there is no composite interaction, the slab must be considered as the summation of two separate elements. This situation significantly reduces the structural performance, as the steel and concrete components do not act together to resist loads. In this case, slip occurs between the steel and concrete. The degree of composite interaction can vary, leading to no, partial, or full composite action. Partial composite interaction represents an intermediate state where some degree of slip occurs, but there is still a considerable load-sharing between the materials.

The concept of composite interaction is often illustrated using simplified composite beam models. These models help in visualizing the different levels of interaction between steel and concrete under load. For instance, Figure 2.10 [11] illustrates examples of no, partial, and full composite interaction in composite beams.

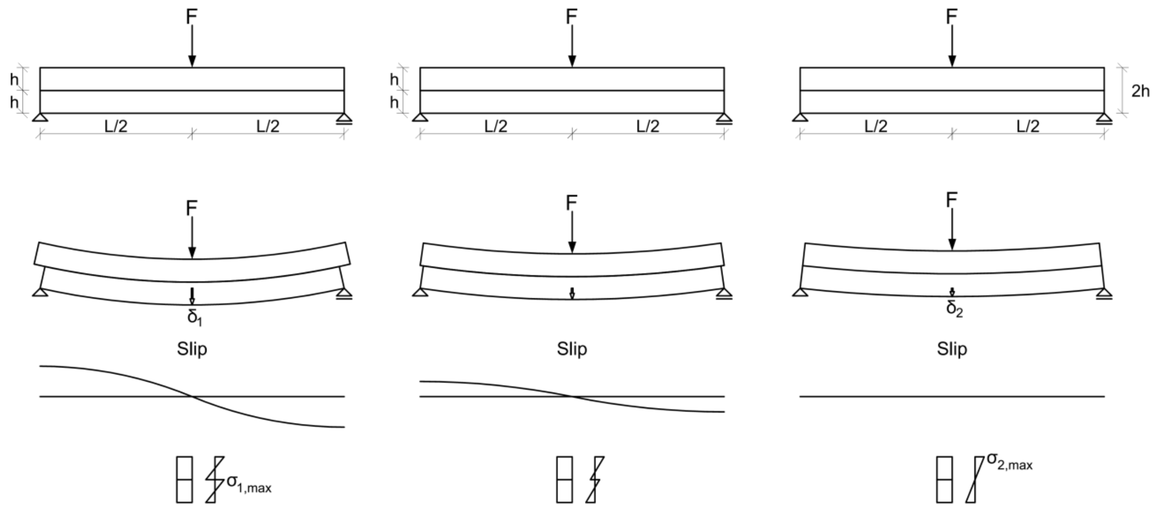

*Figure 2.10. No, partial, and full composite interaction for composite beams [11].*

For the case of no composite and full composite interaction the section modulus, second moment of inertia, and the normal stress can be calculated. These calculations are shown in Table 2.1.

*Table 2.1. Calculations for no composite interaction, and full composite interaction.*

| | *No composite interaction* | *Full composite interaction* |
|---|---|---|
| *W (mm³)* | $2 * \left(\frac{1}{6} * b * h^2\right) = \frac{1}{3} * bh^2$ | $\frac{1}{6} * b * (2h)^2 = \frac{2}{3} * bh^2$ |
| *I (mm⁴)* | $2 * \left(\frac{1}{12} * b * h^3\right) = \frac{1}{6} * bh^3$ | $\frac{1}{12} * b * (2h)^3 = \frac{4}{6} * bh^3$ |
| *σ (MPa)* | $\frac{M}{W_{no}} = \frac{M}{\frac{1}{3}bh^2}$ | $\frac{M}{W_{full}} = \frac{M}{2 * \frac{1}{3}bh^2}$ |

Where:

$W$ is the section modulus of the composite beam (mm$^3$).

$I$ is the second moment of inertia of the composite beam (mm$^4$).

$\sigma$ is the stress due to bending (MPa).

$M$ is the bending moment (N*mm).

The section modulus (W) for full composite interaction in SCC slabs is twice as high as when there is no composite interaction. Additionally, the second moment of inertia (I) is four times greater in the case of full composite interaction. This difference results in the maximum stress being reduced by half in the case of full composite interaction compared to when there is no composite interaction. Lower stress levels contribute to enhanced durability and serviceability of the slab, as the materials are less likely to experience fatigue or failure under typical loading conditions. Therefore, achieving full composite interaction is more desirable in the design and construction of SCC slabs.

Papastergiou et al. [12] researched the experimental verification of a steel-concrete composite beam. In this research, the neutral axis of the cross-section was found at both the elastic stage and the ultimate limit state. The neutral axis was determined using strain measurements performed by 5 strain gauges which were distributed along the height of the steel girder. The composite beam was subjected to a cyclic loading part and a static loading part. During the elastic loading in the cyclic loading part, there was one neutral axis for the full cross-section. However, in the ultimate limit state a partial connection developed due to slip occurring between the steel girder and the concrete, this caused two partly separate neutral axes to form [12]. A cross-section of the beam and the locations of the neutral axes are illustrated in Figure 2.11 [12].

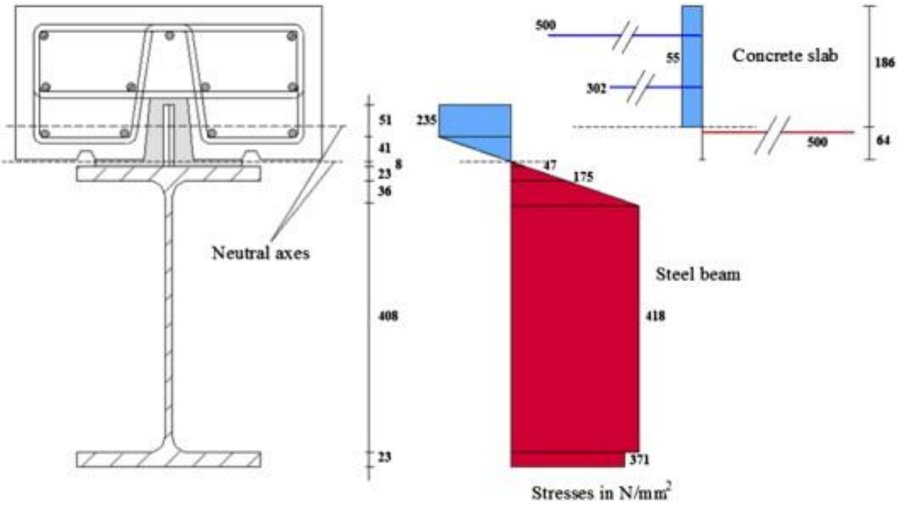

*Figure 2.11. Two neutral axes for a composite beam [12].*

## 2.2. Optical fiber sensors

Developments of modern optical fibers started in 1977 and were intended for long-distance telecommunications. These fibers were extensively researched, and by 1982 optical fiber sensors (OFS) were capable of detecting several properties, including strain. The fibers revolutionized the telecommunications industry and with that came quality improvements, wider availability, and lower costs of optical fibers [13]. OFSs can collect information along the length of the fiber through light scattering. There are several different types of OFS, and the main focus of this research will be on Fiber Bragg Grating Sensors since they were used in the experimental part of this research. Firstly the background of optical fibers will be discussed and then its applications in civil engineering projects.

### 2.2.1. Background of optical fiber sensors

An optical fiber has a cylinder shape and consists of a core, through which the light waves travel, and a cladding around the core, which traps the light inside the core. Additional protection can be given to the fiber with an external coating. For telecommunications, it is desired that the fiber has as few disruptions as possible from external influences. However, for optical fiber sensors, this is desired and these effects are therefore enhanced [13]. There are several types of optical fiber sensors (OFS), and they can be divided into three classes; interferometric sensors, distributed sensors, and grating-based sensors [14]. The optical fibers used in the test were Fiber Bragg Grating (FBG) sensors, which are part of the grating-based sensors category. The focus of the rest of this section will therefore be on FBG sensors.

Fiber Bragg Grating sensors are based on the principle of changes in the reflected wavelengths of the light, as it travels through the core [15]. FBGs are grated by laterally exposing the fiber core to a pattern of intense laser light. The light exposure pattern changes the refractive index permanently, creating a fixed index modulation [16]. Individual gratings can be located close to each other which enables distributed measurements. When a spectrum of light propagates through the core, a specific wavelength is reflected, and the rest of the spectrum continues unaffected. This reflected wavelength is called the Bragg wavelength. This is illustrated in Figure 2.12 [14].

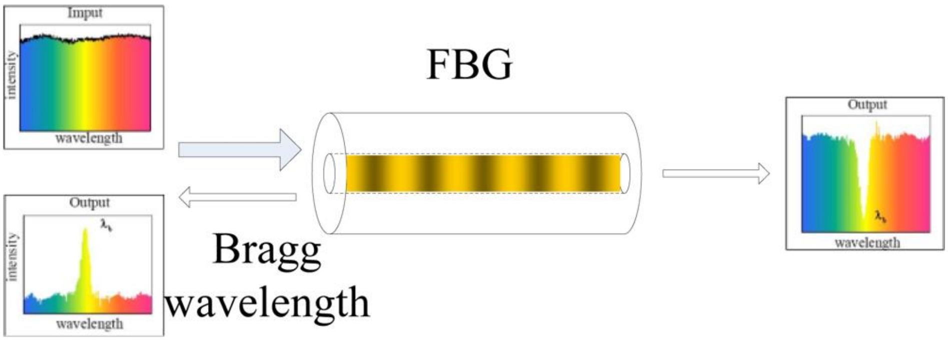

*Figure 2.12. Principle of Bragg wavelength reflection [14].*

The Bragg wavelength depends on the refractive index and the grating pitch, which can be affected by external factors like strain and temperature. These external factors cause a Bragg wavelength shift, this shift can be measured and translated into strain measurements [14].

### 2.2.2. Civil engineering applications of optical fibers

Distributed fibers have been applied to civil engineering structures or components of structures. Some cases relevant to this thesis will be expanded upon in this section.

**Fibers inside reinforced concrete**

Bado et al. [5] used Distributed Optical Fiber Sensors (DOFS) to perform strain measurements inside reinforced concrete. The goal of this study was to measure the strain of embedded rebars, induced by concrete shrinkage. Two different fibers were utilized, one thin chemical polyamide-coated DOFS, and one with a central metal tube and an outer thick polyamide sheath. The fibers were applied to the rebars in four different manners;

a) The thin fiber was glued with a cyanoacrylate adhesive, in the concavity created by the longitudinal ridge of the rebar.
b) The thin fiber was applied similarly to option a), except there is an additional protective layer of water-proof oxygen-free silicone rubber.
c) The thin fiber was positioned in an incised groove, and glued with a cyanoacrylate adhesive.
d) The thick fiber (blue) was positioned in an incised groove, and glued with an epoxy adhesive.

These applications are illustrated in Figure 2.13 [5].

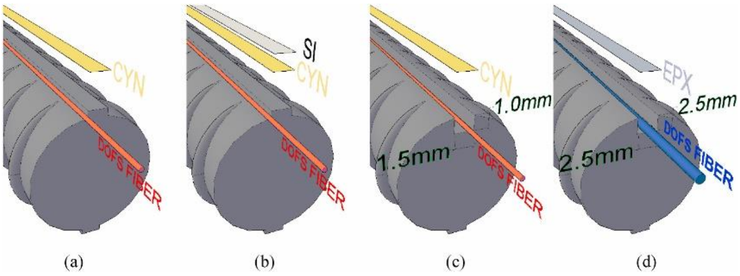

*Figure 2.13. Application of fibers on rebars [5].*

Bado et al. [5] concluded that option b) yielded the best and most reliable strain measurement results. However, in this test shrinkage strains were measured, which are relatively low. The maximum measured strain was 321 με, for tensile tests, yielding of steel could be reached which is approximately 2750 με for S500 [5]. This means results might be different for higher strains.

Kaklauskas et al. [15] researched different experimental setups regarding reinforcement strain data. Double pull-out tests were performed on rectangular reinforced concrete elements. In this research Fiber Bragg Grating (FBG) sensors were applied in a shallow groove on the reinforcement bar. The fiber location and the measurement points along the length of the rebar are illustrated in Figure 2.14 [15].

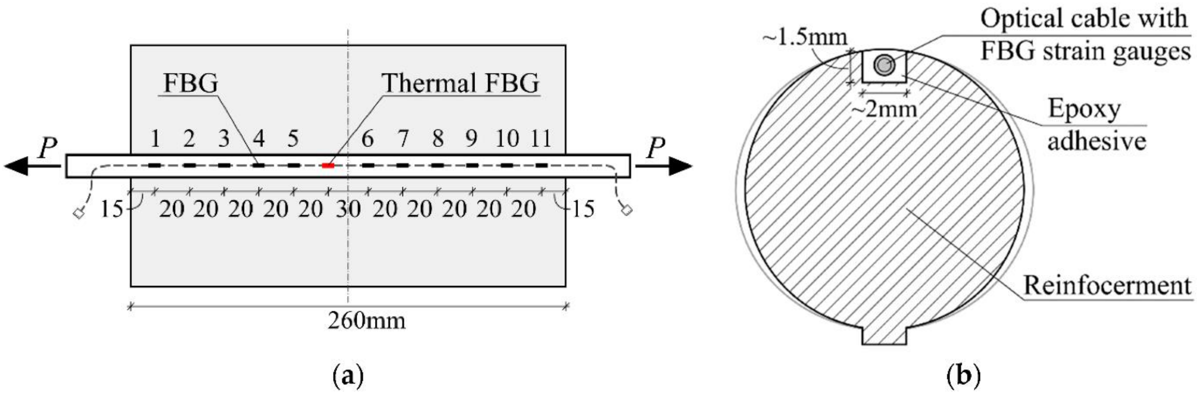

*Figure 2.14. Measurement points along the length of the rebar (a), and the location of fiber on the rebar (b) [15].*

The fiber results were compared with data from strain gauges. The strain gauges were applied in the middle of a rebar. The rebar was cut in half and a groove was made on one of the halves to accommodate space for the strain gauges. The two halves were glued together using an epoxy adhesive. The location of the strain gauges in the cross-section and along the length of the rebar is shown in Figure 2.15 [15].

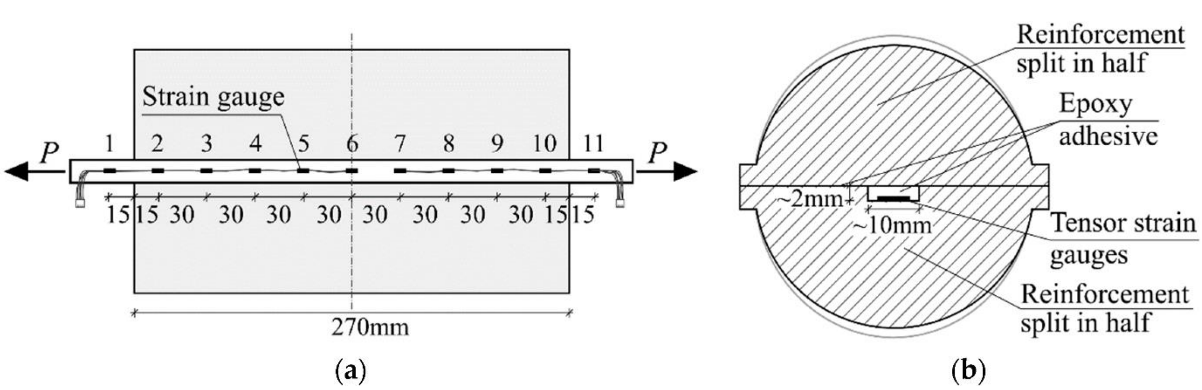

*Figure 2.15. Location of the strain gauges along the length of the rebar (a), and the location of the strain gauges in the cross-section (b) [15].*

Kaklauskas et al. [15] concluded that both experimental setups yielded reasonable accuracy and smoothness, however, the fiber data had some anomalies. The measured strains exceeded the estimated values, and there was a noticeable asymmetry between the left and right sides of the specimen. Despite these discrepancies, the fiber method is preferred over the strain gauge method. This preference is due to its simpler application process, the ability to have a finer spacing of measurement points, and the limitation of strain gauges, which cannot be applied to smaller diameter rebars.

**Fibers on steel surfaces**

Distributed optical fibers have also been applied to steel surfaces. Weisbrich et al. [17] researched differences in strain measurements between different fiber coatings and adhesives on steel surfaces. Three different fiber coatings were tested, Ormocer®, polymide, and acrylate. To apply the fibers, several different adhesives were used;

- M-bond 200
- Loctite HY 4090
- Loctite EA 3430
- Z70
- MD-Megabond 200
- Loctite 4902

Three separate specimens were prepared, each with a different fiber coating. The dimensions of the specimens were 70.3 mm x 15.3 mm x 500 mm. Four-point bending tests were conducted at three different load levels. The test setup and the locations of the fibers are shown in Figure 2.16 [17].

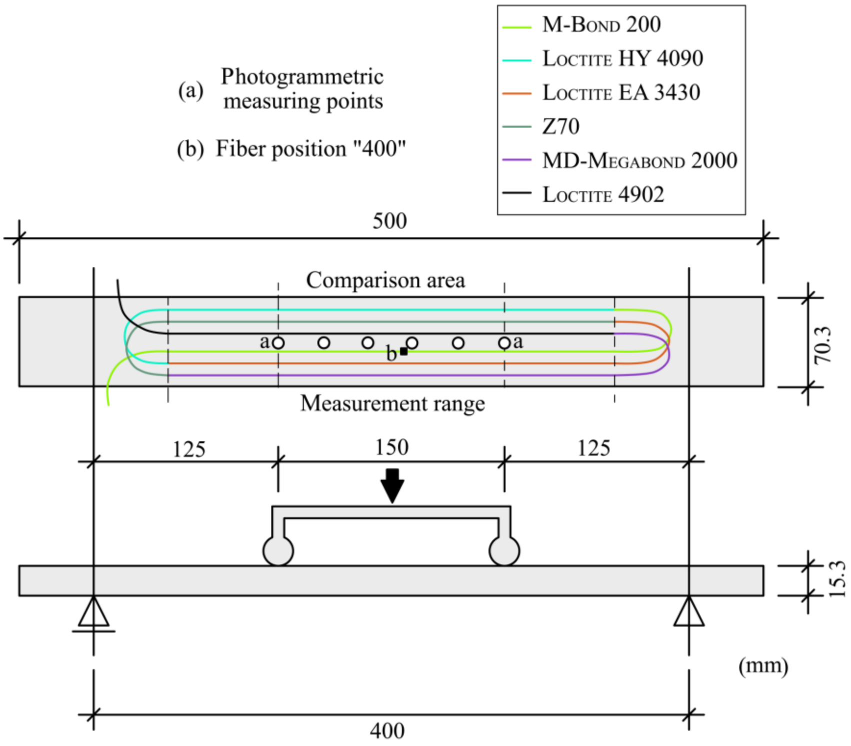

*Figure 2.16. Test setup and fiber locations [17].*

Weisbrich et al. [17] found that the results for Ormocer® and polyimide coatings closely correlated with the reference measurements and analytical calculations. The acrylate fiber exhibited a high loss of strain due to slipping between the coating and the cladding. All six adhesives tested yielded similar results, indicating that any of them can be effectively implemented. Lastly, the preparation of the bonding area and the application of adhesive are essential for achieving accurate results.

**Detecting buckling with distributed optical fibers:**

Tan et al. [18] utilised distributed fiber optic sensors to detect buckling and reconstruct three-dimensional deformations. The DOFs were applied to an aluminium bar and a thin steel plate which were compressed until they buckled. The setup and location of the fibers is illustrated in Figure 2.17 [17].

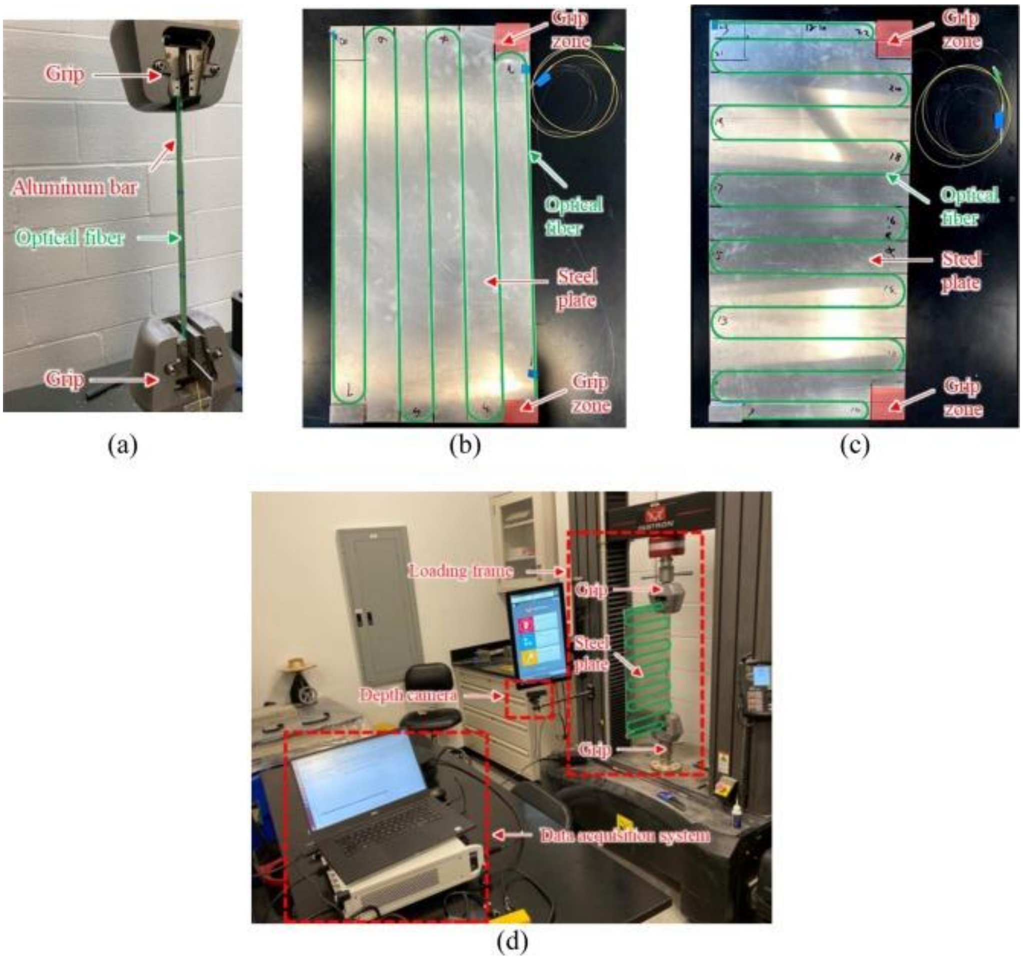

*Figure 2.17. Test setup and location of the DOFs on the bar (a) and plate (b and c) [18].*

Using these tests, Tan et al. [18] was able to develop an approach to detect, measure, visualize, and quantify 3D buckling, using distributed optical fibers. The fiber results were validated by a computer vision method that measured a point cloud from the specimens. They concluded that the distributed strain measurements of the DOFs can be used to detect buckling in thin-walled structures [18]. However, they noted that this investigation applies to simple thin-walled specimens, and its performance in more realistic real-world applications is unknown.

**Fibers in composite slabs**

Bai et al. [19] applied distributed optical fibers in steel-concrete composite slabs. The objective of the research was to assess the flexural behaviours of composite floor beams, using distributed optical fibers. The fibers were embedded inside the concrete and attached to a wire mesh, this is illustrated in Figure 2.18 [19]. The composite floor beams are loaded to failure using a test setup shown in Figure 2.19 [19].

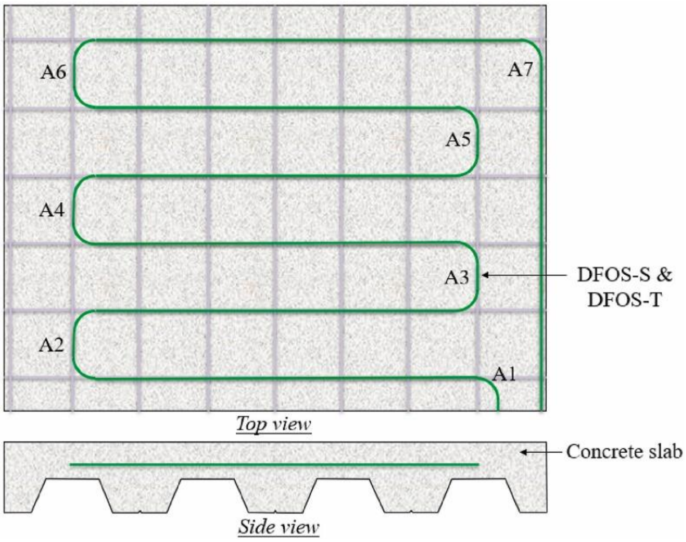

*Figure 2.18. Top and side view, showing the location of the optical fibers in the slab [19].*

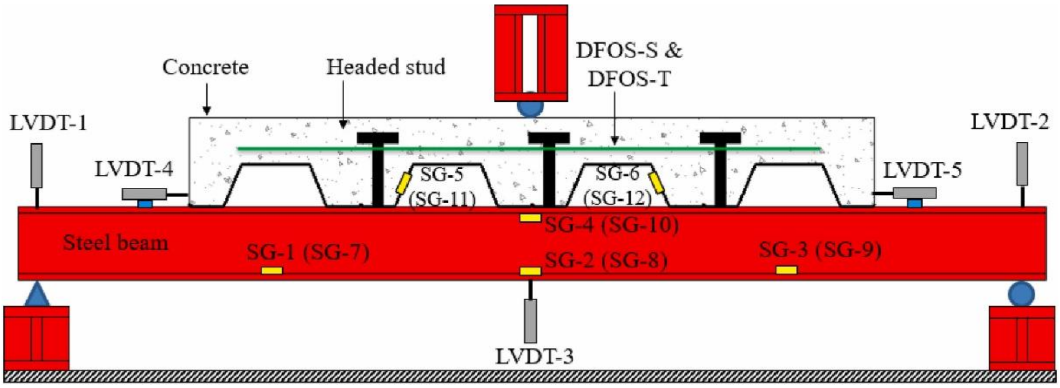

*Figure 2.19. Test setup [19].*

Based on the tests, it was concluded that the deployment method for distributed optical fiber sensors is recommended for real-life applications. These optical fibers enable in-situ monitoring of concrete cracks and can detect microcracks before they become visible. However, optical fibers have two limitations in detecting concrete cracking. Firstly, the fibers only detect intersections with cracks, which should be taken into account during placement. Secondly, when the spacing between cracks is less than 100 mm, individual cracks cannot be identified.

# 3. Experimental setup

For this thesis, Distributed Optical Fibers (DOFs) were applied to deep steel-concrete composite slabs that underwent a four-point bending test. The test setup used for the full-scale experiments is shown in Figure 3.1, the schematic overview of the setup, described by Eurocode 4 [4], is shown in Figure 3.2.

*Figure 3.1. Test setup of the full-scale experiments.*

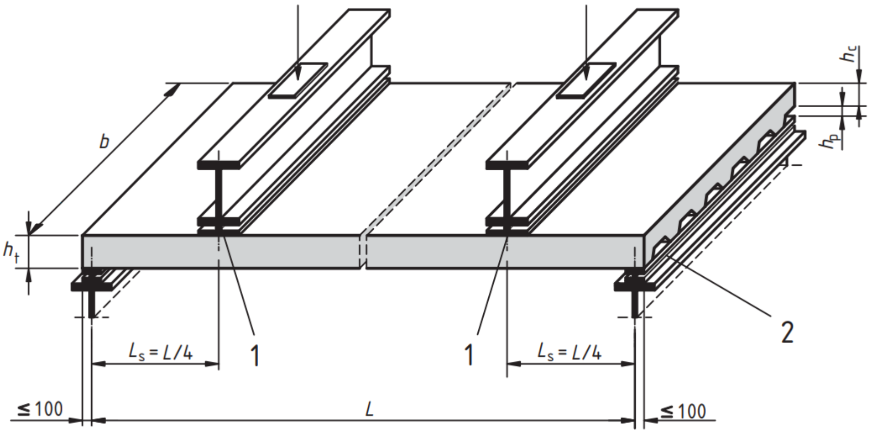

*Figure 3.2. Test setup described by Eurocode 4 [4].*

## 3.1. Specimens and materials properties

Firstly, information on the specimens and their material properties will be given. There were 14 specimens in total, however, distributed optical fibers were applied to 5 composite slabs. This is due to the availability of the optical fibers. These slabs were S6, S7, S10, S11, and S12, the dimensions of these slabs are given in Table 3.1.Table 3.1. Dimensions and general information on all specimens.

Table 3.1. Dimensions and general information on all specimens.

| *Specimen* | *Span, L (mm)* | *Shear span, $L_s$ (mm)* | *Width, b (mm)* | *Total height, $h_t$ (mm)* | *General information* |
|---|---|---|---|---|---|
| S6 | 5400 | 1350 | 2500 | 270 | Regular C20/25 concrete |
| S7 | 7200 | 1800 | 2500 | 270 | Regular C20/25 concrete |
| S10 | 3600 | 900 | 2500 | 270 | Recycled aggregate concrete |
| S11 | 3600 | 900 | 2500 | 270 | Regular C20/25 concrete, without rib reinforcement |
| S12 | 3600 | 900 | 2500 | 270 | Regular C20/25 concrete, with colour-coated sheeting |

The specimens are 2500 mm wide and have 5 ribs, however, the two ribs on the side of the slab can be considered as half a rib. This is illustrated in Figure 3.3. A schematic view of a single rib is shown in Figure 3.4 [20].

Figure 3.3. Side view of a slab.

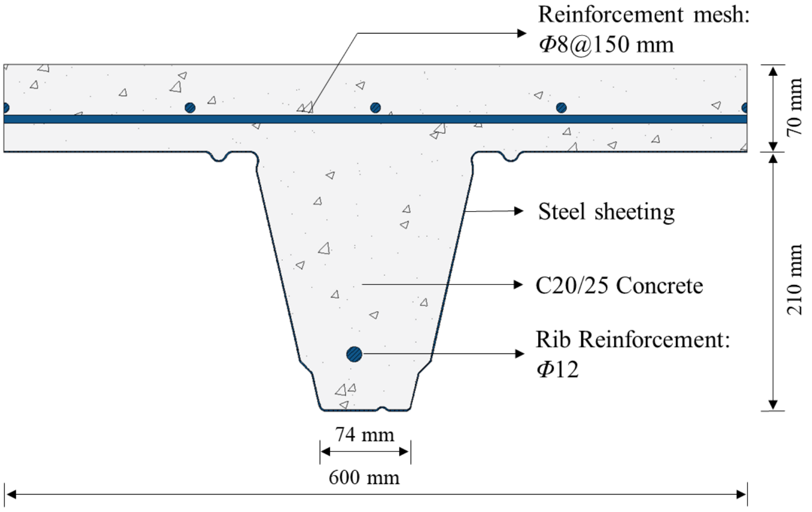

Figure 3.4. Schematic view of a single rib [20].

A detailed overview of the steel sheeting and the embossments is provided in Appendix A. The steel sheeting and reinforcement mesh, as illustrated in Figure 3.4, are identical for every slab, ensuring consistency in structural components across the specimens. However, there are notable exceptions: specimen S12 features colour-coated steel sheeting, where both sides of the steel are painted. This coating is primarily applied for aesthetic purposes, enhancing the visual appeal of the slab. Additionally, the concrete composition varies among the slabs. Specifically, slab S10 utilizes recycled aggregate concrete, distinguishing it from the other slabs, which are constructed with standard C20/25 concrete. Furthermore, all slabs are reinforced with rib reinforcement, except slab S11, which lacks this additional reinforcement. These variations and specific details are summarized in the final column of Table 3.1, ensuring that all relevant information is readily accessible for reference and analysis.

## 3.2. Loading procedure

The loading procedure is described by Eurocode 4, it consists of 2 tests [4]. The initial test is cyclic loading, which is load-controlled, 25 cycles are performed for each slab. The subsequent test is where the slab is loaded to failure under a monotonic load, which is displacement-controlled.

For the initial test, the cyclic load should vary between a lower limit, which should be less than $G + 0.2*(W_t – G)$, and an upper limit which should be higher than $0.6*W_t$. G is the self-weight of the slab and $W_t$ is the measured failure load of the preliminary static test [4].

The subsequent test starts after the initial test is over. The slab is subjected to an imposed load that increases progressively, such that failure occurs after at least 1 hour. The failure load ($W_t$) is the maximum load imposed at failure including the self-weight of the slab and the weight of the spreader beams [4].

The lower limit, upper limit, and the loading rate of the cyclic loading are shown in Table 3.2 for all slabs. Additionally, the peak load and the loading rate of the subsequent phase are also shown in table 3.2.

*Table 3.2. Cyclic load limits and loading rate.*

| *Specimen* | *General information* | *Lower limit, cyclic loading (kN)* | *Upper limit, cyclic loading (kN)* | *Loading rate, cyclic loading (kN/s)* | *Peak load (kN)* | *Loading rate, subsequent phase (mm/min)* |
|---|---|---|---|---|---|---|
| S6 | Regular C20/25 concrete | 75 | 150 | 5 | 220.7 | 1 |
| S7 | Regular C20/25 concrete | 35 | 65 | 3 | 142.2 | 2 |
| S10 | Recycled aggregate concrete | 90 | 225 | 5 | 279.6 | 0.75 |
| S11 | Regular C20/25 concrete, no rib reinforcement | 75 | 155 | 3 | 217.6 | 0.5 |
| S12 | Regular C20/25 concrete, colour-coated sheeting | 40 | 70 | 1 | 366.1 | 0.75 |

## 3.3. Distributed optical fiber locations

A coordinate system is introduced to all relevant figures to provide a consistent frame of reference across all figures, making it easier to understand the spatial positioning and direction of the fibers within the slab. The origin of this coordinate system, as well as the directions of the X, Y, and Z axes, are depicted Figure 3.5.

The axis orientation:

- The X-axis runs along the span of the slab, indicating the longitudinal direction.
- The Y-axis is oriented along the width of the slab, representing the transverse direction.
- The Z-axis extends along the height of the slab, corresponding to the vertical direction.

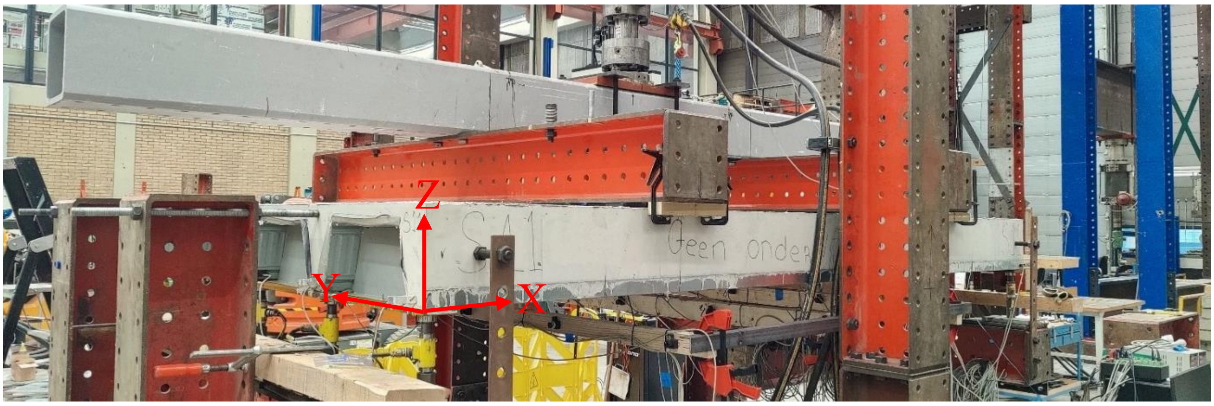

Figure 3.5. Coordinate system of the slabs.

The Distributed Optical Fibers (DOFs) were applied along the span (in the X-direction) at various locations. For Slabs 6, 10, 11, and 12, the fibers were positioned along the middle rib of each slab at seven distinct points. These positions are highlighted in the cross-sectional view at mid-span, as shown in Figure 3.6. Additionally, for Slab 12, a fiber was also applied to the side of the slab on the concrete surface, as indicated in Figure 3.6.

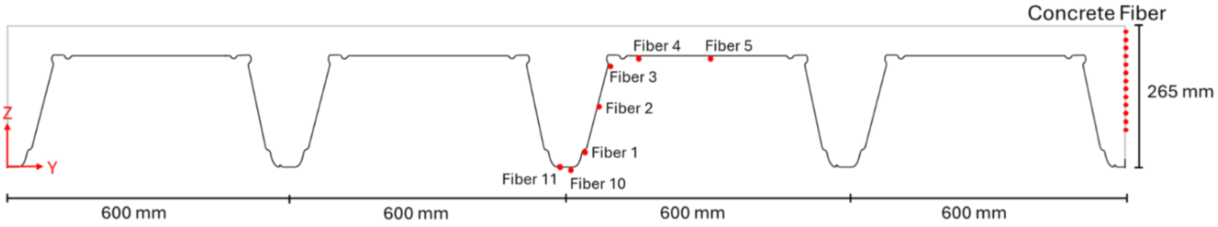

Figure 3.6. Indication of the fiber positions in the cross-section at mid-span.

The position of the fibers along the span has been indicated in Figure 3.7, the Concrete Fiber is indicated with a red box and the fibers in the steel sheeting are indicated with dashed lines. The steel fibers do not reach the supports of the slabs because there was a steel plate that hindered the application in that location, instead, the fibers start and end approximately 100 mm from the supports.

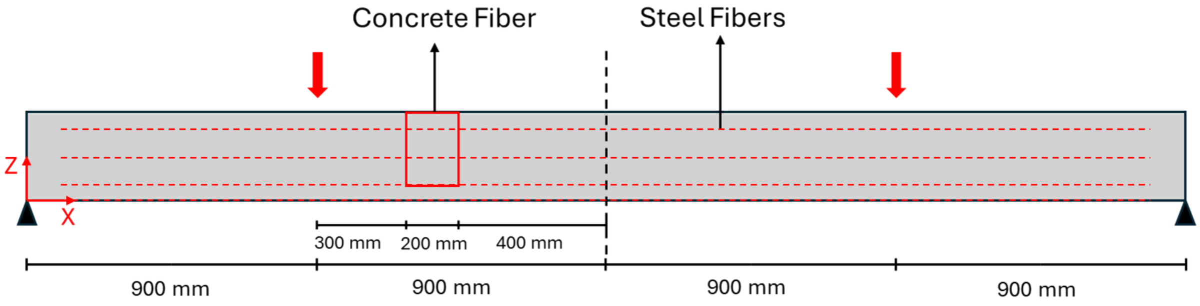

*Figure 3.7. Side view of a 3.6 meter slab, indicating the fiber positions.*

A photograph of the Steel Fibers is shown on the left side and the Concrete Fiber is shown on the right side.

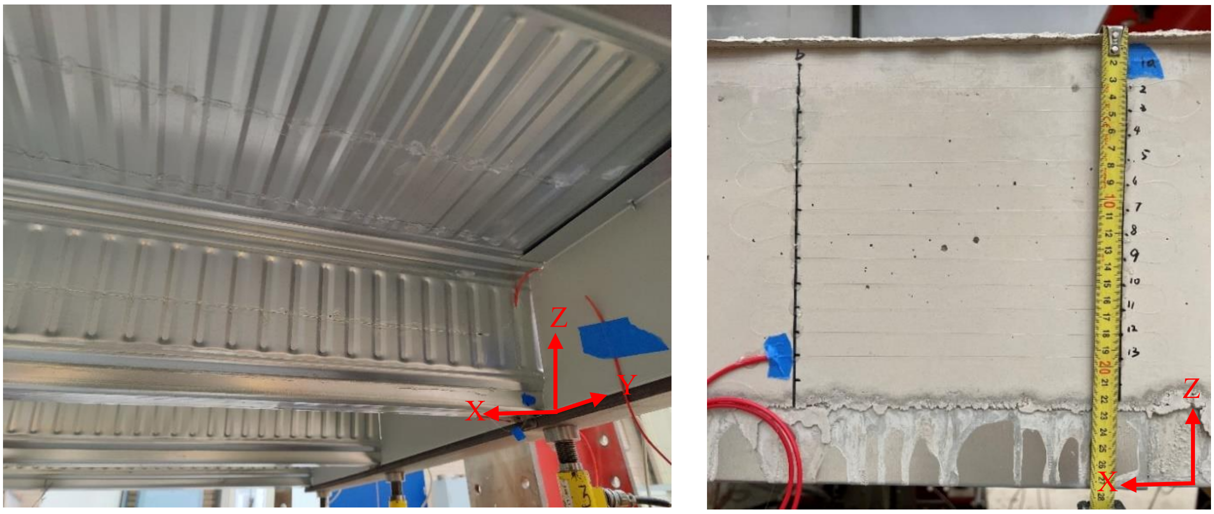

*Figure 3.8. Photograph of the Steel Fibers (left) and the Concrete Fiber (right).*

For Slab 7, which spans 7.2 meters, only Fiber 11 was applied, however, it was applied to all 5 ribs. This was done to determine the location of the concrete cracks throughout the slab. The locations are highlighted in the cross-section shown in Figure 3.9.

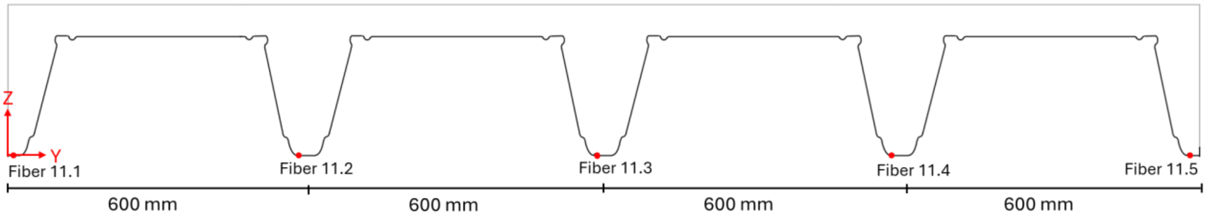

*Figure 3.9. Cross-section of Slab 7, indicating the fiber locations.*

An overview is given below to see which Slabs have which Fibers;

- Slab 6: Fibers 1, 2, 3, 4, 5, 10, and 11
- Slab 7: Fibers 11.1, 11.2, 11.3, 11.4, and 11.5
- Slab 10: Fibers 1, 2, 3, 4, 5, 10, and 11
- Slab 11: Fibers 1, 2, 3, 4, 5, 10, and 11
- Slab 12: Fibers 1, 2, 3, 4, 5, 10, 11, and the Concrete Fiber

## 3.4. Distributed optical fiber application

The fibers need to be applied to the specimens in a way that ensures proper bonding with the specimen to make sure that the strains of the steel sheeting are identical to the strains experienced by the fibers. To achieve this, the adhesive used not only has to create a strong bond but also has to yield with the steel to maintain strain compatibility throughout the test.

To prepare the steel surface, it was first cleaned with acetone to remove any contaminants. A two-component quick-drying glue was selected for this experiment, used in combination with Araldite 2011, an epoxy adhesive known for its strong bonding properties. The application process was relatively straightforward for the fibers on the flat steel sheeting. The two-component glue was applied approximately every 50 cm to straighten the fiber and secure it in the desired position, which was needed since the fibers had to be applied to the underside of the slab. Once the fiber was positioned, the epoxy was carefully applied over it and evenly distributed by hand. The quick-drying glue set within a few seconds, providing immediate adhesion, while the epoxy required 24 hours to fully cure.

For the embossed part of the steel sheeting, this could not be done in the same manner because the fibers have to follow the embossments. Instead, the two-component glue had to be applied in every embossment, and in between the embossments the epoxy would be applied. Figure 3.10 shows a close-up of a fiber applied over embossments, the fiber is indicated with a dashed red line. The steps taken to apply the fiber are shown in Figure 3.11.

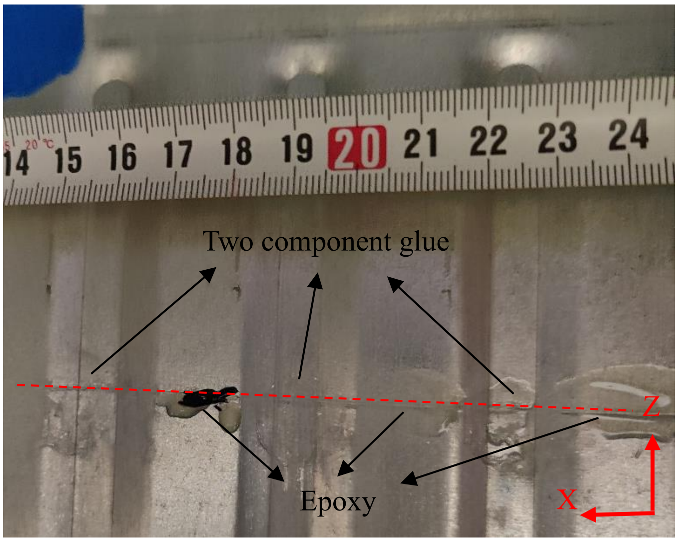

*Figure 3.10. Close-up of the embossed part of the steel sheeting.*

*Figure 3.11. Application of two-component glue on embossments (left), application of epoxy (middle), and spreading the epoxy by hand (right).*

After the application of the fibers, both ends have to be prepped to be connected to the Luna ODISI 6104 Series measuring system. The start of the fiber will be connected to the Luna system with a pigtail, and the end will be connected to a coreless fiber which protects the end of the fiber.

The following steps have to be taken to connect the fiber to the Luna system:

a) Strip away approximately 15 mm of the cladding of the fiber at both ends.
b) Clean both ends of the fiber with alcohol.
c) Make a straight cut of the fiber at 90 degrees.
d) Do steps a, b, and c for the pigtail and the coreless fiber.
e) Splice the start of the fiber to the pigtail and the end of the fiber to the coreless fiber.
f) Cover the spliced part of the fiber with a protector.

Steps a), c), and e) have been illustrated in Figure 3.12.

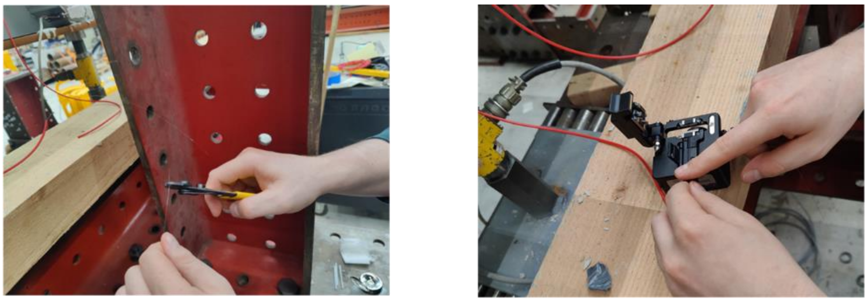

Step a) Step c)

Step e)

*Figure 3.12. Steps of connecting the fiber to the Luna system.*

# 4. Embossment region behaviour

Steel-concrete composite slabs have embossments that transfer shear forces between the steel sheeting and concrete. The strain values of the embossed steel sheeting will be different from the strain of the flat steel parts. Distributed optical fibers were applied to the embossed parts of the steel sheeting to highlight this difference. Fiber 2 was placed on the steel sheeting web, and Fiber 4 and 5 were placed on the top flange of the steel sheeting. This is illustrated in Figure 4.1, where the fiber locations are also shown in the cross-section of the middle rib.

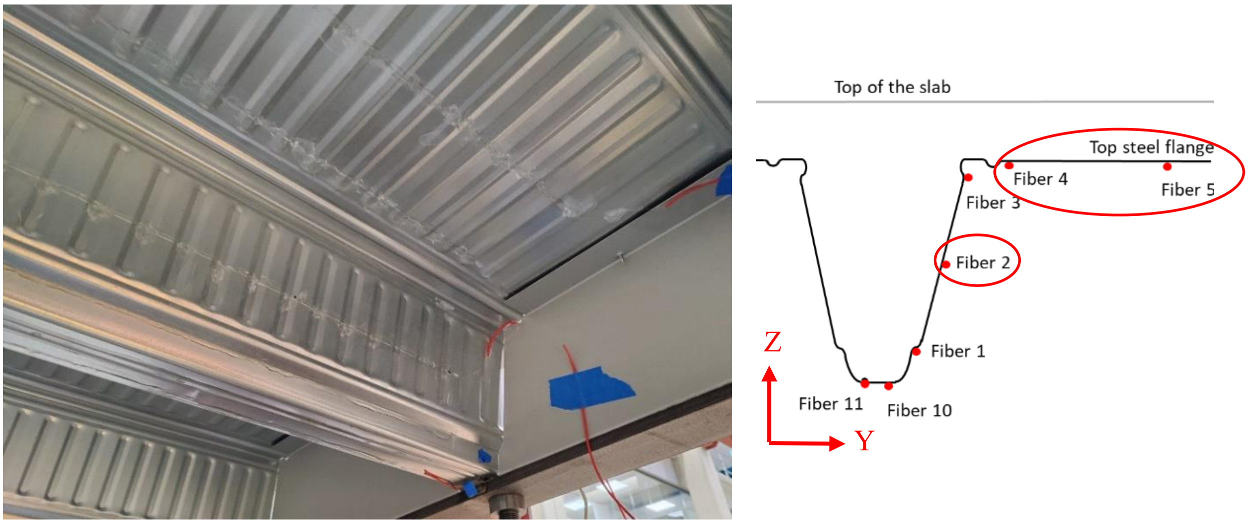

*Figure 4.1. Fibers applied on the embossments.*

Fibers 2, 4, and 5 are located on the embossed part of the steel sheeting, this causes the strain data of these fibers to have oscillations. However, these oscillations do not occur instantly. For Fiber 2 it occurs at the start of the test, during the first cycle of the cyclic loading part. This is the case for all specimens. An example is given on the left side of Figure 4.2, here the strain of Fiber 2 from Slab 12 is shown over the span of the slab, at two load levels. These load levels are highlighted in the load-displacement curve of slab 12 in Figure 4.3, the blue graph is before cyclic loading and the orange is after. A close-up of the strain data around the mid-span is illustrated next on the right side of Figure 4.2.

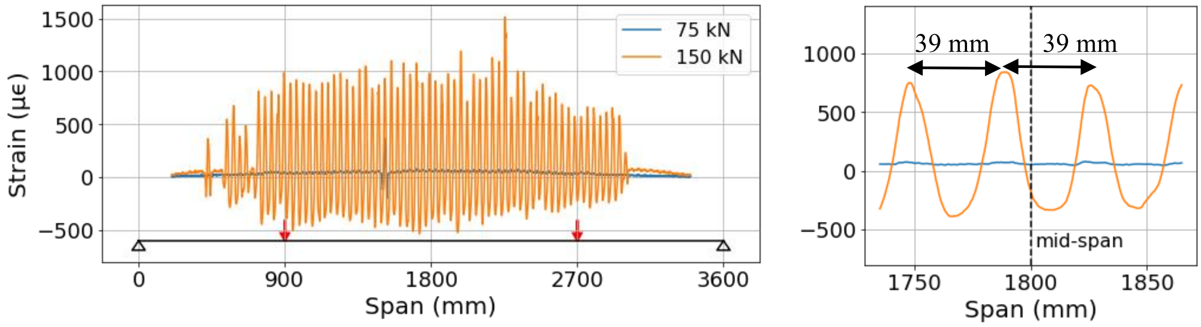

*Figure 4.2. Strain of Fiber 2 along the full span of Slab 12 (left), and a close-up of the strain of Fiber 2 around the mid-span (right).*

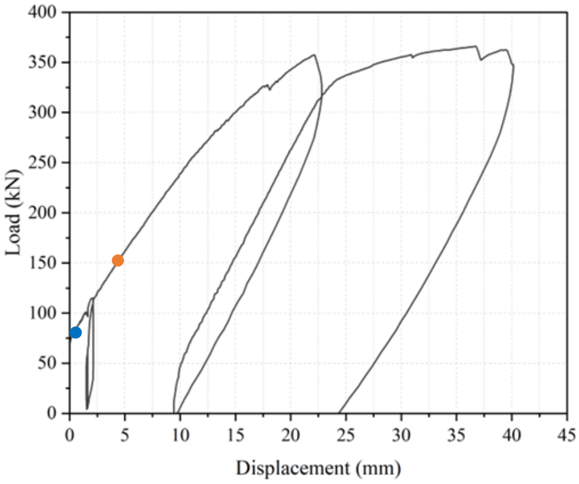

*Figure 4.3. Load-displacement graph of slab 12, indicating the 2 load points shown in Figure 4.2.*

Figure 4.2 shows that the strain is relatively constant at first, and then the oscillations occur at a later stage during loading. This is due to the debonding between the steel sheeting and concrete.

The strain values of the peaks are positive and the valleys are negative, as opposed to fibers on the flat steel part which have relatively constant strain values, either positive or negative. The oscillations are approximately 39 mm apart which is also the distance between the embossments of the measured specimens, this indicates that the oscillations are caused by the embossments of the steel sheeting.

The oscillations that form in Fibers 4 and 5 are very similar to those illustrated in Figure 4.2. However, the oscillations occur at a later stage compared to those in Fiber 2. In Slabs 6 and 11, some oscillations develop during cyclic loading. The more uniform oscillations, resembling those in Figure 4.2, begin to form when the load reaches approximately 70% of the peak load during the static loading phase of the test.

In contrast, for Slab 12, no oscillations form during the cyclic loading phase. Instead, they begin to appear at 90% of the peak load on the right side of the slab and 95% on the left side. This difference is likely due to the differences between the maximum load levels of the cyclic loading part. For Slab 12 the maximum load of the cyclic loading part is 17% which is relatively low. For Slab 6 this maximum load is 68%, and for Slab 11 this is 67%, which is relatively high.

To better understand the cause of the oscillation it is important to know what parts of the embossments are in tension and which are in compression. This will be discussed in the following section.

## 4.1. Location of the peaks

The fiber data can be compared with the data from the strain gauges. The strain gauges were applied at mid-span at the same locations as the fibers. Thus, for each strain gauge, there is one measurement point of the fiber that should give the same strain values over time. The strain gauges can be used to find which part of the embossed steel sheeting is in tension and which is in compression since the location of the strain gauges is known. The embossments of the web and the top flange are slightly different and will therefore be looked at separately. The web is deformed into the concrete, which will be referred to as indentation. In contrast, the steel on the top flange deforms away from the concrete, creating what will be referred to as embossments. This distinction is illustrated in Figure 4.4. In both cases, the strain gauge is applied to the flat part.

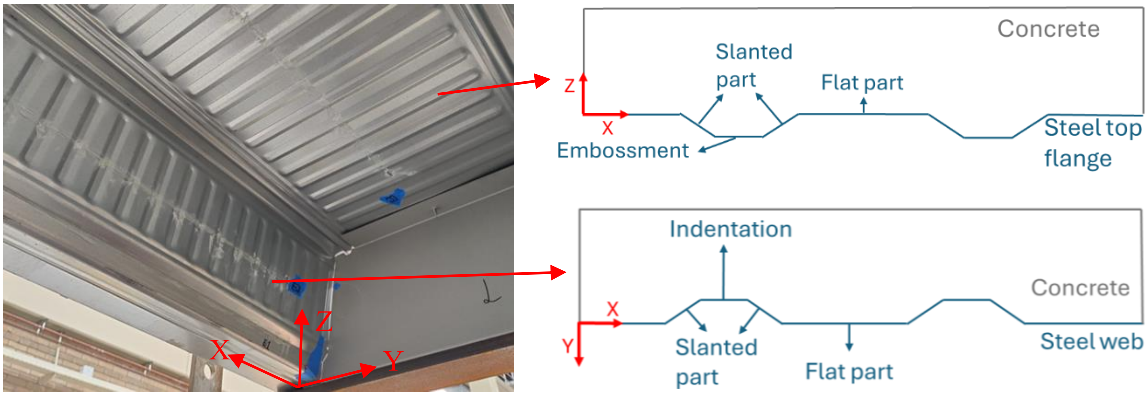

*Figure 4.4. Embossments of the web and the top flange.*

### 4.1.1. Web embossments

Fiber 2 is applied on the web embossments of Slabs 6, 10, 11, and 12. Slab 11 will be used to illustrate the steps taken to identify which parts of the steel sheeting are in tension and which are in compression. The results of the other Slab are given in the Appendix B.

**Slab 11**

Slab 11 is 3.6 meters long and does not have a reinforcement rebar in its ribs. It experienced flexural failure and had a peak load of 217.6 kN.

The strain gauge is applied at the centre of the slab, however, this might not be the centre of the flat part of the web, as shown in Figure 4.5. It shows that the strain gauge is applied off-centre, to the left, it is almost on the edge of the flat part. Fiber 2 is indicated with a red dashed line.

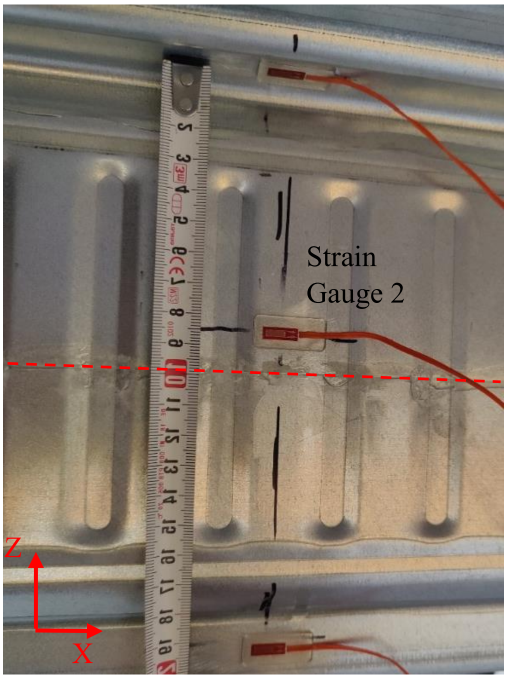

*Figure 4.5. Location of the strain gauge and Fiber 2 on the web of Slab 11.*

The strain levels can be plotted over time for both the strain gauge and one specific measurement point of the optical fiber. When these strain levels overlap, the optical fiber measurement point indicates the position of the strain gauge compared to the fiber data, this is illustrated in Figure 4.6.

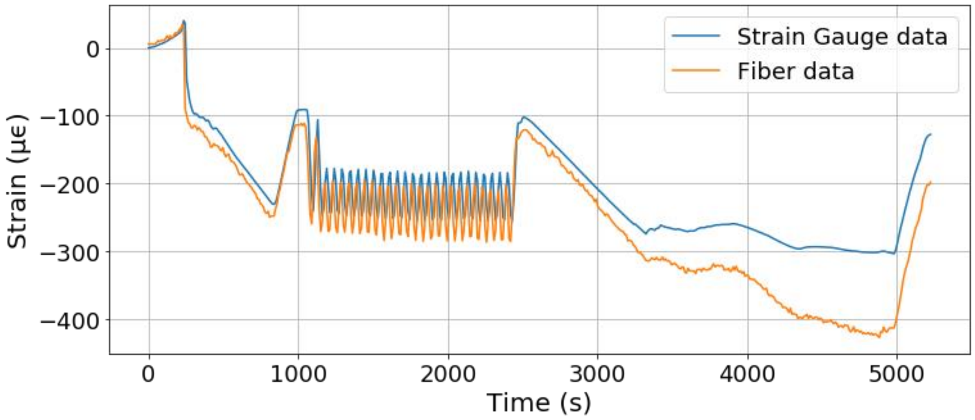

*Figure 4.6. The strain levels over time, of the strain gauge and the corresponding measurement point of Fiber 2, from slab 11.*

Knowing the location of the strain gauge in both the fiber data and the location of the web allows for the determination of strain levels at other parts of the web using the fiber data. The strain level of Fiber 2 is illustrated in Figure 4.7 over a small part of the span at peak load. The location of the measurement point corresponding to the strain gauge is shown in Figure 4.6 is marked by an orange dot, which indicates where the strain gauge is positioned relative to the strain data of Fiber 2. Figure 4.7 also depicts a part of the web that overlaps with the strain data. The location of the strain gauge on the web is shown as a red box. As mentioned before, the strain gauge is positioned on the left side of the flat part of the web. It can be observed that the strain is positive in the indentation part of the web, and negative in the flat area of the web. The transition between positive and negative strain mainly occurs in the slanted parts of the web.

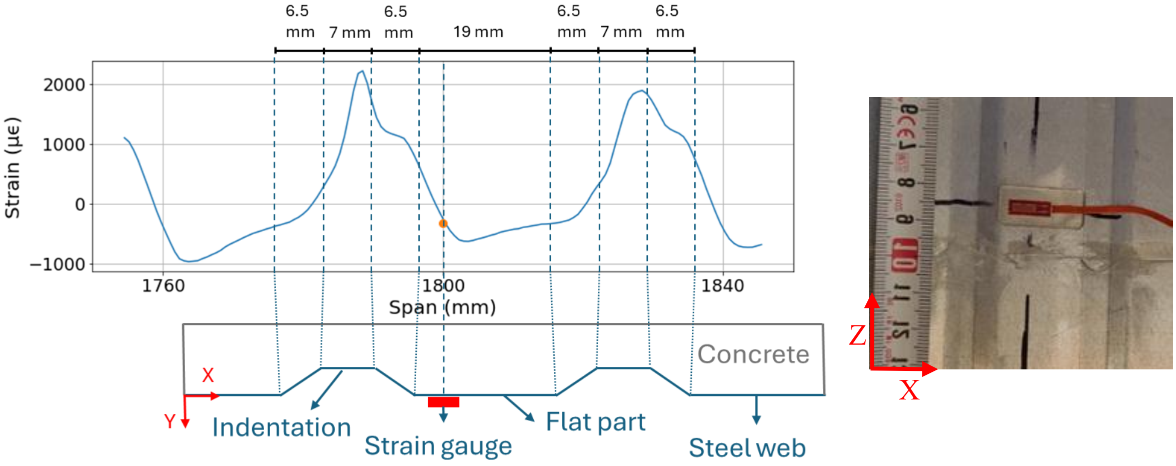

*Figure 4.7. The strain of Fiber 2 overlaps with a small part of the steel web (left), and a photo of the strain gauge location on the flat part of the web (right), Slab 11.*

### 4.1.2. Top flange embossments

Fiber 4 and Fiber 5 are applied on embossments of the steel top flange. These two fibers also have strain gauges applied in roughly the same locations, which is illustrated in Figure 4.8. For Slab 10 there is no data from Fiber 4 and 5 since the fibers broke before testing. Only Slabs 6, 11, and 12 will be discussed in this section.

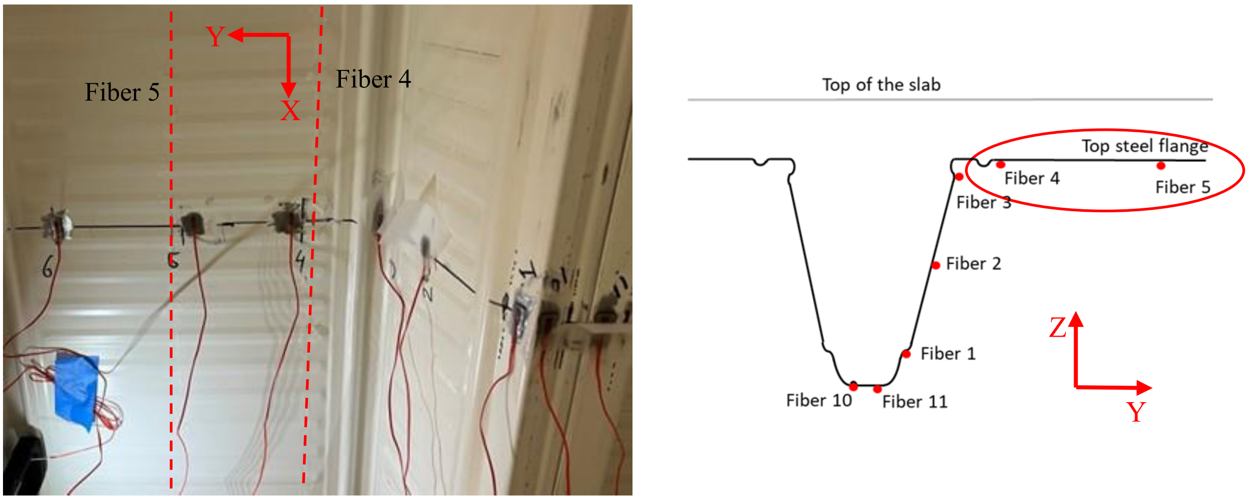

*Figure 4.8. Overview of the fiber locations.*

### Slab 11

The measurement point of the fiber data corresponding to the strain gauge is identified similarly to the process used for Fiber 2. The overlapping strain measurements for strain gauge 4 and Fiber 4 are illustrated on the left side of Figure 4.9, while strain gauge 5 and Fiber 5 are depicted on the right side of Figure 4.9 and Figure 4.10.

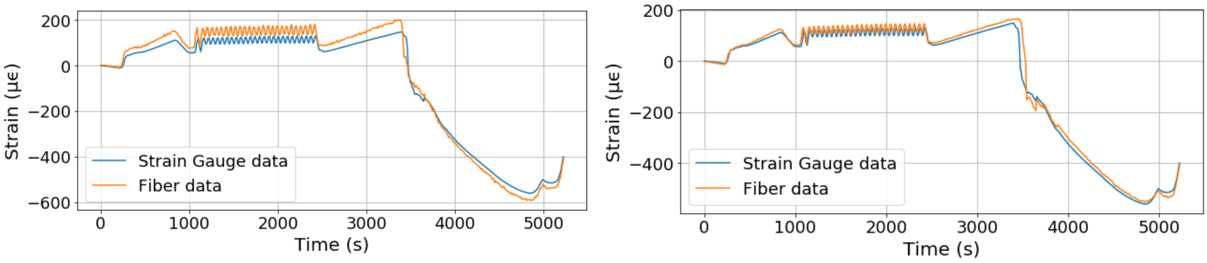

*Figure 4.9. The strain levels over time, of the strain gauge and the corresponding measurement point of Fiber 4 (left), and Fiber 5 (right), from Slab 6.*

Figure 4.10 shows the strain of Fiber 4 over a small portion of the span at peak load, the measurement point corresponding to the strain gauge is highlighted with an orange dot. Additionally, it shows in the photo that the strain gauge is applied to the left side of the flat part of the web, this means that in the fiber data, the strain gauge is also on the right side of the flat part. The same has been done for Fiber 5 which is illustrated in Figure 4.11. The strain gauge was also moved to the left side of the flat part.

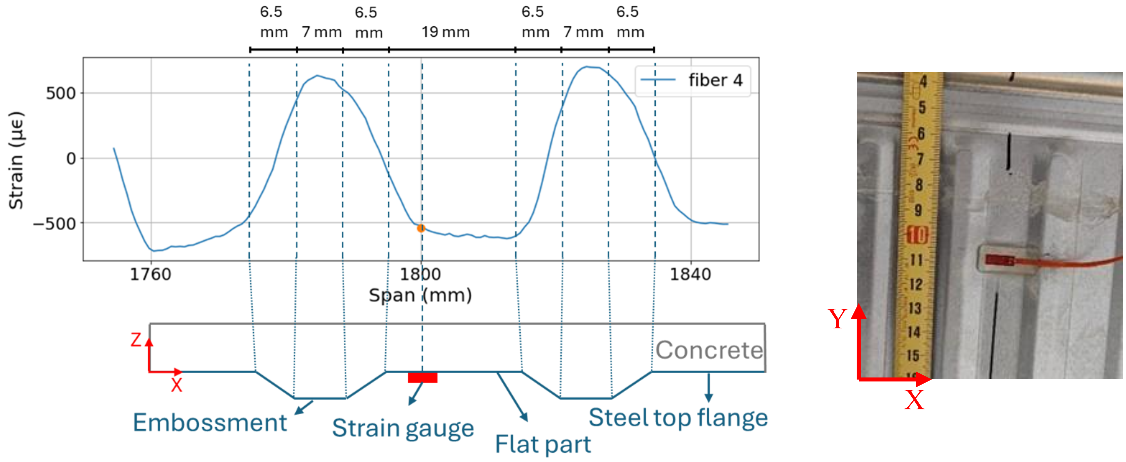

*Figure 4.10. The strain of Fiber 4 overlaps with a small part of the steel top flange (left), and a photo of the strain gauge location on the flat part of the flange (right), for Slab 11.*

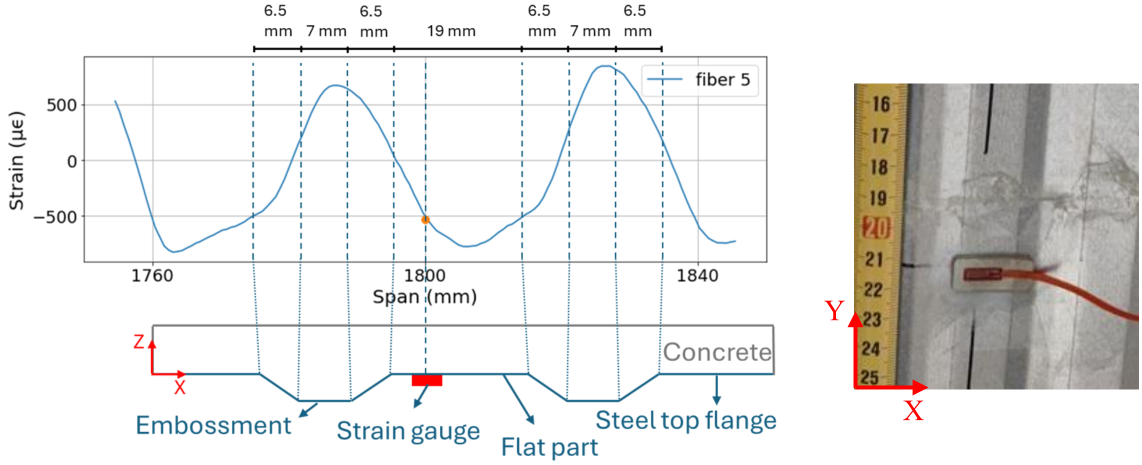

*Figure 4.11. The strain of Fiber 5 overlaps with a small part of the steel top flange (left), and a photo of the strain gauge location on the flat part of the flange (right), for slab 11.*

Figure 4.10 and Figure 4.11 present results that are quite similar. In both cases, a tension peak is observed in the embossment region of the top flange, while the flat section of the flange exhibits compressive stresses. These findings are consistent with the behaviour observed for Fiber 2, as discussed in the previous section, even though the layout of the steel sheeting is different for the top flange and the web. These results are also consistent with the findings of the other slabs which are shown in Appendix B.

## 4.2. Cause of the oscillations

Fibers 2, 4, and 5 are positioned on the embossments and indentations, and exhibit oscillations in their strain data. In contrast, the fibers applied to the flat sections of the steel sheeting do not show these oscillations, instead they display relatively constant strain values. This suggests that the oscillations are caused by local effects associated with the embossments/indentations.

The previous section showed that the positive tension peak is located at the embossment/indentation section of the web and that the flat region is in compression. This was the case for both the web and the flange, even though the profiles are different. Firstly the web of the steel sheeting will be looked at;

**The web**

Fiber 2 is positioned at the centre of the web, which consistently experiences tension. As the web undergoes tension, the slanted sections tend to flatten, generating bending moments within the web. This occurs because the connections between the indentations, the slanted part, and the flat section are rigid, resisting deformation. The resulting deformations and bending moments within the web under tension are depicted in Figure 4.12.

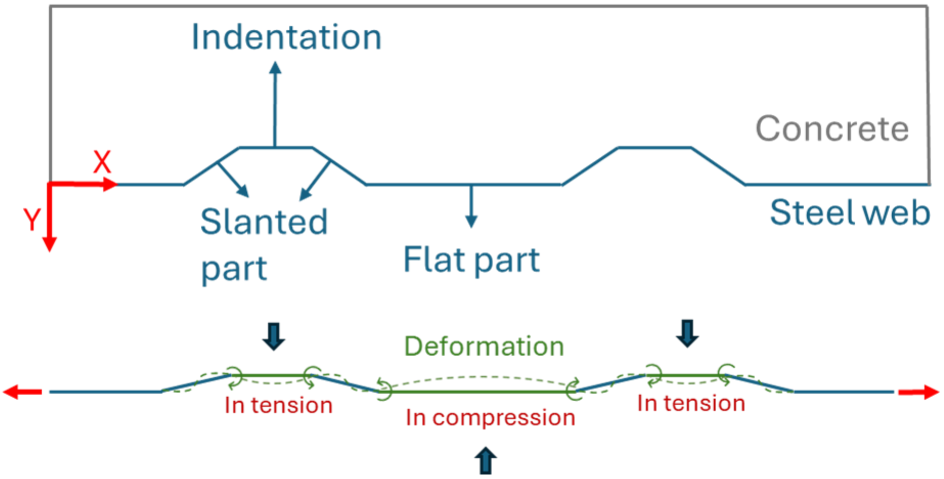

*Figure 4.12. Deformations of the web under tension.*

Figure 4.12 shows that tensioning causes the flat part to bend upwards, causing compression on the bottom of the flat part, where the fiber is located. The indentation bends downwards, which causes tension on the bottom of the indentation.

**The top flange**

The top flange of the steel sheeting is different from the web, the top flange has embossment and the web has indentations. Another difference between the web and the flange is that the web is under tension and the flange is under compression if oscillations are present. This can be checked with Fiber 3, which is located close to the top flange of the steel sheeting. If Fiber 3 is in compression then Fibers 4 and 5 must also be under compression since they are located above Fiber 3. This is illustrated using an example in Figure 4.13, it shows the strain of Fibers 3, 4, and 5 along the span of Slab 12 at one load level. The load level is indicated in the load-displacement graph in Figure 4.14.

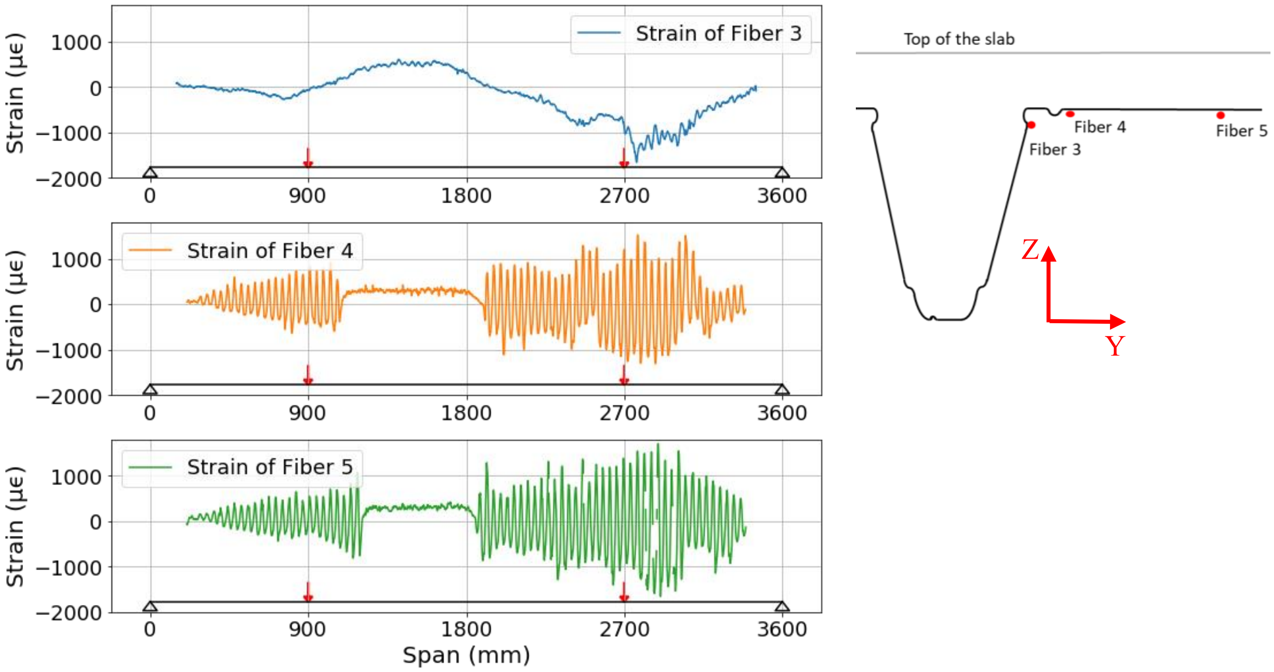

*Figure 4.13. Strain of Fiber 3, 4, and 5 over the span of slab 12.*

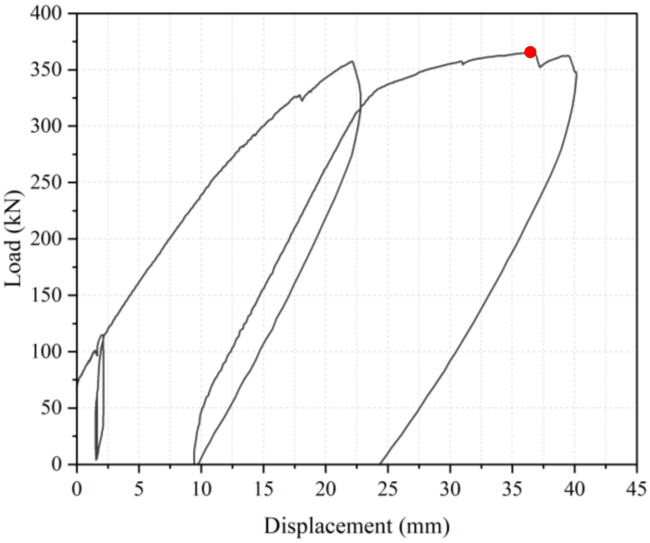

*Figure 4.14. Load-displacement graph of Slab 12.*

The top flange of the steel sheeting is under compression, which is opposite to the web which was under tension. This means that instead of the slanted parts flattening out, they increase in height. The flat part and embossment move away from each other. This causes deformations and bending moments that are illustrated in Figure 4.15.

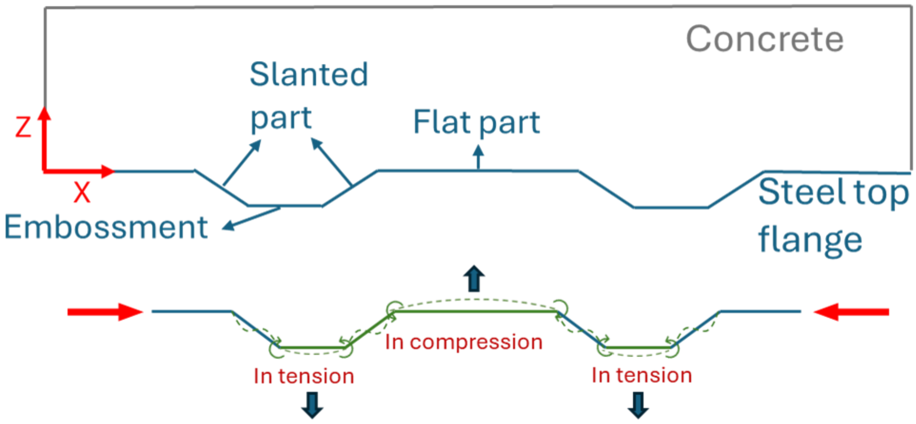

*Figure 4.15. Deformations of the top flange under compression.*

Figure 4.15 shows that the flat part bends upwards, which causes the bottom to be in compression, which is where the fiber is located. The embossment bends downwards, causing the bottom to be in tension. These results are very similar to the results of the web, which was under tension.

It can be concluded that the oscillations in the web are caused by local effects of the indentations due to the tensioning of the web. The oscillations in the top flange are caused by local effects of the embossments due to compression of the flange.

## 4.3. Concluding remarks

The strain data revealed oscillations in the embossed regions, causing the steel sheeting to be in compression and tension. In the web, these oscillations began forming during the cyclic loading phase, while in the top flange, they emerged later, during the static loading phase.

Throughout the test, the web remained in tension. However, the strain data indicated that when oscillations appeared, the indented parts of the web were in tension, while the flat sections were in compression. This behaviour can be attributed to the local effects of the geometry of the indentations: the indented part bends downward, creating tension, while the flat part bends upward, causing compression.

When oscillations are present in the fiber data of the top flange, it is in compression as opposed to tension in the web. Despite this difference, the strain data shows similar results. The flat part is in compression and the embossed part is in tension. Again, this can be attributed to the localized effects of the geometry of the embossment: the embossed part bends downward, creating tension, while the flat part bends upward, causing compression.

# 5. Neutral axis position

When a slab is loaded, bending moments cause stresses distributed along the height of the cross-section. In the conducted tests, compression occurs at the top of the slab, while tension occurs at the bottom. The neutral axis (N.A.) is the location within the cross-section where the normal stress is zero. Determining the neutral axis is crucial as it shows which parts of the cross-section are in tension and which are in compression. This is needed to compute the bending moment resistance and longitudinal shear resistance according to Eurocode 4 [4]. The Distributed Optical Fibers (DOFs) are applied at several different positions along the height of the steel cross-section, which is illustrated in Figure 5.1. Through interpolation of the fiber data, the location of the neutral axis can be found. However, not all fibers are applied on flat steel, Fiber 2, 4, and 5 are on the embossed part of the steel sheeting. This causes these fibers to give different results from the fibers on flat steel. The local effects of the embossments have to be removed to fit the trend of the other fibers.

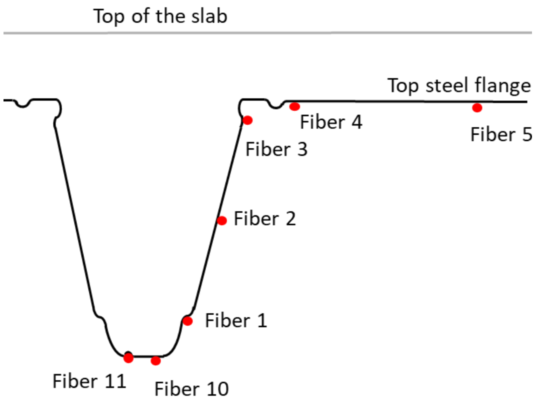

*Figure 5.1. Side view of the middle rib indicating the fiber locations.*

## 5.1. Theoretical position of the neutral axis

The theoretical position of the neutral axis (N.A.) can be determined at three distinct stages of loading: the initial, elastic, and plastic stages. For the initial and elastic loading stages, the N.A. is located at the centroidal axis of the cross-section. In the plastic stage the method described in Eurocode 4 [4] can be used. Understanding the N.A.'s position during these stages is crucial for accurately assessing the behaviour of a composite section. The theoretical position can indicate how the position of the N.A. found by the fibers should change at different loads. Detailed calculations for each stage are provided in Appendix C.

**Initial loading stage**

In the initial loading stage, the load gradually increases from 0 kN. It is assumed that the concrete is uncracked and capable of carrying tensile forces. However, it’s important to note that concrete has a relatively low design tensile strength, approximately 1.2 MPa for C25/30 concrete [21]. Despite this, analysing the N.A.'s position during this stage provides valuable insight into the early behaviour of the composite section. At this stage, since the concrete contributes to the tensile zone of the slab, the neutral axis is positioned at the centroidal axis of the entire cross-section. This includes the concrete which is in tension.

For this initial stage, the N.A. is located 86.4 mm from the top of the slab, which is in the steel sheeting. This is the case for slabs that have a reinforcement rebar in their ribs which are Slabs 6 and 12. However, the rebar is not present in Slab 11 which alters the N.A. position to 85.0 mm from the top of the slab.

**Elastic loading stage**

As the load increases beyond the initial stage, the tensile forces in the concrete intensify until the concrete begins to crack. Once cracking occurs, the concrete no longer contributes to tensile resistance, and all tensile forces are carried solely by the steel components in the tension zone. During the elastic stage, the structure exhibits linear elastic behaviour, where stress is directly proportional to strain. The N.A. shifts due to the cracking of the concrete. In the elastic stage, the neutral axis moves to 48.7 mm from the top of the slab, positioning it entirely within the concrete and above the steel sheeting. For Slab 11 this value is 45.2 mm since it does not have a rebar in its ribs.

**Plastic loading stage**

When the structure reaches the plastic stage, its behaviour changes significantly. For shallow steel-concrete composite slabs, it is assumed that the steel is fully yielding and the concrete has reached its ultimate compressive strain. The neutral axis now represents the boundary between the fully yielded tensile steel and the fully compressed concrete. Determining the N.A.'s location at this stage is essential for assessing the ultimate moment capacity of the section.

However, for deep slabs the assumption that all steel sheeting in the tension zone is yielding might not apply, it could be the case that part of the steel sheeting is not yielding. This is confirmed with the data of Fiber 2 from Slab 11, which is located in the middle of the web. It has an average strain value of 1416 με between the load points at peak load. The strain (ε) in combination with the stiffness (E) of the steel sheeting can be used to calculate the stress (σ) experienced by Fiber 2, which is located in the middle of the web;

$$\sigma = \varepsilon * E = 1416 * 10^{-6} * 0.21 * 10^{6} = 297\ MPa$$

This shows that Fiber 2 and the top half of the steel sheeting are not yielding at peak load. Thus, the position of the plastic neutral axis cannot be calculated with the method described in Eurocode 4 [4]. Instead, an existing Finite Element model is used to obtain the position of the plastic neutral axis. The model found an N.A. position of 32.5 mm from the top of the slab at the peak load [22]. The geometry of Slabs 6 and 12, which include reinforcement in their ribs, was used in the model. Although Slab 11 lacks a rebar in its ribs, which would slightly affect the results, the same N.A. position of 32.5 mm from the top of the slab will be used.

To summarise; it is expected that the position of the N.A. starts in the steel sheeting, then relatively quickly during the elastic stage it shifts upwards until it is fully in the concrete, above the steel sheeting. After the elastic stage, the N.A. will shift further upwards during the plastic loading stage.

The values mentioned above are for Slab 12 which has a reinforcement rebar in its ribs, Slab 6 also has a rebar in its ribs and therefore has the same theoretical positions of the neutral axis. Slab 11 has no reinforcement rebar in its ribs which causes the N.A. position to be different in all loading stages. The results are summarised in Table 5.1.

*Table 5.1. Expected positions of the neutral axis.*

| *Loading stages* | *N.A. position of Slabs 12 and 6* | *N.A. position of Slab 11* |
|---|---|---|
| *Initial* | 86.4 mm | 85.0 mm |
| *Elastic* | 48.7 mm | 45.2 mm |
| *Plastic* | 32.5 mm | 32.5 mm |

## 5.2. Inclusion of the embossment fibers

For Fiber 2 the local effects of the embossments can be filtered out to fit in the strain profile of the other fibers. Fiber 2 has oscillations in its strain data, to get a strain value without local effects, the maximum values of the positive peaks and the minimum values of the negative valleys are needed. Figure 5.2 shows the strain of Fiber 2 along the span between the load points, the maximum values are indicated with green markers, and the minimum values with red markers. The average of the maximum peak values and the average of the minimum valley values is taken, which is indicated with dashed lines. The left and right sides of the slab might not be symmetrical, the averages are therefore taken separately for both sides.

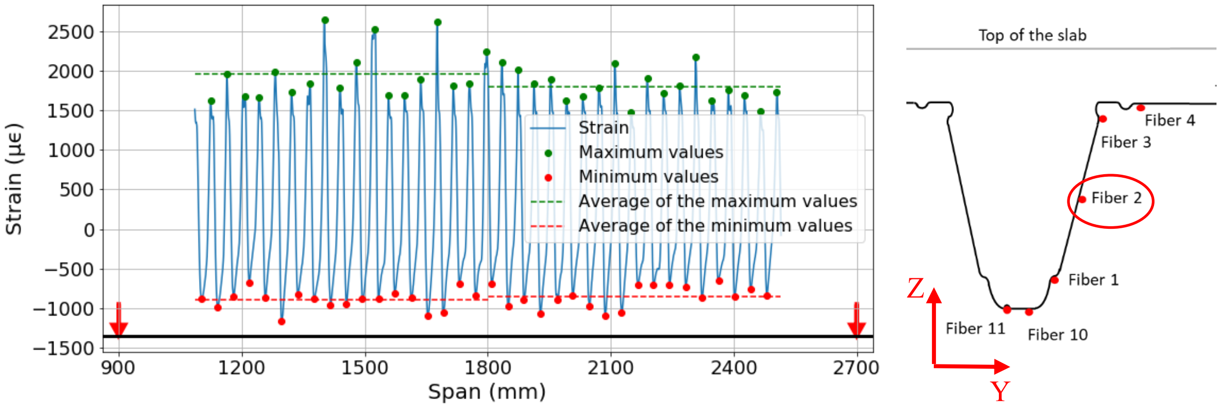

*Figure 5.2. Strain of Fiber 2, slab 11, indicating the maximum and minimum values.*

Figure 5.2 illustrates that the data considered does not cover the entire span of the slab. Instead, only a portion spanning 715 mm to the left and right of the midpoint is analysed. This limited focus is intentional to avoid including areas near the load points, which may be influenced by the load application and could alter the results. These left mid and right mid areas are highlighted in Figure 5.3.

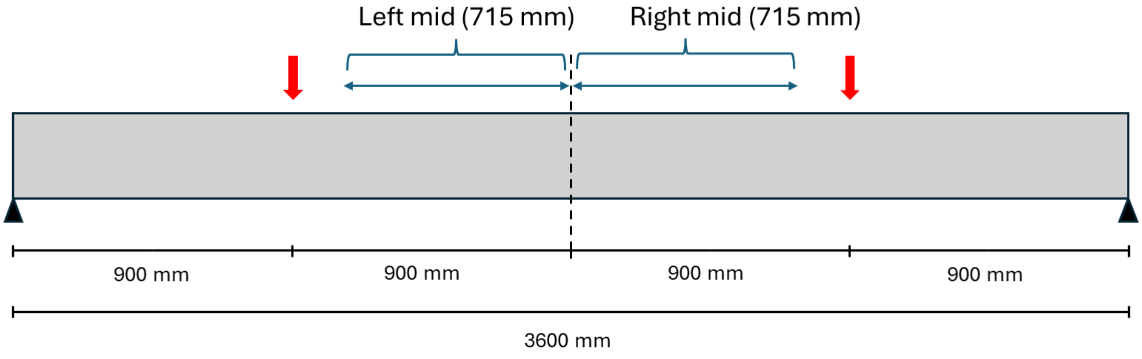

*Figure 5.3. Side view of a 3.6-meter slab, highlighting the regions where the neutral axis is calculated.*

To obtain strain values usable in N.A. calculations, the average of the maximum and minimum values have to be added up. This means that in the example shown in Figure 5.2 the strain value of Fiber 2 would be 1959 + (-899) = 1060 με for the left side, and 1798 + (-848) = 950 με for the right side. This can be done for all measurements, creating strain values of Fiber 2 that can be used to find the position of the neutral axis.

Fibers 4 and 5 are applied to the embossments on the top flange of the steel sheeting and show oscillations similar to Fiber 2. However, the method used to obtain strain values for calculating the neutral axis is ineffective for Fibers 4 and 5, and an alternative method has not yet been found. Fiber 4 and 5 will therefore not be used in calculations of the neutral axis.

## 5.3. Neutral Axis position

For the determination of the neutral axis (N.A.) position, Fibers 1, 2, 3, 10, and 11 will be used, these fibers are applied on the middle rib. The locations of individual fibers are shown in Figure 5.4.

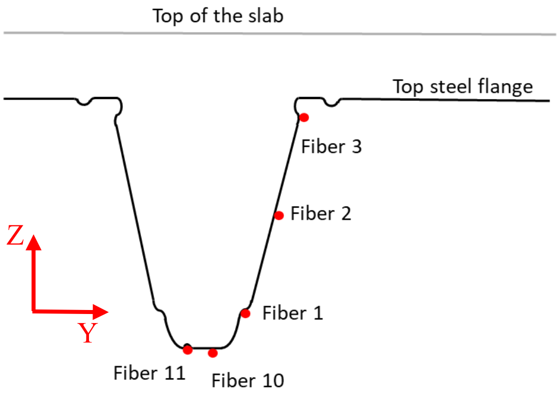

*Figure 5.4. Location of the fibers.*

The neutral axis in a cross-section is the location where the strain value is zero. When a structure is subjected to elastic loading, the strain distribution over the height of the cross-section is linear. In this case, there are five strain levels distributed over the height of the cross-section. Since the strain distribution is linear, a straight line can be fitted through these points. The point at which this line intersects the zero-strain axis represents the location of the neutral axis.

As discussed in the previous section, the neutral axis will be determined separately for both the left and right sides of the slab. Figure 5.3 illustrates this for a slab with a span of 3.6 meters. The strain values through which the line will be fitted are obtained by calculating the mean values of each of the fibers, this is done for both the left and right middle areas of the slab.

The fitting of the line through the strain values is accomplished using the least squares method, a widely used technique for linear regression. The least squares method aims to find the best possible fit for a set of data points by minimizing the discrepancies between the data and the fitted line [23]. Specifically, it minimizes the sum of the squares of the errors, which are the vertical distances between the data points and the corresponding points on the fitted line. Squaring the errors is to ensure that all deviations, whether positive or negative, are treated equally, and to place greater weight on larger errors. By minimizing this sum of squared errors, the least squares method produces a line that best represents the overall trend in the data.

The postprocessing of the data was carried out using Python, specifically utilizing the Numpy package. Numpy provides a function called ‘polyfit’, which is designed to fit data to a polynomial function using the least squares method. For this analysis, the ‘polyfit’ function was employed to fit the strain data to a first-degree polynomial, effectively generating a linear fit. This allows for the precise determination of the neutral axis based on the strain distribution.

Slab 12 will be utilized to illustrate how the results were obtained, it has a span of 3.6 meters and it has a reinforcement rebar in its ribs and colour-coated steel sheeting. Slab 12 was loaded until it reached a peak load of 366 kN. Firstly, the results of the fibers applied to the steel in the middle rib will be discussed, followed by the results of the fibers applied to the concrete side of the slab.

### 5.3.1. Middle rib fibers

A straight line is fitted through five data points, as illustrated in Figure 5.5 for the left middle side and Figure 5.6 for the right middle side. These figures represent the static loading phase of the test, after the cyclic loading. The load levels corresponding to this phase are shown in the load-displacement graph in Figure 5.7. The neutral axis position is the point where the fitted line intersects with the zero strain axis. The steel sheeting yield point is 1775 με which is indicated with a red dashed line. It shows that at 300 and 356 kN part of the steel sheeting is yielding.

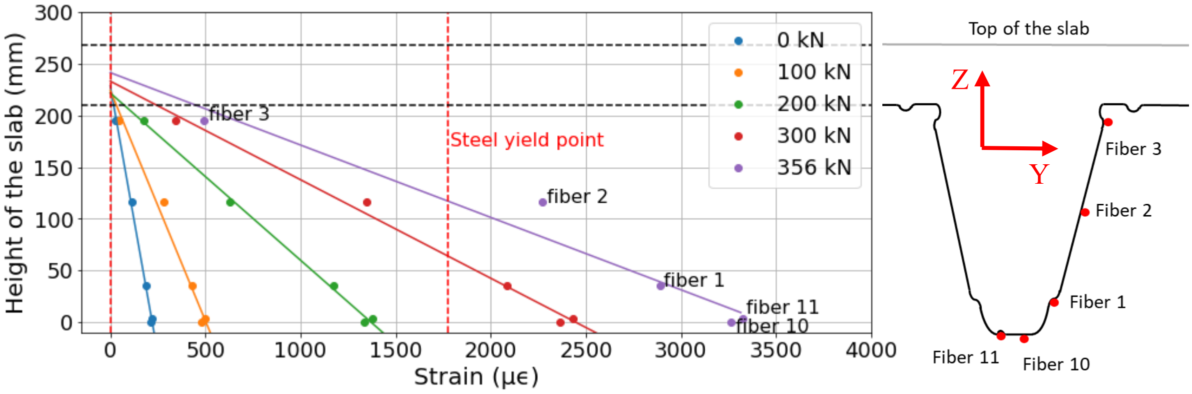

*Figure 5.5. Strain distribution of the* ***left*** *middle side of Slab 12, with a fitted line through the measurements.*

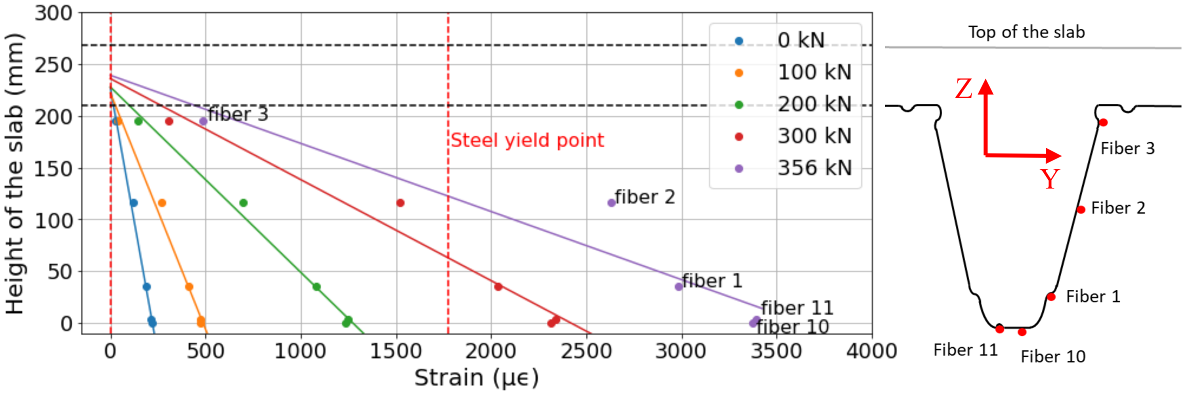

*Figure 5.6. Strain distribution of the* ***right*** *middle side of Slab 12, with a fitted line through the measurements.*

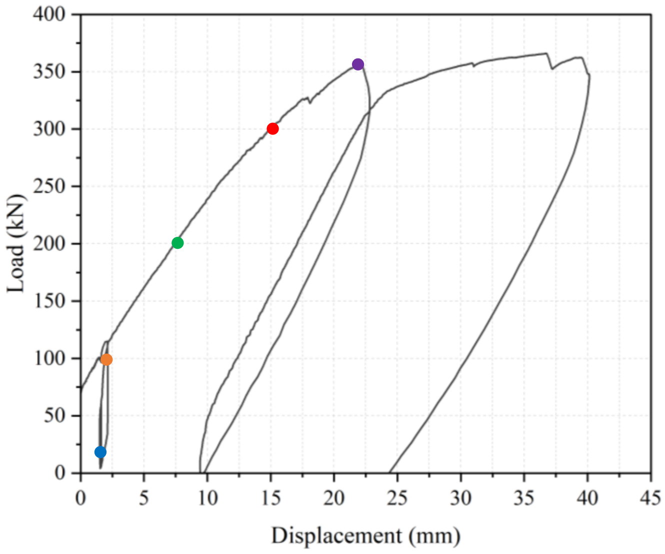

*Figure 5.7. Load-displacement graph of Slab 12.*

Figure 5.5 and Figure 5.6 display very similar trends. Both figures show that under elastic loads, the strain of Fiber 2 aligns well with the strain levels of the other fibers. For Slabs 6 and 11, the results closely resemble those presented in Figure 5.5 and Figure 5.6 and are included in Appendix C for reference. These figures demonstrate that during lower load levels in the elastic stage, the strain measured by Fiber 2 aligns consistently with the strains observed in the other fibers. However, as the load increases and the slab transitions into the plastic loading stage, Fiber 2 exhibits slightly higher strain values compared to the others. This discrepancy indicates that the strain distribution across the fibers becomes nonlinear under higher load conditions.

### 5.3.2. Concrete Fiber

The Concrete Fiber is only applied on Slab 12, it is located on the concrete side of the slab which is highlighted with a red box in Figure 5.8.

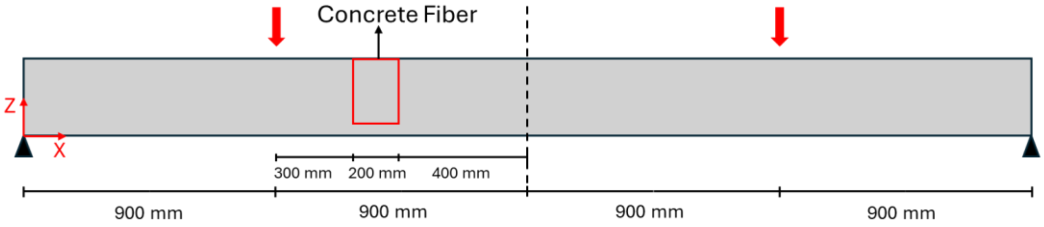

*Figure 5.8. Side view of Slab 12, highlighting the location of the concrete Fiber.*

The Concrete Fiber gives the average strain over a distance of 200 mm, measured at intervals of 15 mm from the top surface. The strain distribution along the slab height (Z-direction) is depicted in Figure 5.8. The applied load levels remain consistent with those used in the previous section, as shown in the load-displacement curve in Figure 5.7.

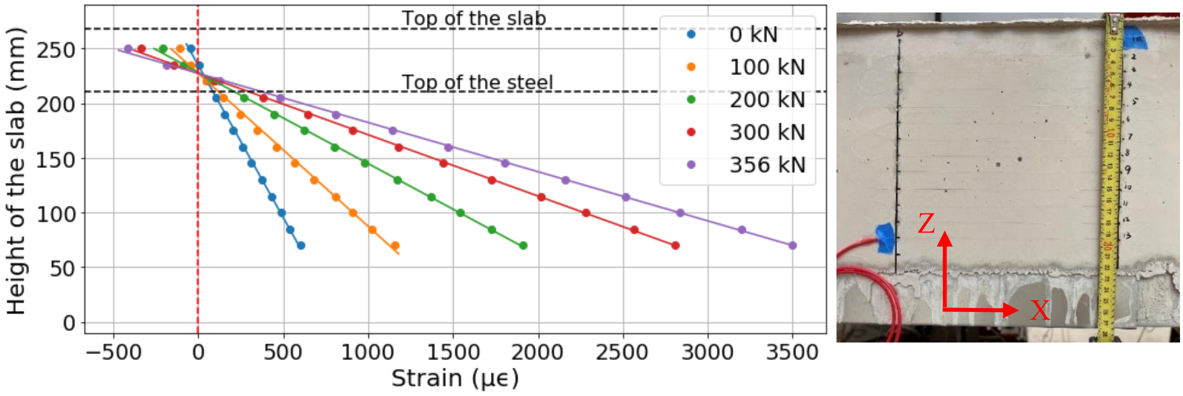

*Figure 5.9. Strain results of the concrete Fiber.*

The Concrete Fiber has slightly different results than the Fibers applied on the middle rib. The N.A. starts relatively high in the slab and then shifts downwards slightly, whereas the middle rib fibers start lower and then shift upwards. Furthermore, the strain distribution of the concrete Fiber remains linear, as opposed to the middle of the slab where the strain distribution became non-linear at higher loads.

A difference between the Concrete Fiber N.A. and the middle rib N.A. is expected due to the different locations. The middle rib is constrained on all sides, while the slab's edge has an unconstrained side, allowing it to deform more freely.

## 5.4. Neutral axis position results

The N.A. location was found at three different loading stages; the initial, elastic, and plastic loading stages. Firstly the initial stage will be discussed.

### 5.4.1. Initial loading stage results

For the initial loading stage, the start of the test will be examined because after the cyclic loading concrete cracking will occur. At this stage, the theoretical position of the N.A. is in the steel at approximately 86.4 mm from the top of the slab.

Slabs 11 and 12 had a short static loading stage before the cyclic loading part, the maximum load was equal to the maximum load level of the cyclic loading part. The loading rate of this first static part was much slower than in the cyclic loading part, this was done to enable the visual identification of cracks forming. However, this also gives more fiber measurements at the start of loading which enables the N.A. calculation of the initial loading stage. For Slab 6 this was not done, which leaves only 2 measurements in the initial loading stage, Slab 6 is therefore left out of this section. The location of the N.A. has been determined at a load level of approximately 0 kN. The N.A. position is given as the distance to the top of the slab in Table 5.2. As a reference, the top of the steel sheeting is 55 mm from the top of the slab.

*Table 5.2. N.A. position for the initial loading stage.*

| *Slab 12, N.A. position (mm)* | | | *Slab 11, N.A. position (mm)* | |
|---|---|---|---|---|
| Left | Right | Concrete Fiber | Left | Right |
| 74.5 | 77.0 | 114.1 | 92.9 | 88.3 |

Table 5.2 shows that the results of Slab 12 are in line with the expectations mentioned before, the N.A. starts in the steel sheeting. However, the values of the N.A. position deviate from the expected values.

The fiber results show that the N.A. starts at 74.5 and 77.0 mm, which is above the expected start point of the N.A. position, it was 86.4 mm according to the theoretical N.A. position found in section 5.2. The Concrete Fiber starts deeper in the slab than expected. The N.A. position of Slab 11 also starts in the steel sheeting at 92.9 and 88.3 mm, this is higher than the theoretical value, which was 85 mm. As the load increases, the N.A. position shifts upwards, this is shown in the following section.

### 5.4.2. Elastic and plastic loading stage results

The results of the elastic and plastic loading stages are discussed together since they follow each other. The elastic part of the loading can be considered as up to 80 % of the peak load, after this point, the plastic stage starts. The results of the N.A. position are given for different load levels, which are shown as a percentage of the peak load.

**Slab 12**

Slab 12 has a span of 3.6 meters, it has colour-coated steel sheeting, and it experienced a peak load of 366 kN. Figure 5.10 illustrates how the position of the N.A. changes as the load increases for both the left and right side of the middle rib and the Concrete Fiber on the side of the slab.

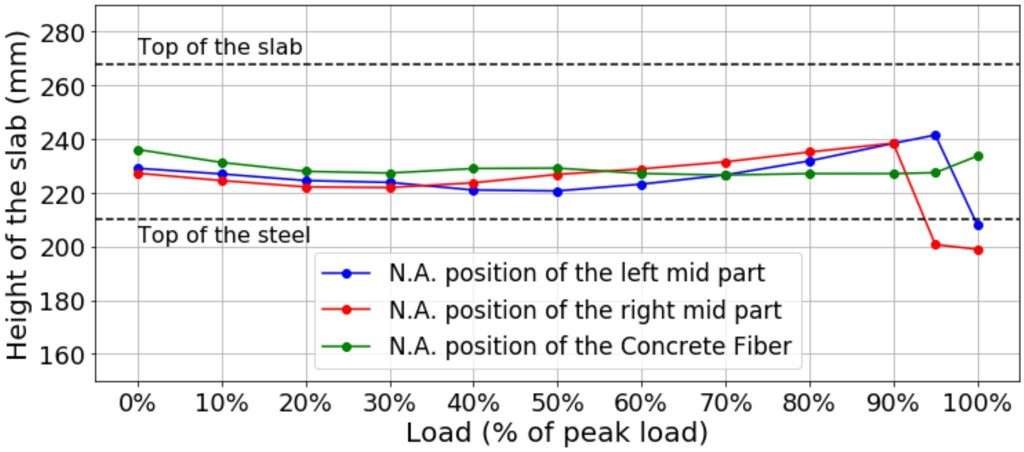

*Figure 5.10. The N.A. position of Slab 12 at load levels ranging from 0% to 100% of the peak load of 366 kN.*

All three locations showed similar results for the elastic loading stage with a relatively constant N.A. position above the steel sheeting, which is in line with expectations. Additionally, as the load increases the N.A. shifts upwards slightly which is expected in the plastic stage. However, after 90% of the peak load, the N.A. shifts downwards in the middle rib, even though it is expected to shift upwards. The Concrete Fiber on the side of the slab does have the expected upward shift in N.A. position. This difference between the results is likely due to the loss of shear interaction between the steel sheeting and the concrete, resulting in partial composite interaction.

The loss of shear interaction between the steel sheeting and the concrete is confirmed by the measured slip at the supports. This slip, occurring between the two materials, is illustrated for both sides of Slab 12 in Figure 5.11. The data shows that slip begins to increase at around 97% of the peak load on the left side and continues growing until the test's conclusion. On the right side, slip initiates slightly earlier, at approximately 95% of the peak load. A brief pause in the testing procedure, during which the slab was unloaded, is visible in the right-side graph. The slip on the left side occurred after this pause, which is why it is not visible in the left graph.

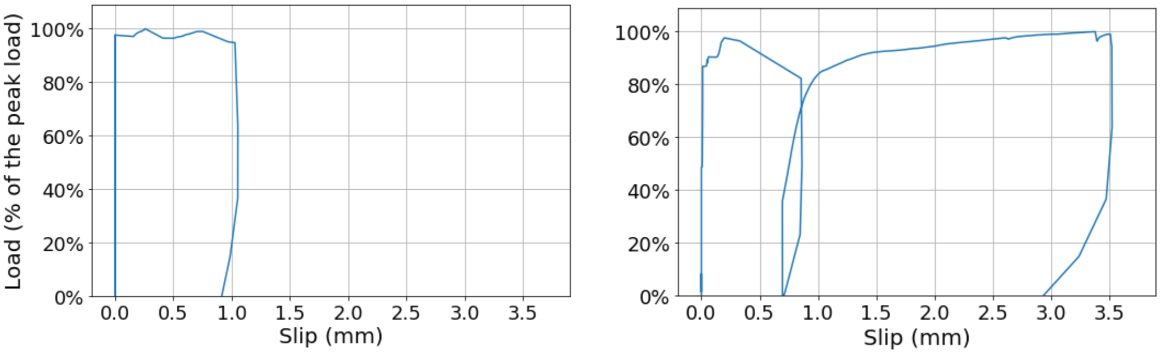

*Figure 5.11. Slip measured at the supports at different load levels on the left side of Slab 12 (left), and on the right side of Slab 12 (right).*

Additionally, oscillations observed in the strain data from the fibers located in the top flange correspond with the initiation of slip. These oscillations become evident in the later stages of the test, starting at around 97% of the peak load for the left side and at 95% for the right side. This correlation suggests that the oscillations in the top flange are indicative of slip and partial composite interaction between the steel sheeting and concrete. The strain data highlighting the sudden formation of oscillations on the right side of the slab is shown in Figure 5.12. The strain of Fiber 4 is shown over the span at two load levels, these load levels are highlighted in the load-displacement curve on the right side of Figure 5.12. The oscillations forming on the left side of Fiber 4 and the results of Fiber 5 are shown in Appendix C.3.

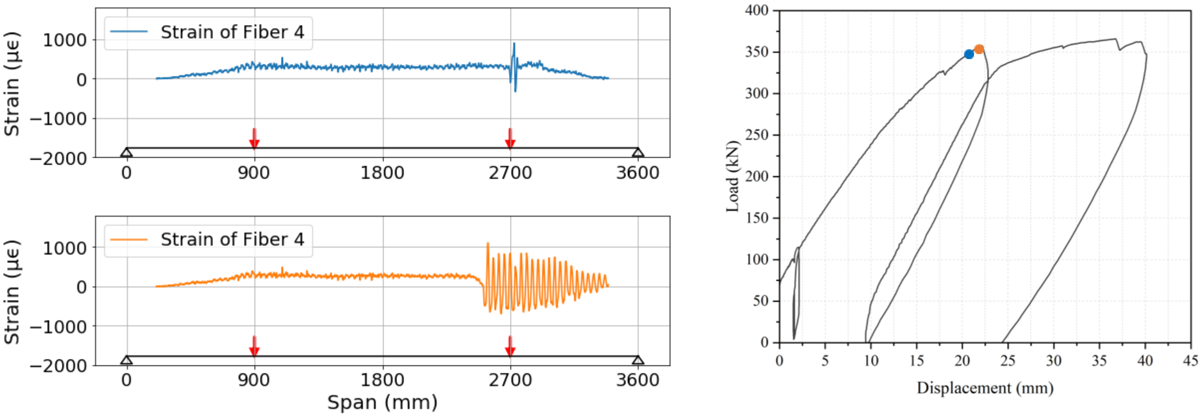

*Figure 5.12. Strain of Fiber 4 over the span at two load levels (left), and the load-displacement curve indicating the load levels (right).*

For Slab 12 the N.A. position in the elastic stage is taken as the average of the values from 0% to 70% of the peak load which results in a N.A. position of 40 mm from the top of the slab. The N.A. position in the plastic stage is 62 mm from the top of the slab which is at peak load.

The concrete fiber has a neutral axis position of 36 mm from the top of the slab, and during the plastic loading stage, the N.A. position is 31 mm from the top of the slab which is at the peak load.

### Slab 11

Slab 11 had a span of 3.6 meters, no reinforcement rebar in its ribs, and experienced a peak load of 217 kN. Figure 5.13 illustrates how the position of the N.A. changes as the load increases for the left and right middle of the slab.

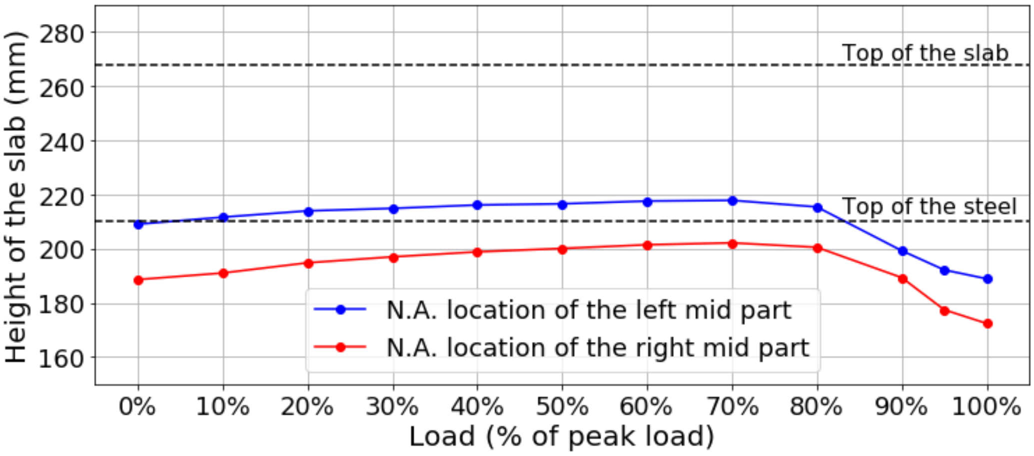

*Figure 5.13. The N.A. position of Slab 11 at load levels ranging from 0% to 100% of the peak load of 217 kN.*

The N.A. position of Slab 11 is lower than expected, which is especially the case for the right middle part of the slab. According to the elastic loading stage calculations, the N.A. is expected to be above the steel sheeting. However, Figure 5.13 does show a similar trend to the results of Slab 12, in the plastic stage the N.A. shifts downwards further, which starts between 70% and 80% of the peak load. Again, this can be attributed to the loss of shear interaction between the steel sheeting and the concrete. For Slab 12 the oscillations in the strain data of the top flange occurred between 70% and 80% of the peak load, which indicates the start of the loss of shear interaction.

The slip at the left and right sides of Slab 11 is illustrated in Figure 5.14, the load levels are shown as a percentage of the peak load. For Slab 11 a small amount of slip occurred during cyclic loading, approximately 0.3 mm on the left side and 0.6 mm on the right side. Then, at 85% of the peak load, the slip increases significantly, up to 7.7 mm on the right side of the slab, and 1.1 mm on the left side. The initial slip indicates that there was already a loss of shear interaction between the steel sheeting and concrete during the cyclic loading part, which could cause the N.A. position to be lower than expected during elastic loading. Similarly to Slab 12, the occurrence of slip coincides with the formation of oscillations in the top flange. The oscillations forming in the strain data of Fibers 4 and 5 are shown in Appendix C.

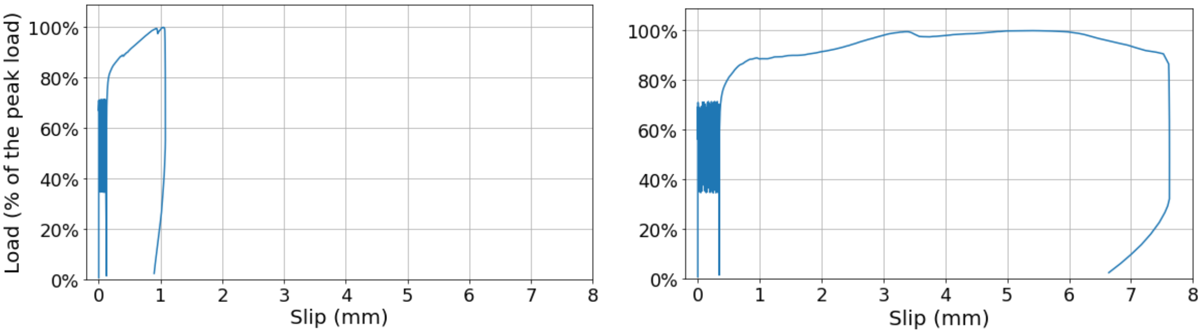

*Figure 5.14. Slip measured at the supports at different load levels, on the left side of Slab 11 (left), and the right side of Slab 11 (right).*

The N.A. position in the elastic stage is taken as the average of the values from 0% to 70% of the peak load which results in an N.A. position of 59 mm from the top of the slab. The N.A. position in the plastic stage is 84 mm from the top of the slab which is taken at the peak load.

**Slab 6**

Slab 6 had a span of 5.4 meters and it experienced a peak load of 220 kN. Figure 5.15 illustrates how the position of the N.A. changes as the load increases for the left and right side of the slab.

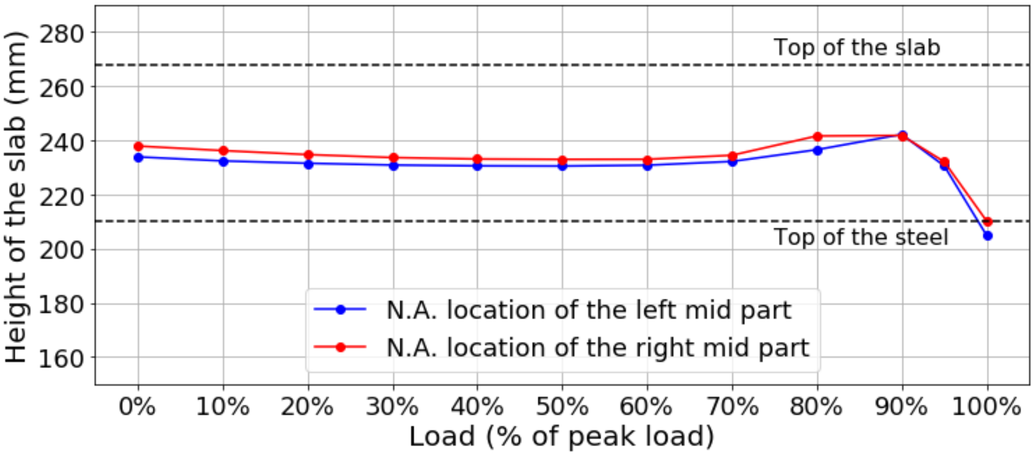

*Figure 5.15. The N.A. position of Slab 6 at load levels ranging from 0% to 100% of the peak load of 220 kN.*

Slab 6 has similar results to Slab 12; in the elastic stage, the position of the N.A. starts in the concrete, above the steel sheeting, for both the left and right middle parts of the slab. Then, at the start of the plastic stage, the N.A. shifts upwards slightly as the load increases, which is expected. However, after 90% of the peak load the N.A. shifts downwards, deeper into the slab, which is unexpected. The loss of shear interaction is indicated by the oscillations in the fiber data of the top flange just like it did for Slab 11 and 12. For Slab 6 the oscillations start to form between 80% and 90% of the peak load.

The slip of Slab 6 at different load levels is illustrated in Figure 5.16. For Slab 6 the slip initiates at approximately 85% of the peak load on the left side and 80 % on the right side. However, the slip increases significantly at approximately 90% of the peak load for both the left and right side of the slab. This again confirms that the N.A. shifts downwards if the slab experiences slip. Similarly to Slabs 12 and 11, the occurrence of slip coincides with the formation of oscillations in the top flange. The formation of oscillations in the strain data of the top flange is shown in Appendix C.

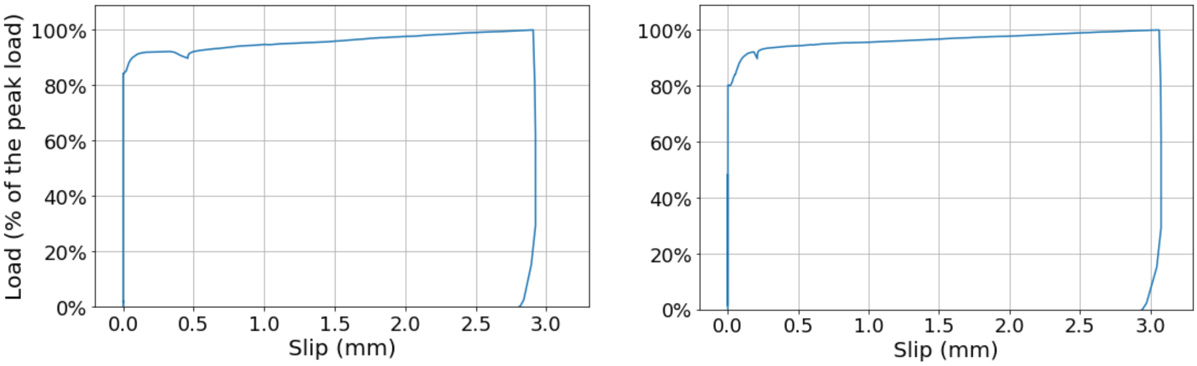

*Figure 5.16. Slip measured at the supports at different load levels, on the left side of Slab 6 (left), and the right side of Slab 6 (right).*

The N.A. position in the elastic stage is taken as the average of the values from 0% to 70% of the peak load which results in an N.A. position of 32 mm from the top of the slab. The N.A. position in the plastic stage is 57 mm from the top of the slab which is taken at the peak load.

## 5.5. Concluding remarks

The available fiber locations can be utilized to calculate the neutral axis (N.A.) of the slab. Including the fiber positioned on the web, which spans across the embossments, helps achieve a more evenly distributed strain profile. Including more fibers along the height of the slab enhances the accuracy of the found neutral axis, as it allows for the inclusion of more data points. However, as the load approaches the peak load, the strain distribution becomes increasingly non-linear, reducing the accuracy of linear curve fitting. At lower loads, where the strain distribution remains linear, the curve fitting is more reliable.

The N.A. position results of the fibers and the theoretical predictions are summarized in Table 5.3. There were notable differences between these slabs. Slabs 11 and 12 spanned 3.6 meters, whereas Slab 6 spanned 5.4 meters. Additionally, Slabs 12 and 6 had a reinforcement rebar in their ribs, while Slab 11 did not.

*Table 5.3. Summary of the N.A. position results.*

| | *Slab* | *Theoretical N.A. position (in mm from the top of the slab)* | *N.A. position found by the fibers (in mm from the top of the slab)* |
|---|---|---|---|
| *Initial stage* | 12 | 86.4 | 75.8 |
| | 11 | 85.0 | 90.6 |
| *Elastic stage* | 12 | 48.7 | 40 |
| | 11 | 45.2 | 59 |
| | 6 | 48.7 | 32 |
| *Plastic stage* | 12 | 32.5 | 62 |
| | 11 | 32.5 | 84 |
| | 6 | 32.5 | 57 |

The neutral axis (N.A.) position determined by the fibers applied to the steel sheeting of the middle rib followed the expected trend during the initial and elastic loading stages across all three slabs. The N.A. starts in the steel sheeting and as the load increases the N.A. shifts upwards above the steel sheeting in the concrete. Although the general trend was consistent, the value of the actual N.A. position deviates from the theoretical value. Particularly in Slab 11, there is a large difference between the theoretical N.A. position and the result from the fibers. In the elastic stage, the N.A. was positioned deeper within the slab at 59 mm from the top of the slab, while the theoretical value was 45.2 mm. This difference is due to a loss of shear interaction occurring during the cyclic loading part. Slab 11 had no reinforcement rebar in its ribs while Slabs 6 and 12 did, this is likely the cause of the difference between the slabs.

During the initial and elastic stage, the Concrete Fiber readings closely aligned with those obtained from the middle rib, suggesting that in these stages, the fibers attached to the steel sheeting of the middle rib can reliably be used to determine the N.A. position of the slab.

However, in the plastic loading stage, the N.A. position derived from the middle rib fibers deviated from the theoretical position and the Concrete Fiber's N.A. position. Instead of shifting upwards, as predicted by the FE model, the N.A. moved downwards into the steel sheeting. In contrast, the concrete fiber readings continued to follow the expected trend. This suggests a loss of shear interaction between the steel sheeting and the concrete, leading to partial composite interaction. The loss of shear interaction is confirmed by the slip measured at the supports, between the steel sheeting and concrete. The downward shift of the N.A. coincided with an increase in slip for all three slabs. As a result, the N.A. positions of the steel sheeting and the concrete should be considered separately in the plastic stage. Therefore, in this phase, fibers attached to the steel sheeting alone cannot accurately determine the N.A. position of the slab, instead they give the N.A. of the steel sheeting alone.

# 6. Buckling detection

Buckling is a phenomenon where a structure or component of a structure deforms suddenly under compressive stress, often leading to failure. This typically occurs when a slender structural element, such as a column or beam, experiences a critical load that exceeds its stability threshold. Unlike simple compression, where the material shortens uniformly, buckling involves a sideways deflection, often leading to a sudden and unexpected collapse. The critical load at which buckling occurs depends on several factors, including the material properties, length, cross-sectional area, and shape of the structure, as well as the boundary conditions.

In steel-concrete composite slabs, the steel sheeting is prone to buckling due to its low thickness. Compressive stresses can develop at the top of the steel sheeting, potentially leading to buckling. When buckling occurs, the steel sheeting can only deform away from the concrete, as illustrated in Figure 6.1. In this figure, the fibers crossing the buckling zone are highlighted with a red dashed line; these fibers are numbered 2, 3, 4, and 5. The specific locations of these fibers within the cross-section are depicted adjacent to Figure 6.1. Buckling will cause significant and abrupt variations in strain along these fibers, providing a clear indication of when buckling has initiated. Only Slabs 10 and 11 buckled during testing. Slab 11 will be discussed first because all its fibers remained intact. Slab 10 has less data due to two fibers breaking.

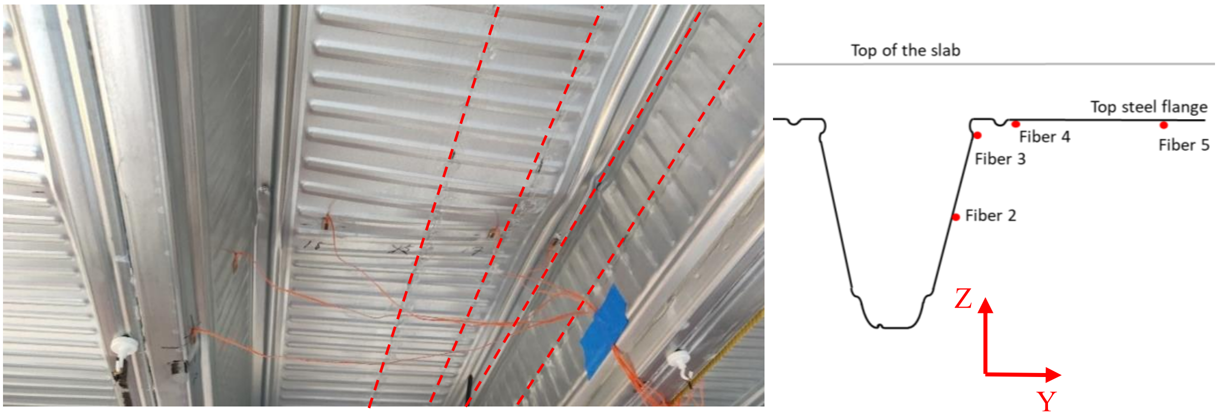

*Figure 6.1. Buckling of steel sheeting of Slab 11 (left), and the fiber locations in the cross-section (right).*

## 6.1. Buckling of slab 11

Slab 11 had a span of 3.6 meters and normal C20/25 strength concrete, it did not have a reinforcement rebar in its ribs. Slab 11 experienced flexural failure at a peak load of 217.6 kN. The steel sheeting of Slab 11 buckled at the right load point, Figure 6.1 shows that only fibers 2, 3, 4, and 5 are affected by the buckling. Fiber 3 is on flat steel, as opposed to embossed steel, and will therefore be looked at first.

### 6.1.1. Fiber 3

Fiber 3 is located on the flat part of the steel sheeting. Since the steel buckles away from the concrete, locally there should be large deformations, both tension and compression. Figure 6.2 shows the strain of Fiber 3 over the span close to the right load point, at 4 load levels, these load levels are indicated in the load-displacement graph of Figure 6.3.

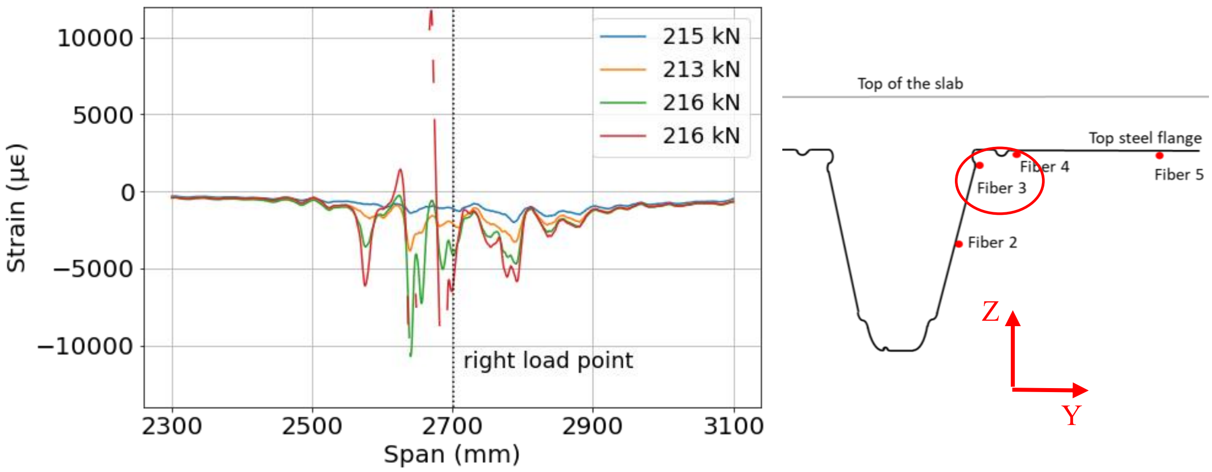

*Figure 6.2. Strain of Fiber 3 at multiple load levels, for Slab 11.*

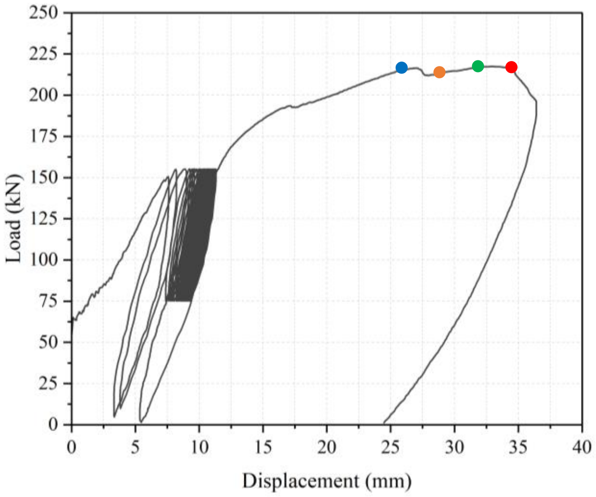

*Figure 6.3. Load-displacement graph of Slab 11.*

Figure 6.2 shows that the compressive strain is initially relatively constant, with the blue graph displaying some minor peaks. However, in later stages, distinct compressive (negative) peaks develop and continue to increase. As expected, positive strain, or tension, forms locally at the last load level. The red graph contains some gaps in its data which is caused by damage to the fiber. The data shows both positive and negative peaks locally, indicating buckling. This formation of these peaks occurs gradually, making it difficult to pinpoint the exact moment when it initiates. However, at 216 kN, which is indicated by the green marker in Figure 6.3, it is clear that buckling occurred. This point is before the peak load of 217.6 has been reached, as a percentage of the peak load this is at 99.3%.

### 6.1.2. Fiber 4

Fiber 4 is positioned on the top flange of the steel sheeting, spanning across the embossments. The strain recorded by this fiber is expected to display relatively consistent oscillations. Figure 6.4 illustrates the strain distribution of Fiber 4 over the span, near the right load point at three different load levels, which are marked on the load-displacement curve in Figure 6.5. As the load increases, the strain data from Fiber 4 reveals the emergence of a significant peak. In the blue curve, a strain increase begins to form, but it is not yet clear that buckling has occurred. However, in the orange curve, corresponding to a load of 211 kN, which is 97% of the peak load, the strain increase becomes more pronounced, indicating buckling.

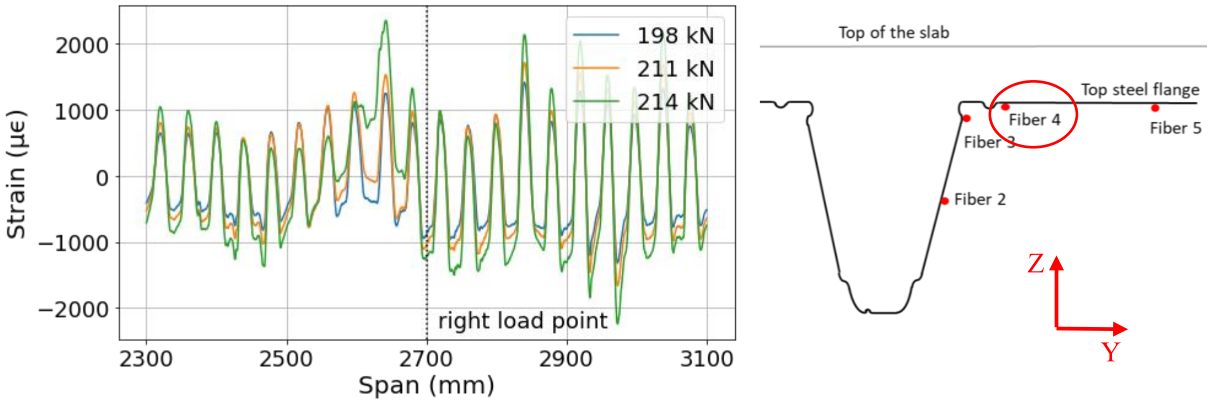

*Figure 6.4. Strain of Fiber 4, indicating buckling, for Slab 11.*

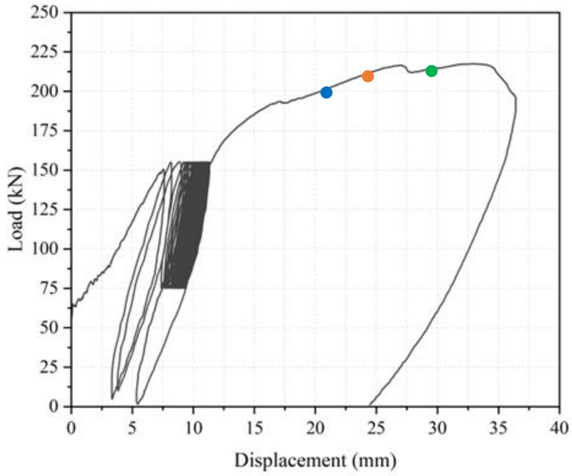

*Figure 6.5. Load-displacement graph of Slab 11, indicating the load levels of Figure 6.4 and Figure 6.6.*

### 6.1.3. Fiber 5

Fiber 5 can also be utilized to indicate buckling, its results are shown in Figure 6.6. The same load levels are used for Fiber 4, which are indicated in the load-displacement graph in Figure 6.5. Fiber 5 is located on the embossments of the top flange just like Fiber 4, but Fiber 4 is located close to the edge and Fiber 5 is in the middle of the embossments. The results are therefore quite similar to each other. The data from Fiber 5 shows that the strain level increases, however, no distinct peak forms. Furthermore, this increase is lower than that of Fiber 4, and the increase starts later. This is likely due to Fiber 4 being closer to the edge of the embossments where the deformations due to buckling are larger, this can be seen in Figure 6.1. Buckling is detected at a load level of 214 kN, which is 98.3% of the peak load.

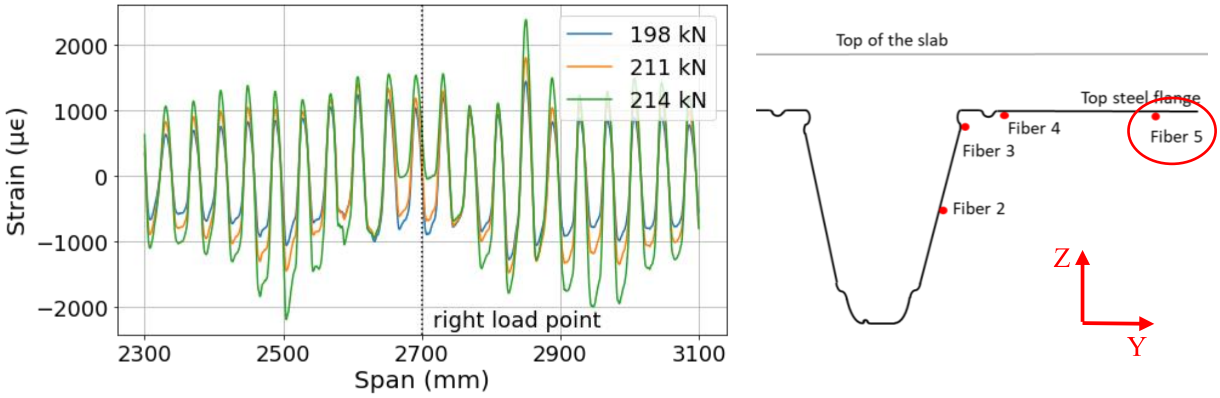

Figure 6.6. Strain of Fiber 5, indicating buckling, for Slab 11.

## 6.1.4. Fiber 2

Lastly, Fiber 2 is also affected by the buckling of the steel sheeting, it is located on the indentations of the web. Figure 6.7 illustrates the strain distribution of Fiber 2 over the span near the right load point at three different load levels, which are also indicated on the load-displacement curve in Figure 6.8. Fiber 2 does not show any signs of buckling at the load levels analysed in the previous section. Instead, this begins to occur at the peak load of 217.6 kN, as depicted by the purple curve in Figure 6.7. Before this point, the strain data is represented by the red curve, which indicates no evidence of buckling. As the test continues and the slab approaches failure, the strain is shown by the brown curve, where the effect of buckling is even more pronounced.

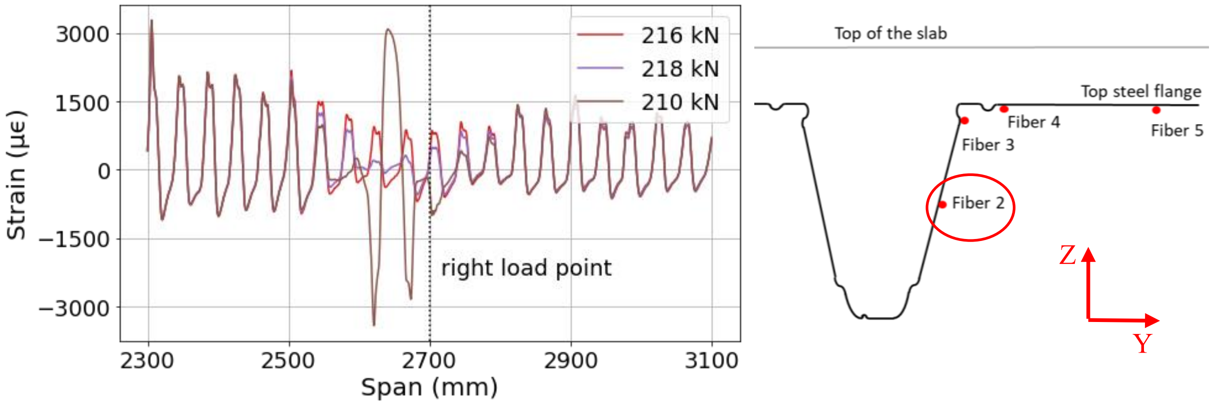

Figure 6.7. Strain of Fiber 2, indicating buckling, for Slab 11.

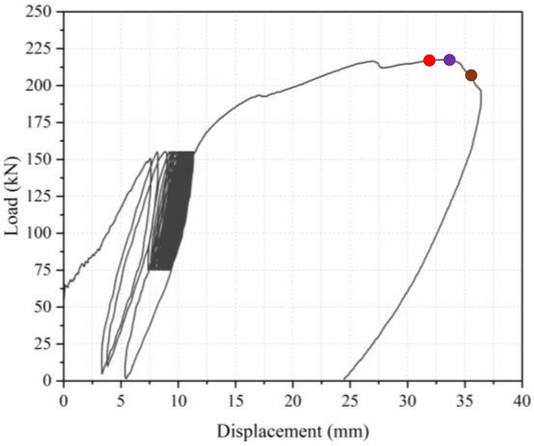

*Figure 6.8. Load-displacement graph of Slab 11, indicating the load levels of Figure 6.7.*

## 6.2. Slab 10

Slab 10 had a span of 3.6 meters and featured rib reinforcement along with recycled aggregate concrete. In contrast, Slab 11 lacked rib reinforcement and had normal C20/25 strength concrete. During the testing, the steel sheet of Slab 10 experienced buckling. Out of the fibers placed in the buckling zone, only Fiber 2 provided usable data because the other fibers broke. Consequently, Fiber 2's data is the only source for analysing the buckling behaviour of Slab 10. Slab 11 showed that Fiber 2 could detect buckling, although it showed indications of buckling later than the other fibers. The buckling of slab 10 is illustrated in Figure 6.9, and Fiber 2 is highlighted with a red dashed line.

*Figure 6.9. Buckling of the steel sheeting of Slab 11.*

The buckling shown in Figure 6.9 occurred close to the right load point. The effect of buckling on the strain of Fiber 2 is illustrated in Figure 6.10, at three load levels. These load levels are indicated in the load-displacement graph of Slab 10 in Figure 6.11.

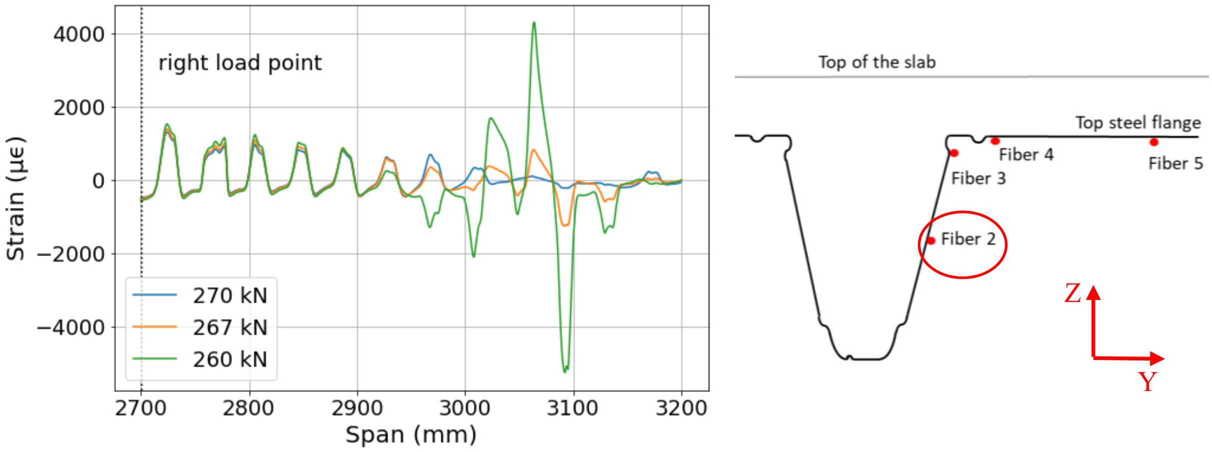

*Figure 6.10. Strain of Fiber 2, indicating buckling of Slab 10.*

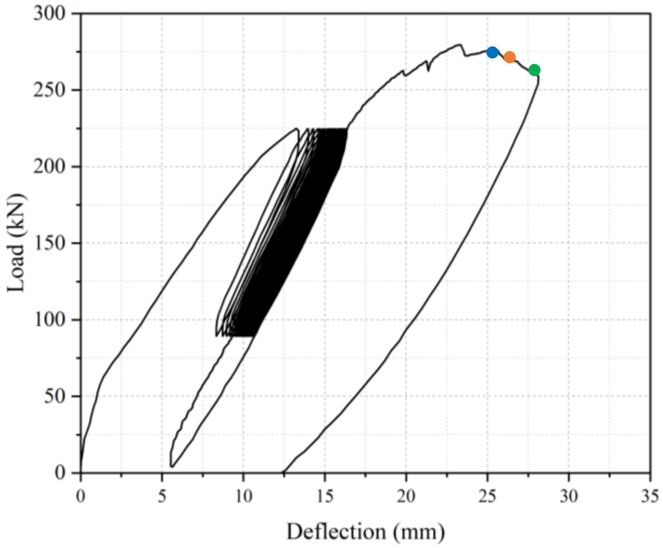

*Figure 6.11. Load-displacement curve of Slab 10, showing load levels of Figure 6.10.*

Figure 6.10 illustrates the transition of relatively uniform oscillations into significantly higher peaks. Additionally, some data points that were initially in compression shift to tension, and those in tension shift to compression. This indicates large deformations of the steel sheeting, signifying buckling. The changes in strain observed in Fiber 2 of Slab 10 are very similar to the strain changes in Fiber 2 of Slab 11, as shown in Figure 6.7. This similarity confirms that the strain changes are caused by buckling, as both slabs experienced buckling at the location of these strain variations. The blue graph in Figure 6.10 is the earliest point where signs of buckling are visible in the strain data, this is at 270 kN, however, from Figure 6.11 it can be seen that this is after the peak load has been reached.

## 6.3. Concluding remarks

In Slab 11, Fibers 2, 3, 4, and 5 were located within the buckling zone, while in Slab 10, only Fiber 2 was in the buckling zone. All fibers displayed deformation patterns which indicated buckling during testing. These observations lead to the conclusion that distributed optical fibers are effective in detecting buckling when applied to steel sheeting. For Slab 11 the buckling was detected before the peak load was reached, Fiber 4 gave the earliest indication of buckling at a load of 211 kN, which is 97% of the peak load. This suggests that the buckling likely began in proximity to Fiber 4. However, this pattern may vary for other slabs, as the location of buckling initiation could differ depending on factors such as local material properties or imperfections.

For Slab 10 the buckling was detected at a load of 270 kN, which is after the peak load has been reached. However, only Fiber 2 was available, if the other locations were available then it could be the case that the buckling was detected earlier since this was also the case for Slab 11.

The fibers provide real-time data that can pinpoint the onset of structural instability, offering valuable insight into the behaviour of the slab under load. This demonstrates their potential as a reliable monitoring tool for early detection of buckling, which can enhance safety and structural performance.

# 7. Concrete cracking

The final objective of this thesis is to determine whether the fibers applied to the steel sheeting can effectively detect the propagation and traces of cracks in the concrete. To achieve this, five fibers were applied to the bottom of each rib of Slab 7. The fibers run along the span in the longitudinal direction. The locations of Fibers 11.1, 11.2, 11.3, 11.4, and 11.5 are shown in the cross-section of Slab 7, illustrated in Figure 7.1. Slab 7 spans 7.2 meters and has reinforcement rebars in its ribs, it experienced a peak load of 142 kN.

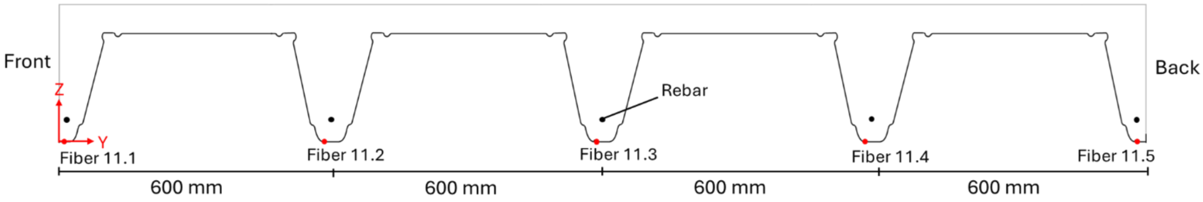

*Figure 7.1. Cross-section of Slab 7, indicating the locations of the fibers.*

## 7.1. Crack detection

Crack openings will lead to localized deformation in the steel sheeting, which generates tension peaks in the strain data recorded by the optical fibers. These tension peaks serve as indicators of the location of the cracks. The cracks are visually identified in the strain data of each fiber. Once the crack locations in each rib are known the crack paths through the slab can be determined. The crack locations found in the slab are compared with the exposed cracks which are visible on the side of the slab. Figure 7.2 shows the right side of Slab 7, the exposed cracks have been marked.

*Figure 7.2. Photo of the front right side of Slab 7.*

Cracks on the left side of Slab 7 were very similar to the cracks shown in Figure 7.2. On both sides the cracks are caused by bending, there are no visible shear cracks. Photos of the left front side and the back side of Slab 7 are shown in Appendix D.

To illustrate the crack identification, the strain data on the right side of the slab, from Fibers 11.1 and 11.2, is shown in Figure 7.3. This data was recorded at peak load to illustrate the fiber data under maximum deformation. The range displayed, from 3600 mm to 6200 mm, is specifically chosen because it represents the zone where cracking was observed, from 6200 mm to 7200 mm no cracks are visible. The peaks that indicate cracks are highlighted with red markers. Only significant peaks were selected as reliable indicators of crack formation, to make sure that the selected peaks represent cracks. The data of the other fibers is shown in Appendix D.

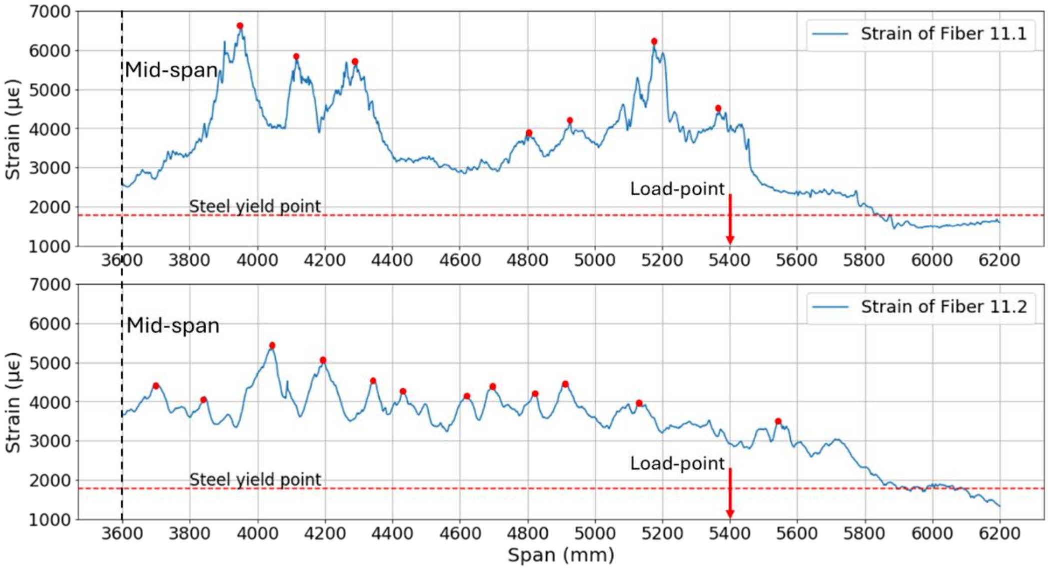

*Figure 7.3. The strain data of Fiber 11.1 (top) and Fiber 11.2 (bottom) on the right side of Slab 7, at peak load.*

There is a difference in strain value between the strain data of the Fibers shown in Figure 7.3. This is because Fiber 11.1 is applied to the outer rib, and Fiber 11.2 is applied to one of the three middle ribs. The difference in the magnitude of strain values can be attributed to the middle three ribs being constrained on all sides, while the outer ribs are constrained on only one side, allowing for greater deformations in the outer ribs. Additional steel sheeting was applied along the sides of the slab, providing a nice finish and formwork at the edges. However, the additional steel sheeting had gaps at several points along the span of the slab. This is illustrated in Figure 7.4, it shows a side view and a bottom view of the gap in the steel sheeting.

*Figure 7.4. Side view (left), and bottom view (right), of the gap in the steel sheeting.*

The gap in the steel sheeting also causes large peaks in the strain data of Fibers 11.1 and 11.5. The large peaks caused by the gaps could cause several peaks to be detected as one large peak, which reduces the accuracy of the crack detection. The gaps are located at 2050, 3080, 4120, and 5170 mm from the left support. Relatively large peaks are located at the same points in the strain data of Fibers 11.1 and 11.5. An example of these peaks in the strain data of Fiber 11.5 at peak load is shown in Figure 7.5.

Additionally, there were gaps at 1000 mm and 6200 mm. However, it can be seen in Figure 7.5 that there are no significant peaks at these locations.

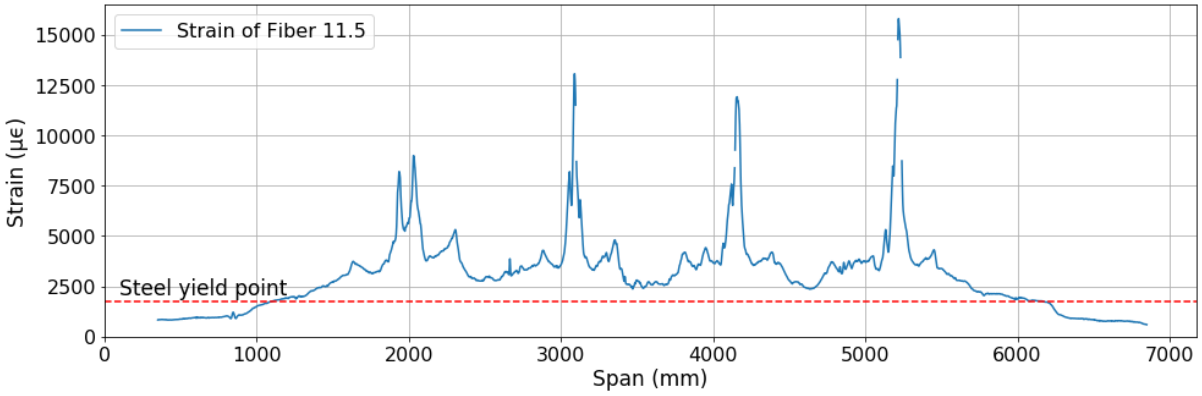

*Figure 7.5. Strain of Fiber 11.1 at the peak load of Slab 7.*

## 7.2. Results

All crack locations have been visualised in a top view of Slab 7, the left side of the slab is illustrated in Figure 7.6. Visible cracks along the edges of the slab are marked with black dots, while cracks detected by the fibers are highlighted with red dots. The fibers themselves are represented by blue lines. Where the crack locations align with each other, they are connected with dashed red lines to indicate correlation. The same approach has been applied to the right side of Slab 7, as illustrated in Figure 7.7.

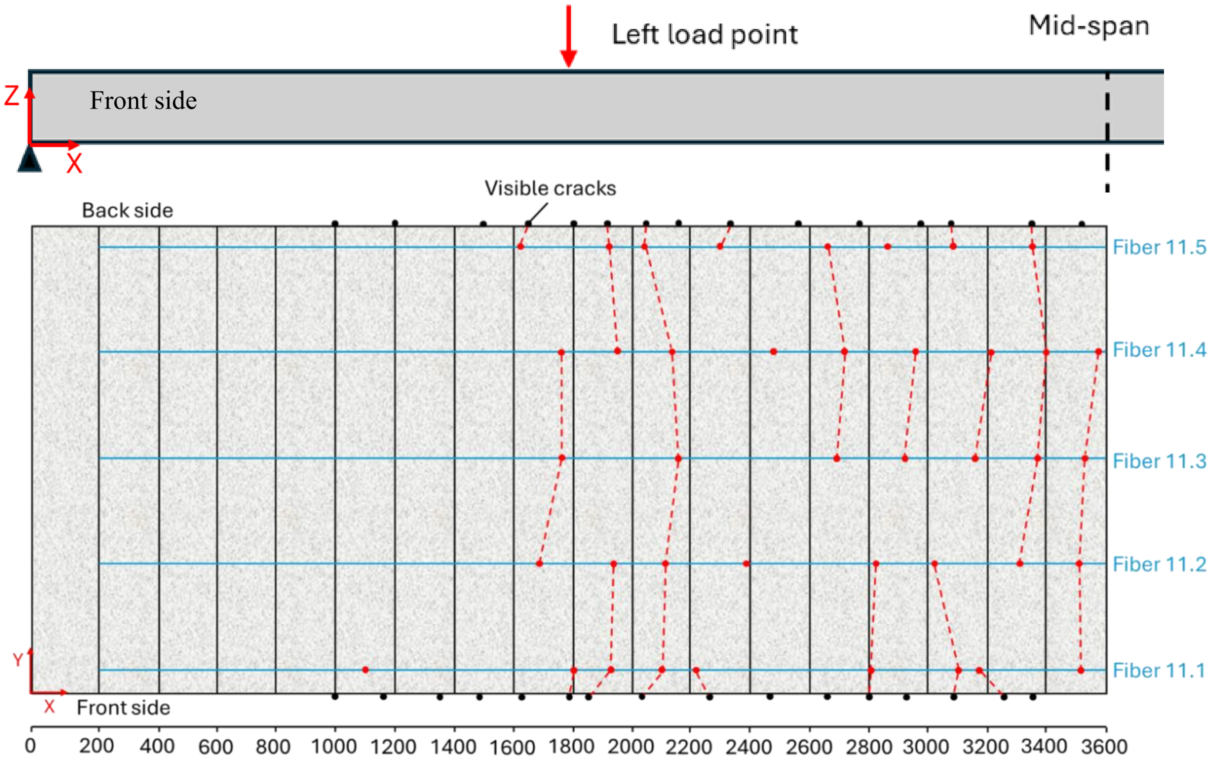

*Figure 7.6. Side and top view of the crack locations through the left side of Slab 7.*

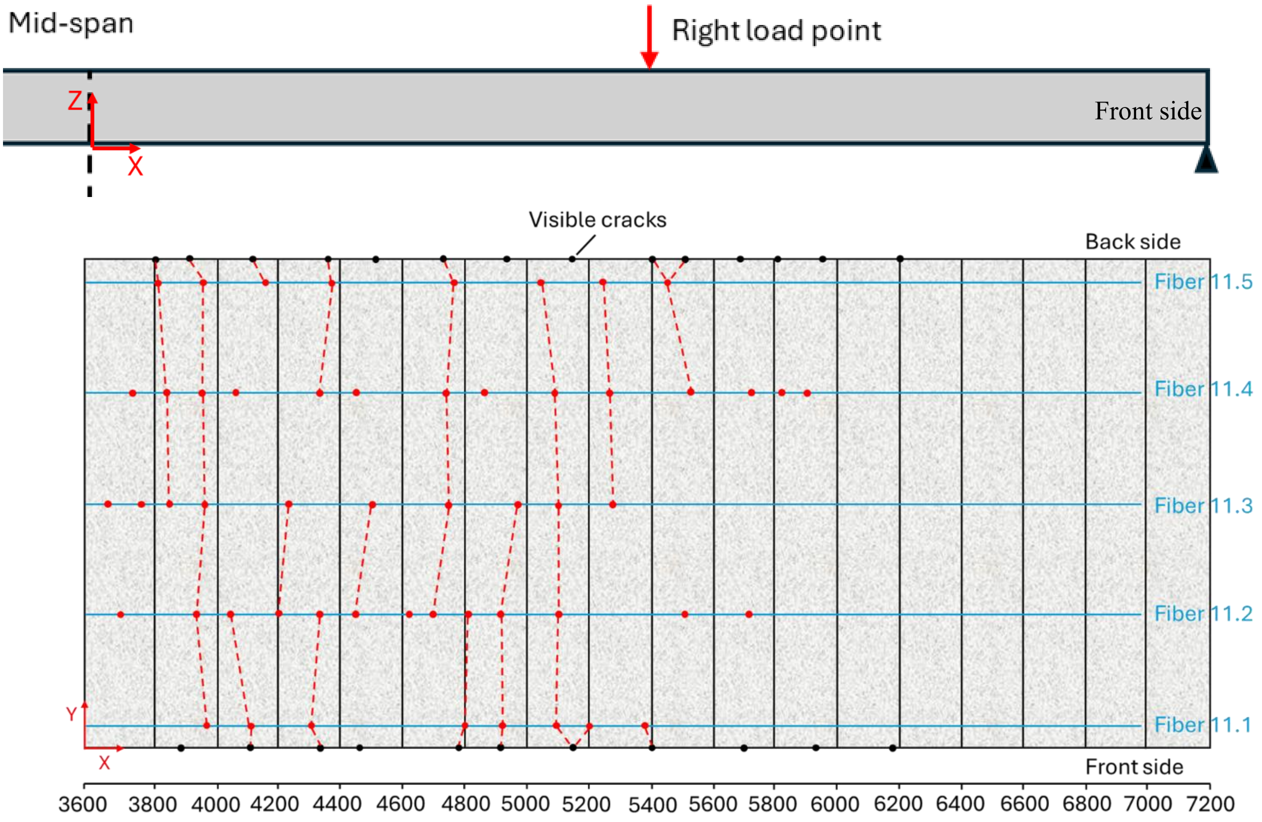

*Figure 7.7. Side and top view of the crack locations through the right side of Slab 7.*

Figure 7.6 and Figure 7.7 illustrate that the visible cracks on both the front and back sides of the slab occur in similar locations. However, these locations did not always correlate with the fiber data. Notably, Fibers 11.1 and 11.5, which are positioned closest to the exposed side of the slab, show the greatest deviation from the observed cracks. This discrepancy is likely due to significant local deformations that cause debonding of the steel sheeting and concrete. This causes multiple cracks to be identified as a single large peak in the strain data. The difference in the magnitude of deformations can be attributed to the middle three ribs being constrained on all sides, while the outer ribs are constrained on only one side, allowing for greater deformations in the outer ribs. Furthermore, there are gaps in the steel sheeting at the sides which cause large strain values, these gaps are shown in Figure 7.4.

The effect of multiple peaks converging into one large peak is illustrated in Figure 7.8, it shows the strain values of the left side of Fiber 11.1 at two loads; 120 kN and at the peak load of 142 kN. The points where multiple peaks converge are highlighted. The load levels are indicated in the load-displacement curve in Figure 7.9, which also shows the cross-section of the slab and the locations of the fibers.

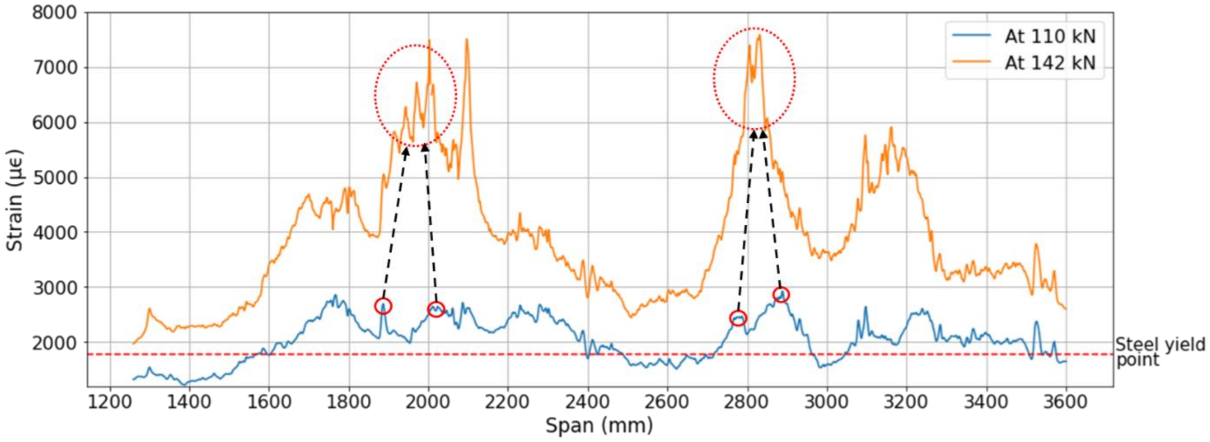

*Figure 7.8. Strain levels of Fiber 11.1 at two load levels, on the left side of Slab 7.*

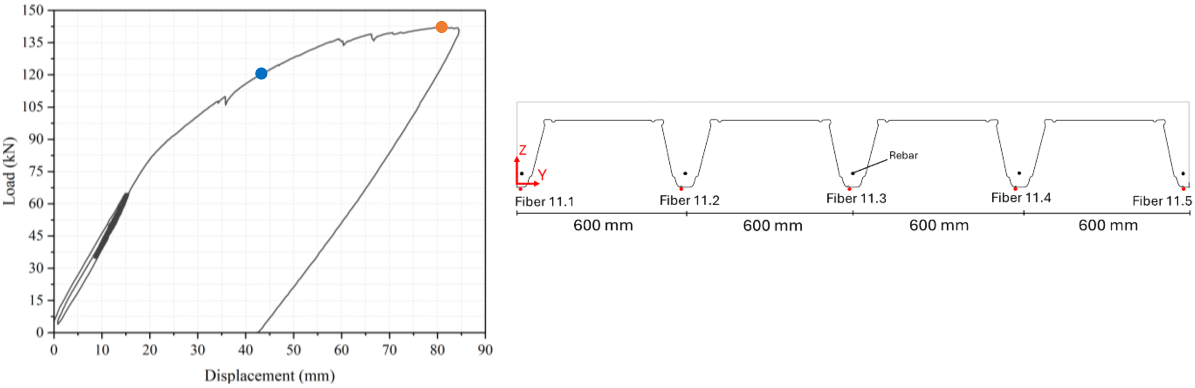

*Figure 7.9. Load-displacement curve of Slab 7 (left), and a cross-section of Slab 7 indicating the fiber positions.*

In contrast, Fibers 11.2, 11.3, and 11.4, located farther from the exposed side, did not exhibit these high strain values, resulting in the detection of more distinct cracks. Though the peaks were more consistent in the three middle ribs than in the outer ribs, the selection of peaks could also be unclear. To increase the certainty of a crack, only significant strain peaks were selected. However, selecting a significant peak is ambiguous, this means that some cracks could cause a strain peak, but were not selected because the peaks were relatively small.

Peak locations were connected with a red dashed line when the difference in location was less than 60 mm. As shown in Figure 7.6 and Figure 7.7, there is only one instance where the top and bottom cracks can be linked, highlighting the inconsistency of crack detection using fiber data. Most peaks were detected at the mid-span between the applied load points. In contrast, significantly fewer cracks were detected in the shear span, despite the presence of visible cracks along the slab edges. This difference is attributed to the nature of bending-induced cracks, which are more common in the mid-span region where the bending moment is largest. The bending moment is larger at mid-span than at the shear spans, which also results in higher strain values, enhancing the detectability of cracks within the strain data.

However, there is no definitive way to verify that the detected crack locations are accurate. Some strain peaks may be attributed to factors other than cracking, further complicating the reliability of the detection by the fibers applied to the steel sheeting.

## 7.3. Concluding remarks

In conclusion, the results shown in Figure 7.6 and Figure 7.7 reveal that the crack detection of the fibers applied to the steel sheeting has limitations in its consistency and reliability. This is attributed to several factors, firstly, it is uncertain which peaks represent a crack, peaks can be relatively small or close to each other, making it difficult to identify cracks. Furthermore, not all cracks that were visible on the side of the slab were detected by the fibers, this is especially the case for the shear spans. Additionally, there can be debonding of the steel sheeting and concrete which causes a larger part of the steel sheeting to deform than only at the crack opening, which can cause two or more cracks to be detected as one. Lastly, there is no definitive way to verify that the detected crack locations are accurate. To confirm that the detected cracks are accurate the steel sheeting would have to be removed from the slab.

# 8. Discussion

The study aimed to investigate the structural behaviour of deep steel-concrete composite slabs using Distributed Optical Fibers (DOFs) for distributed strain measurement during four-point bending tests. The key objectives included understanding strain distribution across embossed regions, determining the neutral axis (N.A.) position, analysing buckling behaviour, and identifying cracks in steel-concrete composite slabs. This section discusses the implications of these findings and highlights areas for future improvement.

## 8.1. Embossment region behaviour

The strain gauges were used to find what parts of the embossed regions were in compression and which were in tension. To identify the measurement point along the length of the fiber corresponding to the strain gauge, strain values over time were compared between the fibers and the strain gauges. Generally, the data from both sources overlapped well, although some fibers did not match the strain gauge data perfectly. This difference is likely due to the locations of the fiber and the strain gauge, they cannot be applied in the same location because they cannot overlap. In these cases, the closest match was selected as the measurement point. Since the results were consistent across all slabs, the chosen measurement points were considered reliable.

## 8.2. Neutral axis position

In calculating the N.A. position, it was assumed that the strain distribution was linear, which was valid during the elastic phase. However, as the load increased beyond 80% of the peak load, in the plastic stage, the strain distribution became increasingly nonlinear. This reduced the accuracy of the NA position since linear curve fitting was used to determine the N.A. position.

Additionally, when there was partial shear interaction, the fibers attached to the steel sheeting only provided the N.A. position for the steel sheeting, not the entire slab. This was demonstrated by Slab 12's data, which showed that the N.A. of the Concrete Fiber aligned with the steel sheeting's N.A. until there was a loss of shear interaction. When shear interaction was lost, the N.A. position of the steel sheeting shifted downward, and the N.A. position of the Concrete Fiber shifted upwards.

For slabs 6 and 12, the partial shear interaction occurred near 90% of the peak load, suggesting that the N.A. position can be reliably estimated for most of the test. However, in Slab 11, partial composite interaction occurred earlier, possibly due to the absence of reinforcement rebar in its ribs, which was present in Slabs 6 and 12. This results in a lower accuracy for the entire static part of loading for Slab 11.

## 8.3. Buckling detection

In both slabs that experienced buckling the strain data showed clear indications of buckling, but pinpointing the exact moment of buckle initiation proved challenging. Instead of a sudden change in strain, the data showed a gradual strain change over time, making the exact buckling point difficult to determine. For Slab 11, four fibers were placed in the buckling zone, two of them indicated buckling before the peak load was reached. For Slab 10 only Fiber 2 provided usable data, Fiber 2, which is located on the web, indicated buckling after the peak load was reached. For Slab 11, Fiber 2 was the last to show buckling. The absence of data from other fibers in Slab 10 makes it impossible to conclude whether buckling happened earlier in the loading process. Thus, to confirm that buckling is detectable before the peak load is reached, more data is needed.

## 8.4. Concrete crack detection

The crack detection using fibers applied to the steel sheeting faced several limitations. First, it could be unclear whether peaks in the strain data represented actual cracks because they were close to average strain values or because multiple peaks occurred close together. Additionally, debonding between the steel sheeting and concrete could cause multiple cracks to be identified as a single large peak, leading to missed crack detection. Some cracks visible on the sides of the slab were not detected by the fibers, and cracks detected by one fiber were not always detected by other fibers.

Research by Bai et al. [19] on applying fibers to steel mesh within composite slabs highlighted a similar limitation, when cracks were spaced less than 100 mm apart, individual cracks would be difficult to identify. However, they found that fibers embedded within the concrete provided good in-situ crack detection and could detect microcracks before they became visible. This suggests that while fibers applied to steel sheeting have limitations, fibers embedded in the concrete offer superior crack detection capabilities.

# 9. Conclusions and recommendations

This chapter presents the key conclusions of this thesis, addressing the main research question by answering the four sub-questions that guided the study. The main research question is:

*What insights into the structural performance of deep steel-concrete composite slabs can be found by distributed strain measurements on the steel sheeting during loading?*

The first sub-question is:

1. *What is the strain distribution across the embossed regions, how does it differ from flat parts of the steel sheeting, and what causes these differences?*

This research question was examined in Chapter 4 using Distributed Optical Fibers (DOFs) applied to both the embossed areas of the top flange and the indented sections of the web in the steel sheeting. The strain data revealed oscillations in both regions. In the web, these oscillations began forming during the cyclic loading phase, while in the top flange, they emerged later, during the static loading phase close to the plastic loading stage.

Throughout the test, the web remained in tension. However, the strain data indicated that when oscillations appeared, the indented parts of the web were in tension, while the flat sections were in compression. This behaviour can be attributed to the local effects of the geometry of the indentations under tension. The indented part bends downward, creating tension, while the flat part bends upward, causing compression.

When oscillations are present in the strain data of the top flange, it is in compression as opposed to tension in the web. Despite this difference, the strain data shows similar results. The flat part is in compression and the embossed part is in tension. Again, this can be attributed to the localized effects of the geometry of the embossment, now in compression instead of tension. The embossed part bends downward, creating tension, while the flat part bends upward, causing compression.

2. *What is the position of the neutral axis of the slabs at different stages during loading, and how does it compare with theoretical predictions of the neutral axis position?*

In Chapter 5, the neutral axis (N.A.) location was determined using five fibers distributed along the height of the steel sheeting. While the fiber on the web provided usable data, the fibers on the top flange did not. The fibers on the web gave usable strain values by taking the average of the minimum values and adding them to the average of the maximum values. This did not work for the strain data of the fibers applied to the top flange. By fitting a linear curve to the strain distribution, the N.A. location was identified at different load levels. The strain distribution remained linear in the elastic stage, but as the load approached peak levels, it became non-linear, reducing the accuracy of the N.A. estimation through linear fitting. A fiber was also applied to the side of the slab, on the concrete, which serves as an indication of the neutral axis in the concrete.

Three stages were identified; the initial, elastic, and plastic stage. The N.A. position shifts during these stages, according to theoretical calculations the N.A. starts in the steel sheeting at 86 mm from the top of the slab, it then shifts upwards to 49 mm, which is above the steel sheeting, fully in the concrete. The top of the slab is 55 mm above the steel sheeting. Lastly, it shifts upwards again to 33 mm from the top of the slab, in the plastic stage.

The N.A. position results from Slabs 12, 11, and 6 are summarized in Table 9.1. There were notable differences between these slabs. Slabs 11 and 12 spanned 3.6 meters, whereas Slab 6 spanned 5.4 meters. Additionally, Slabs 12 and 6 had a reinforcement rebar in their ribs, while Slab 11 did not.

*Table 9.1. Summary of the N.A. positions.*

| | *Slab* | *N.A. position found by the fibers (in mm from the top of the slab)* | *N.A. position* |
|---|---|---|---|
| *Initial stage* | 12 | 75.8 | In the steel sheeting |
| | 11 | 90.6 | In the steel sheeting |
| *Elastic stage* | 12 | 40 | In the concrete |
| | 11 | 59 | In the steel sheeting |
| | 6 | 32 | In the concrete |
| *Plastic stage* | 12 | 62 | In the steel sheeting |
| | 11 | 84 | In the steel sheeting |
| | 6 | 57 | In the steel sheeting |

The neutral axis position determined by the fibers applied to the steel sheeting of the middle rib followed the expected trend during the initial and elastic loading stages across all three slabs. The N.A. starts in the steel sheeting and as the load increases the N.A. shifts upwards above the steel sheeting into the concrete. Although the general trend was consistent, the value of the actual N.A. position deviates from the theoretical value. Particularly in Slab 11, there is a large difference between the theoretical N.A. position and the result from the fibers. In the elastic stage, the N.A. was positioned deeper within the slab at 59 mm from the top of the slab, while the theoretical value was 45.2 mm. This difference is due to a loss of shear interaction occurring during the cyclic loading part. Slab 11 had no reinforcement rebar in its ribs while Slabs 6 and 12 did, this is likely the cause of the difference between the slabs.

During the initial and elastic stage, the Concrete Fiber readings closely aligned with those obtained from the middle rib. This indicates that in these stages, the N.A. position of the steel sheeting and the concrete is identical and therefore there is full composite interaction between the steel sheeting and concrete.

However, in the plastic loading stage, the N.A. position derived from the middle rib fibers deviated from the theoretical position and the Concrete Fibers N.A. position. Instead of shifting upwards, as predicted by the FE model, the N.A. moved downwards into the steel sheeting. In contrast, the concrete fiber readings continued to follow the expected trend. This suggests a loss of shear interaction between the steel sheeting and the concrete, leading to partial composite interaction. The loss of shear interaction is confirmed by the slip between the steel sheeting and concrete. The downward shift of the N.A. coincided with an increase in slip for all three slabs. As a result, the N.A. positions of the steel sheeting and the concrete should be considered separately in the plastic stage. Therefore, in this phase, fibers attached to the steel sheeting alone cannot accurately determine the N.A. position of the slab, instead they give the N.A. position of the steel sheeting alone.

3. *At what point during loading is buckling of the steel sheeting detected?*

This research question is addressed in Chapter 6. Two slabs that experienced buckling of the steel sheeting had fibers applied in the buckling zone. In Slab 11, Fibers 2, 3, 4, and 5 were located within the buckling zone, while in Slab 10, only Fiber 2 was in the buckling zone. All fibers displayed deformation patterns which indicated buckling during testing. These observations lead to the conclusion that distributed optical fibers are effective in detecting buckling when applied to steel sheeting. For Slab 11 the buckling was detected before the peak load was reached by two fibers located on the top flange. Fiber 4 gave the earliest indication of buckling at a load of 211 kN, which is 97% of the peak load, Fiber 5 detected buckling at 98.3% of the peak load. This suggests that the buckling likely began in proximity to Fiber 4. However, this pattern may vary for other slabs, as the location of buckling initiation could differ depending on factors such as local material properties or imperfections.

For Slab 10, buckling was detected after the peak load, but only one fiber was positioned in the buckling zone. This fiber, located on the web, was consistent with the behaviour observed in Slab 11. If the other locations were available then it could be the case that the buckling was detected earlier since this was also the case for Slab 11.

The fibers provide real-time data that can pinpoint the onset of structural instability, offering valuable insight into the behaviour of the slab under load. This demonstrates their potential as a reliable monitoring tool for early detection of buckling, which can enhance safety and structural performance.

4. *What are the locations of the concrete cracks, and how do they propagate through the slab?*

The last research question was examined in Chapter 7. For crack detection, fibers were applied to the bottom of each rib, where crack openings are the largest. The resulting tension peaks in the strain data were used to identify potential crack locations. However, the crack locations detected by the fibers did not always correlate with visually identified cracks on the slab sides, and there were inconsistencies between cracks found in different ribs.

This suggests that crack detection using DOFs on the steel sheeting has limitations in accuracy and consistency. Several factors contribute to this, firstly, it is uncertain which peaks represent a crack, peaks can be relatively small or close to each other, making it difficult to identify cracks. Furthermore, not all cracks that were visible on the side of the slab were detected by the fibers, this is especially the case for the shear spans. Additionally, there can be debonding of the steel sheeting and concrete which causes a larger part of the steel sheeting to deform than only at the crack opening, which can cause two or more cracks to be detected as one.

## 9.1. Recommendations for future research

From this thesis the following recommendations can be made:

- A more precise study can be done on the embossment region behaviour where the exact positions of the embossed, slanted, and flat parts of the steel sheeting are identified before testing. In this research, the data had to be compared with a strain gauge which was applied in the middle of the span. In future research, this can be done for several embossments spread over the span of the slab.
- This thesis concluded that the oscillations in the embossed regions of the steel sheeting are caused by deformations due to the tensioning of the web and compression of the top flange. This theory can be verified by tensioning a cut-out of the web and compressing a cut-out of the top flange. DOFs can be used to measure the strain across the embossments.
- Fiber 2 was applied on the embossment in the middle of the web in all slabs. In future research, the fiber could also be placed close to the top or bottom of the web, while still on the

embossment. These other locations could yield different results than the fiber in the middle. They could also give more data points to determine the N.A. position.

- The N.A. position can be determined with fibers applied on the steel sheeting. However, the research showed that if there is partial shear interaction the N.A. is determined only for the steel sheeting and the entire slab. The data from the middle rib was compared with the data from the concrete fiber that was placed on the side of the slab. An improvement for future research would be to determine the N.A. position in the concrete of the middle rib.
- The concrete crack detection of the fibers is limited if they are applied to the steel sheeting. Instead, a better application would be on a steel mesh inside the concrete or on the reinforcement rebar in the rib.

# Bibliography

[1] J. W. Rackham, G. H. Couchman, S. J. Hicks and L. A. Dougherty, *Composite slabs and beams using steel decking,* SCI, 2023.

[2] Steel for Life; British Constructional Steelwork Association; SCI, “Steelconstruction.info,” [Online]. Available: https://www.steelconstruction.info/Composite_construction#Resources. [Accessed 2024].

[3] C. Bailey, “Efficient arrangement of reinforcement for membrane behaviour of composite floor slabs in fire conditions,” 2003.

[4] European Committee For Standardization, “Eurocode 4: Design of composite steel and concrete structures - Part 1-1: General rules and rules for buildings.,” 2005.

[5] M. F. Bado, J. R. Casas, A. Dey, C. G. Berrocal, G. Kaklauskas, I. Fernandez and R. Rempling, “Characterization of concrete shrinkage induced strains in internally-restrained RC structures by distributed optical fiber sensing,” *Cement and Concrete Composites,* vol. 120, no. 104058, 2021.

[6] W. I. Simms and A. F. Hughes, *Composite design of steel framed buildings,* SCI, 2011.

[7] J. Newman and P. Owens, “Properties of lightweight concrete,” in *Advanced Concrete Technology*, p. 2/16.

[8] Dutch Engineering, “Staal-beton Vloersystemen,” 2013. [Online]. Available: https://www.dutchengineering.nl/media/vk_1198/files/Staalplaat-betonvloersystemen.pdf.

[9] R. G. Schuurman, “Physical behaviour of shear connections in steel-concrete composite slabs. Numerical simulation of free-surface flows with steep gradients,” 2001.

[10] F. Kavoura, “Lecture CS5 - Composite Slabs,” in *Steel Structures 3 (CIE 4121)*, 2022.

[11] P. van Erp, “Horizontal Shear Resistance on ComFlor 210 (Master Thesis, TU Delft),” 18 January 2017. [Online]. Available: https://repository.tudelft.nl/islandora/object/uuid%3A613a4ebf-7d48-48f6-9c07-4a84fca028bc?collection=education. [Accessed June 2024].

[12] D. Papastergiou and J.-P. Lebet, “Design and experimental verification of an innovative steel–concrete composite beam,” *Journal of Constructional Steel Research,* vol. Volume 93, pp. 9-19, 2014.

[13] A. Barrias, J. R. Casas and S. Villalba, “A Review of Distributed Optical Fiber Sensors for Civil Engineering Applications,” *Sensors,* vol. 16, no. 5, 2016.

[14] H. Guo, G. Xiao, N. Mrad and J. Yao, “Fiber Optic Sensors for Structural Health Monitoring of Air Platforms,” *Sensors,* vol. 11, no. 4, pp. 3687-3705, 2011.

[15] G. Kaklauskas, A. Sokolov, R. Ramanauskas and R. Jakubovskis, “Reinforcement Strains in Reinforced Concrete Tensile Members Recorded by Strain Gauges and FBG Sensors: Experimental and Numerical Analysis.,” *Sensors,* vol. 19, no. 1, 2019.

[16] FBGS, “FBG Principle,” [Online]. Available: https://fbgs.com/technology/fbg-principle/. [Accessed 04 2024].

[17] M. Weisbrich and K. Holschemacher, “Comparison between different fiber coatings and adhesives on steel surfaces for distributed optical strain measurements based on Rayleigh backscattering,” *Journal of Sensors and Sensor Systems,* vol. 7, no. 2, pp. 601-608, 2018.

[18] X. Tan, P. Guo, X. Zou and Y. Bao, “Buckling detection and shape reconstruction using strain distributions measured from a distributed fiber optic sensor,” *Measurement,* vol. Volume 200, no. 111625, 2022.

[19] H. Bai, D. Guo, W. Wang, X. Tan, M. Yan, G. Chen and Y. Bao, “Experimental investigation on flexural behavior of steel-concrete composite floor slabs with distributed fiber optic sensors,” *Journal of Building Engineering,* vol. 54, no. 104668, 2022.

[20] Y. Zhang, F. Kavoura and M. Veljkovic, “Experimental report: Four-point bending tests on composite slabs with deep-profiled steel sheeting,” Delft University of Technology, 2024.

[21] Eurocode Applied, “Eurocode 2, Table of concrete design properties,” [Online]. Available: https://eurocodeapplied.com/design/en1992/concrete-design-properties.

[22] Y. Zhang, F. Kavoura, L. Gouw and M. Veljkovic, “Experimental and numerical study for neutral axis location of the deep-profiled steel-concrete composite slab,” *13th International Conference on Advances in Steel-Concrete Composite structures,* 2024.

[23] W. Kenton, “Least Squares Method: What It Means, How to Use It, With Examples,” 24 September 2023. [Online]. Available: https://www.investopedia.com/terms/l/least-squares-method.asp#:~:text=The%20least%20squares%20method%20is%20a%20statistical%20procedure%20to%20find,the%20behavior%20of%20dependent%20variables.. [Accessed 8 2024].

[24] Tata Steel UK Limited, “ComFlor® manual, Composite floor decking design and technical information,” 2017. [Online]. Available: https://www.tatasteeleurope.com/sites/default/files/ComFlor%20manual.pdf.

[25] S.-i. Nakamura, T. Hosaka and K. Nishiumi, “Bending Behavior of Steel Pipe Girders Filled with Ultralight Mortar,” *Journal of Bridge Engineering,* vol. Volume 9, no. 3, pp. 291-303, 2004.

# A. Appendix: Details of the steel sheeting

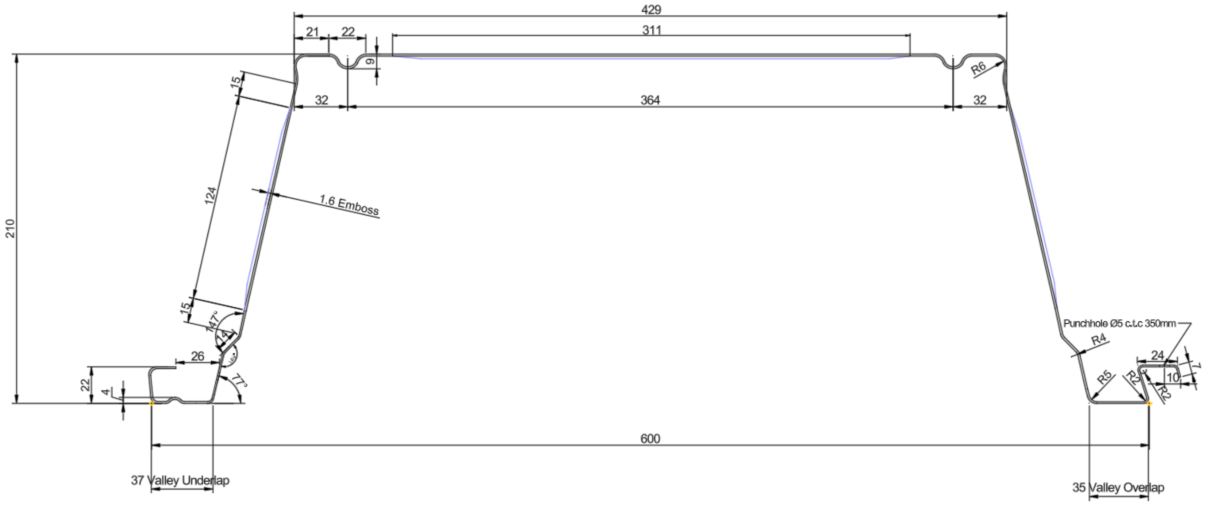

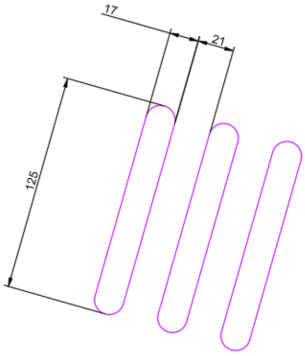

SIDE EMBOSSMENTS

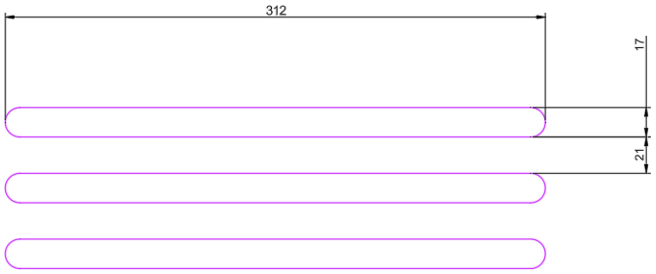

TOP EMBOSSMENTS

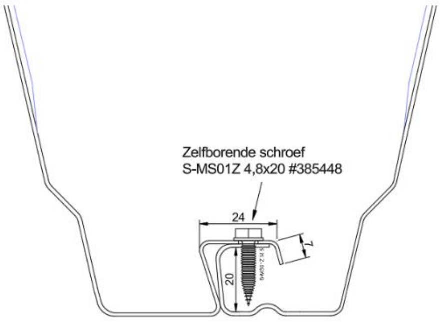

Detail overlap

# B. Appendix: Embossment region behaviour

## B.1. Behaviour of the web

This section shows additional data and information the data which was referenced in section 4.1.1.

**Slab 6**

Slab 6 spans 5.4 meters and has a reinforcement rebar in its ribs.

The strain levels are plotted over time for both the strain gauge and a specific measurement point of the optical fiber. When these strain levels overlap, the optical fiber measurement point indicates the position of the strain gauge compared to the fiber data, this is illustrated in Figure B.1.

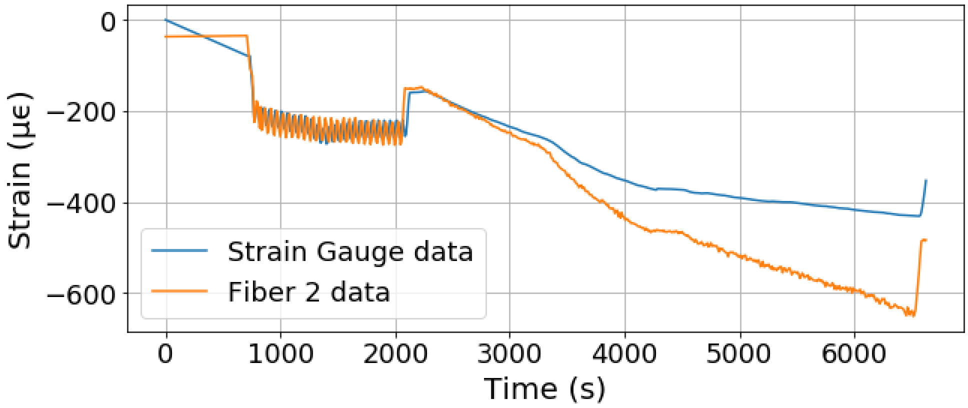

*Figure B.1. The strain levels over time, of the strain gauge and the corresponding measurement point of Fiber 2, from slab 6.*

Figure B.2 shows the strain of Fiber 2 over a small part of the span, the measurement point corresponding to the strain gauge is highlighted with an orange dot. Additionally, it shows in the photo that the strain gauge is applied on the left side of the flat part.

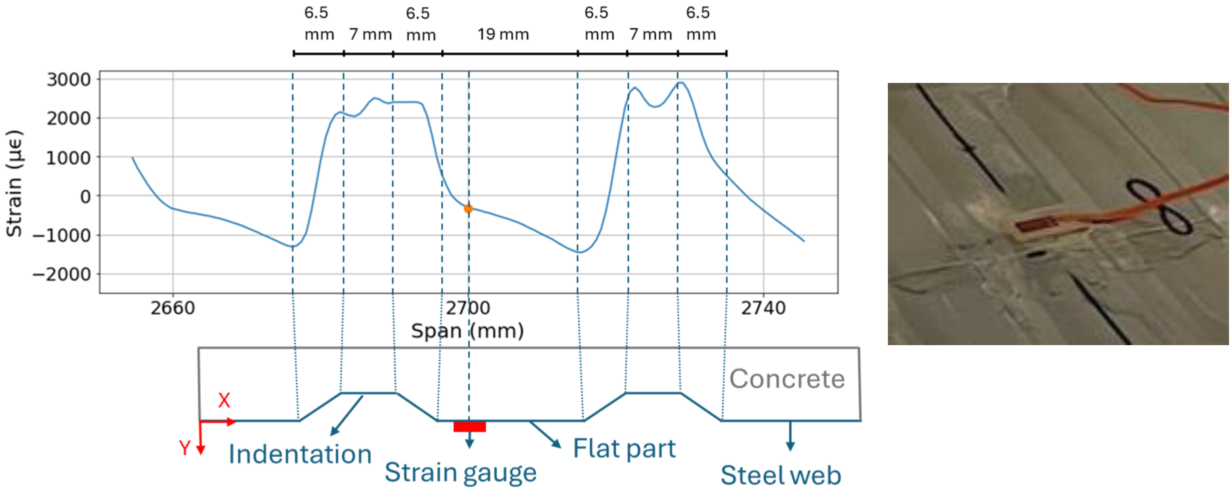

*Figure B.2. Strain of Fiber 2, slab 6, overlapping with a small part of the steel web (left), and a photo of the strain gauge location on the flat part of the web (right).*

**Slab 10**

Slab 10 is 3.6 meters long and has a reinforcement rebar in its ribs. For Slab 10 the overlapping strain measurements of the strain gage and Fiber 2 are shown in Figure B.3.

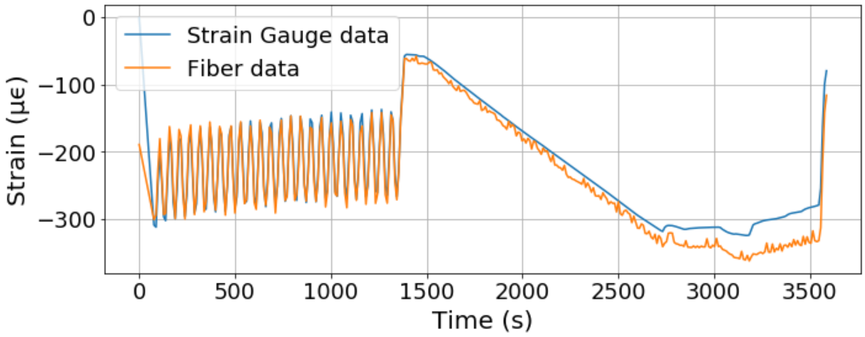

*Figure B.3. The strain levels over time, of the strain gauge and the corresponding measurement point of Fiber 2, from slab 10.*

Figure B.4 shows the strain of Fiber 2 over a small part of the span, the measurement point corresponding to the strain gauge is highlighted with an orange dot. Additionally, it shows in the photo that the strain gauge is applied in the middle of the flat part of the web.

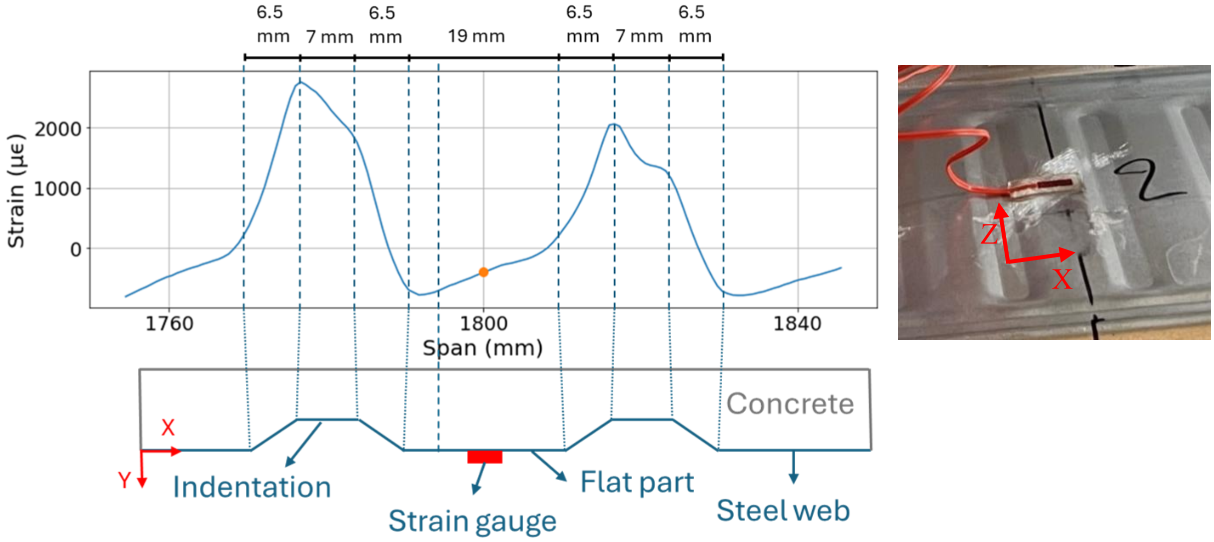

*Figure B.4. The strain of Fiber 2, Slab 10, overlapping with a small part of the steel web (left), and a photo of the strain gauge location on the flat part of the web (right).*

**Slab 12**

Slab 12 is 3.6 meters long and has a reinforcement rebar in the ribs. For Slab 12 the overlapping strain measurements of the strain gage and Fiber 2 are shown in Figure B.5.

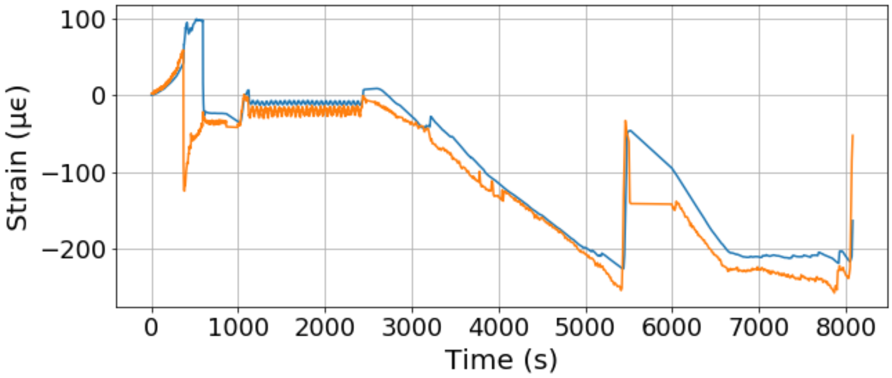

*Figure B.5. The strain levels over time, of the strain gauge and the corresponding measurement point of Fiber 2, from slab 12.*

Figure B.6 shows the strain of Fiber 2 over a small part of the span, and the measurement point corresponding to the strain gauge is highlighted with an orange dot. Additionally, it shows in the photo that the strain gauge is applied on the right side of the flat part of the web, this means that in the fiber data, the strain gauge is also on the right side of the flat part, which is opposite to Slabs 6 and 10.

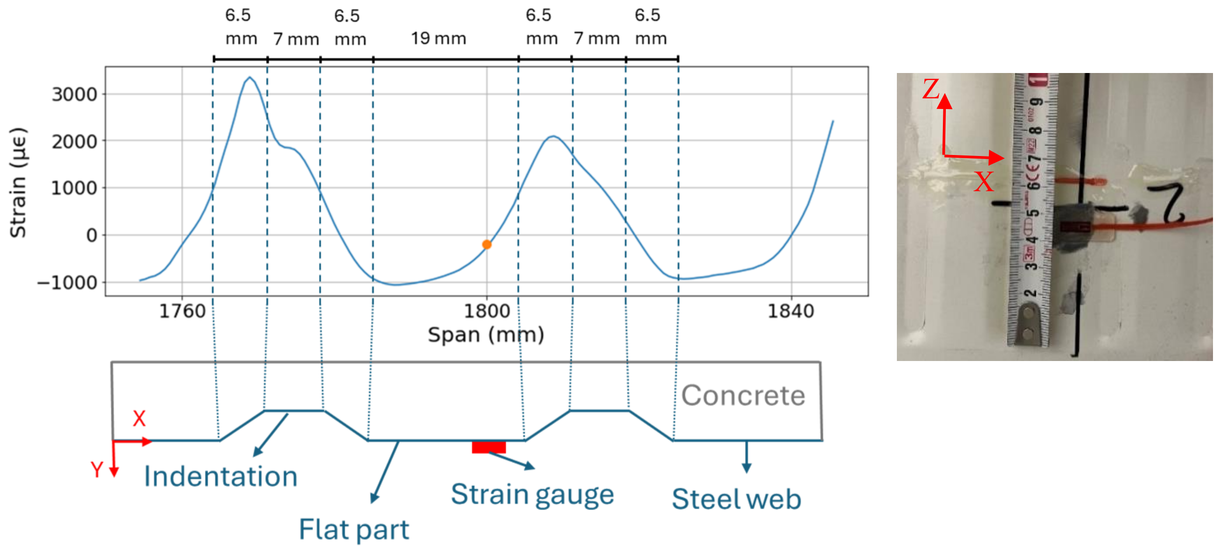

*Figure B.6. The strain of Fiber 2, Slab 12, overlapping with a small part of the steel web (left), and a photo of the strain gauge location on the flat part of the web (right).*

## B.2. Behaviour of the top flange

This section shows additional data and information the data which was referenced in section 4.1.2.

**Slab 6**

The measurement point of the fiber data corresponding to the strain gauge is identified similarly to the process used for Fiber 2. The overlapping strain measurements for strain gauge 4 and Fiber 4 are illustrated on the left side of Figure B.7, while strain gauge 5 and Fiber 5 are depicted on the right side of Figure B.7.

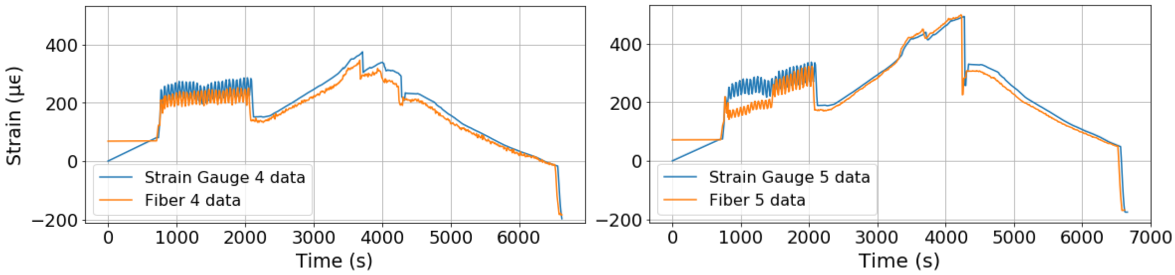

*Figure B.7. The strain levels over time, of the strain gauge and the corresponding measurement point of Fiber 4 (left), and Fiber 5 (right), from Slab 6.*

Figure B.8 shows the strain of Fiber 4 over a small portion of the span, and the measurement point corresponding to the strain gauge is highlighted with an orange dot. Additionally, it shows in the photo that the strain gauge is applied slightly to the right side of the flat part of the web, this means that in the fiber data, the strain gauge is also on the right side of the flat part. The same has been done for Fiber 5 which is illustrated in Figure B.9, here the strain gauge was also moved slightly to the right side of the flat part.

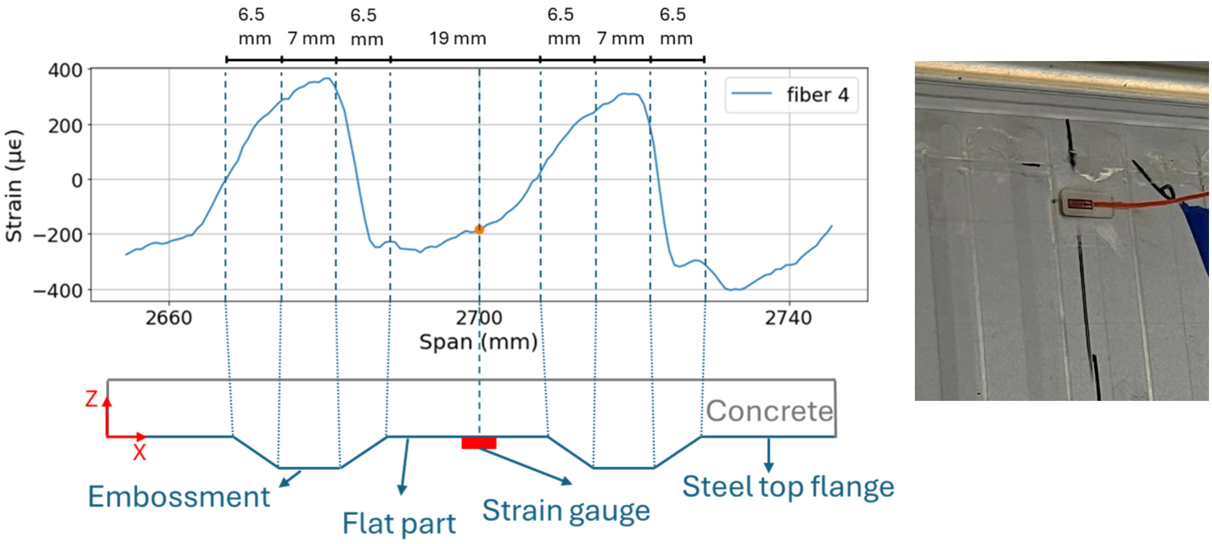

*Figure B.8. The strain of Fiber 4, Slab 6, overlapping with a small part of the steel top flange (left), and a photo of the strain gauge location on the flat part of the flange (right).*

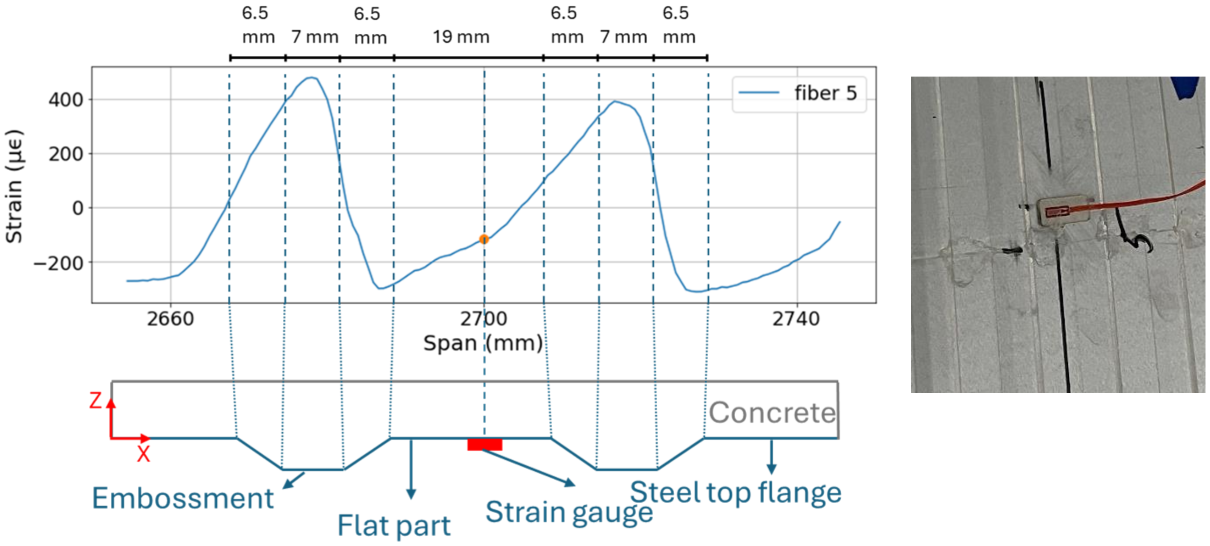

*Figure B.9. The strain of Fiber 5, Slab 6, overlapping with a small part of the steel top flange (left), and a photo of the strain gauge location on the flat part of the flange (right).*

### Slab 12

For Slab 12 the figures of the overlapping strain measurements of the strain gauges and Fibers 4 and 5 are shown in Figure B.10

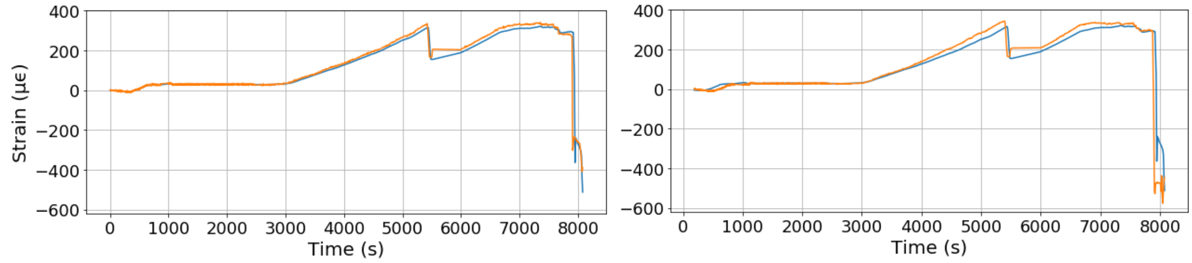

*Figure B.10. The strain levels over time, of the strain gauge and the corresponding measurement point of Fiber 4 (left), and Fiber 5 (right), from Slab 12.*

Figure B.11 illustrates the strain of Fiber 2 over a small portion of the span, and the measurement point corresponding to the strain gauge is highlighted with an orange dot. Additionally, it shows in the photo that the strain gauge is applied to the left side of the flat section of the web, this means that in the fiber data, the strain gauge is also on the left side of the flat section. The same has been done for Fiber 5 which is illustrated in Figure B.12.

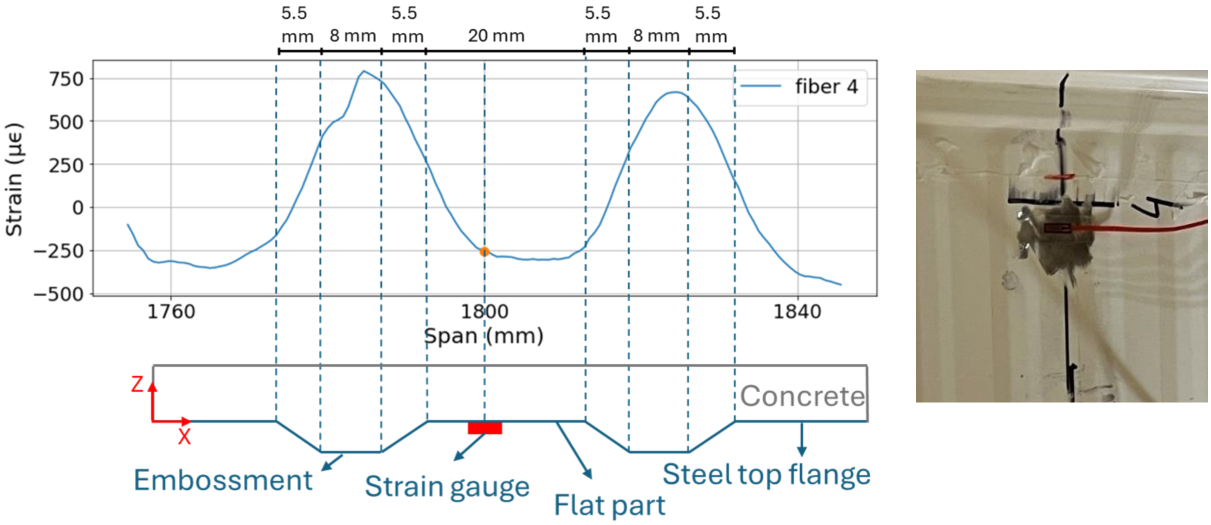

*Figure B.11. The strain of Fiber 4, Slab 12, overlapping with a small part of the steel top flange (left), and a photo of the strain gauge location on the flat part of the flange (right).*

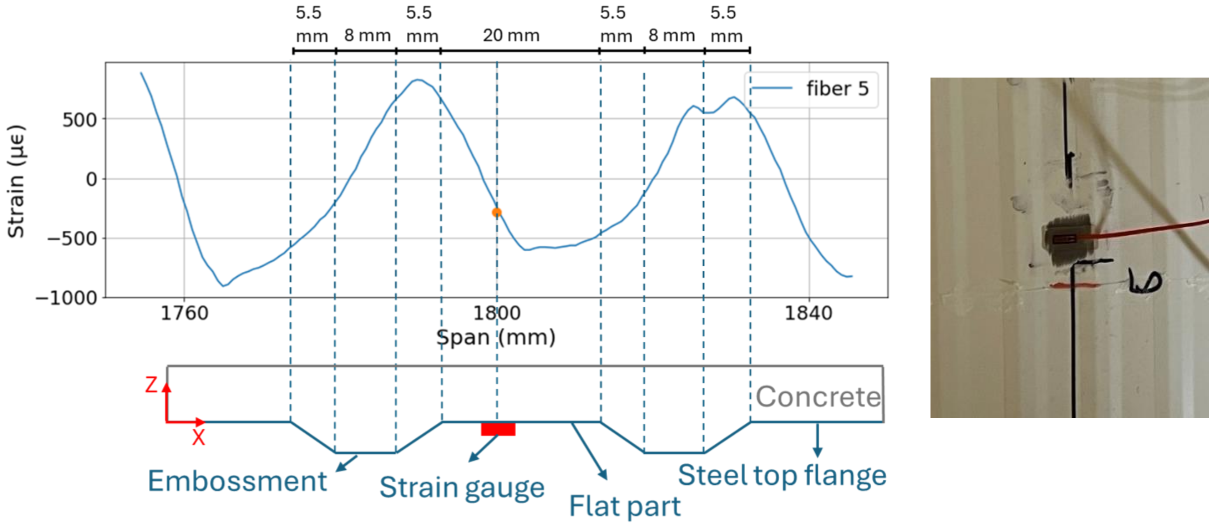

*Figure B.12. The strain of Fiber 5, slab 12, overlapping with a small part of the steel top flange (left), and a photo of the strain gauge location on the flat part of the flange (right).*

The results of Fiber 4, shown in Figure B.11, is very similar to the results of Slabs 6 and 11; the positive tension peak is located at the embossment region of the flange, and the flat region is in compression. However, for fiber 5 the peak shifted to the right, and the tension peak is located at the slanted part, instead of at the embossment section. This could be due to the oscillation forming very late in the test at mid-span. Figure B.13 illustrates the strain of Fiber 5 close to failure, it can be seen that the oscillations have just started to form at mid-span. The load level has been indicated in the load-displacement graph.

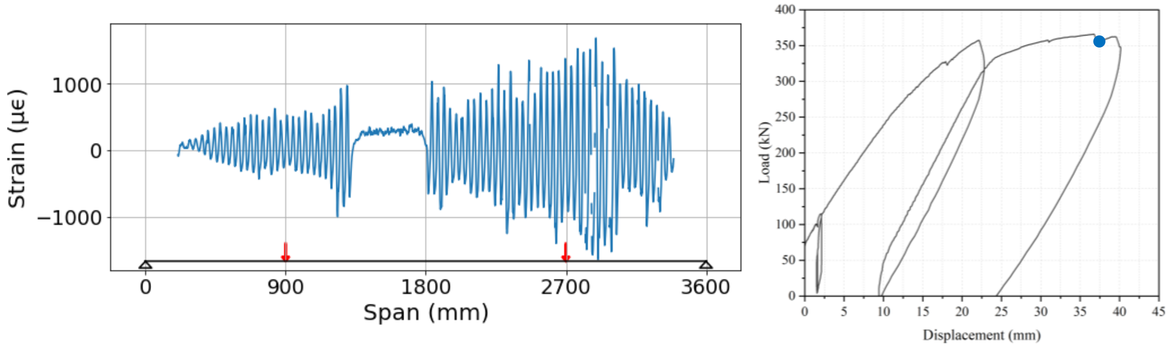

*Figure B.13. Strain of Fiber 5 close to failure (left), and the load-displacement graph of slab 12 (right).*

# C. Appendix: Neutral axis location

## C.1. Theoretical calculation of neutral axis location

This section shows additional data and information the data which was referenced in section 5.1.

**Initial loading stage**

In the initial and elastic stages, the neutral axis (N.A.) is located at the centroidal axis of the cross-section. For the calculations, the steel sheeting was divided into 9 different areas ($A_{S1}$ to $A_{S9}$). For these individual areas, the location of the centroidal axis was found and the distance of the centroidal axis to the top of the slab is denoted by $e_{S1}$ to $e_{S9}$. The steel sheeting areas 1 to 9 are highlighted on the left side of Figure C.1. The concrete areas of the initial phase are split in two and highlighted on the right side of Figure C.1.

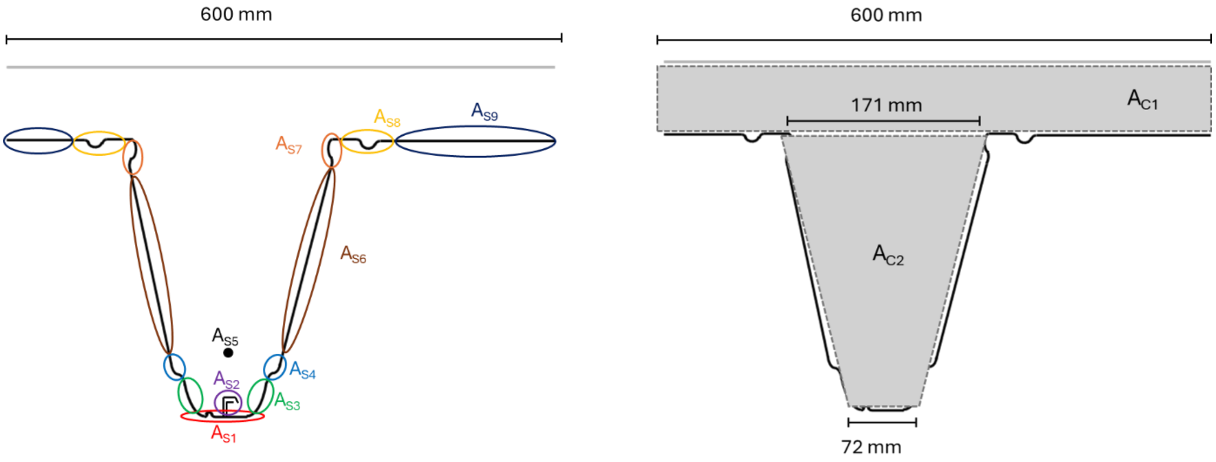

*Figure C.1. Cross-section of one rib, highlighting the steel areas (left), and the concrete areas (right).*

The areas and the distances from their centroid to the top of the slab are listed in Table C.1. The areas of the concrete have been reduced with the modular ratio (n) to account for the lower elasticity of the concrete. With:

$$n = \frac{E_{concrete}}{E_{steel}} = \frac{30}{200} = 0.15$$

*Table C.1. Areas of the cross-section and the distances between their centroids and the top of the slab.*

| | *Area (mm²)* | | *Distance (mm)* |
|---|---|---|---|
| $A_{S1}$ | 72 | $e_{S1}$ | 265 |
| $A_{S2}$ | 70 | $e_{S2}$ | 248.5 |
| $A_{S3}$ | 58 | $e_{S3}$ | 224 |
| $A_{S4}$ | 90 | $e_{S4}$ | 250 |
| $A_{S5}$ | 113.1 | $e_{S5}$ | 218 |
| $A_{S6}$ | 248 | $e_{S6}$ | 152 |
| $A_{S7}$ | 60 | $e_{S7}$ | 69 |
| $A_{S8}$ | 92 | $e_{S8}$ | 56 |
| $A_{S9}$ | 311 | $e_{S9}$ | 56 |

| | | | |
|---|---|---|---|
| $A_{C1}$ | 4950 | $e_{C1}$ | 27.5 |
| $A_{C2}$ | 3827.3 | $e_{C2}$ | 145.7 |

Then the distance from the top of the slab to the centroid of the entire cross-section can be found with the following formula:

$$e_{ini} = \frac{\sum(A_i * e_i)}{\sum A_i} = 86.4\,mm$$

For Slabs 12 and 6 the N.A. is located 86.4 mm from the top, for Slab 11 this is 85.0 mm since it did not have reinforcement rebars in its ribs.

**Elastic loading stage**

In this stage, the concrete only contributes to the compression zone. Assuming the N.A. is fully in the concrete $A_{C2}$ becomes zero, $A_{C1}$ and $e_{C1}$ become:

$A_{C1} = n * 600 * e_{el}$ and $e_{C1} = e_{el}/2$

This is illustrated in Figure C.2.

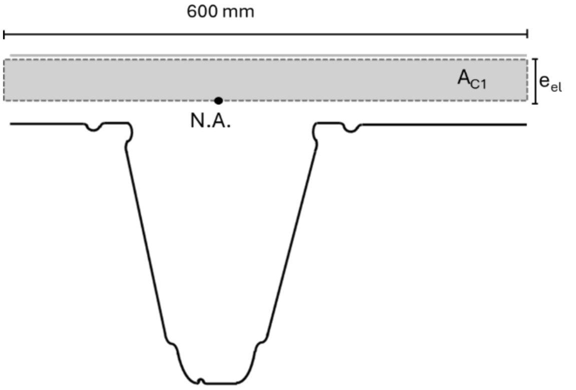

*Figure C.2. Cross-section of a rib indicating the concrete area C1.*

The other areas remain the same. However, the position of the centroid $e_{el}$ is now also in the equations of $A_{C1}$ and $e_{C1}$, the following equation must therefore be solved:

$$e_{el} = \frac{\sum(A_i * e_i)}{\sum A_i} = 48.7\,mm$$

The position of the neutral axis for Slabs 12 and 6 is 48.7 mm, and the position of Slab 11 is 45.2 since it does not have a reinforcement rebar in its ribs.

## C.2. Strain distributions for Slabs 6 and 11

This section shows additional data and information the data which was referenced in section 5.3.

**Slab 6**

Slab 6 spans 5.4 meters and has reinforcement rebars in its ribs. The strain distribution of five load levels in the static loading part is shown in Figure C.3 for the left middle side, and in Figure C.4 for the right middle side. The load levels are highlighted in the load-displacement curve in Figure C.5.

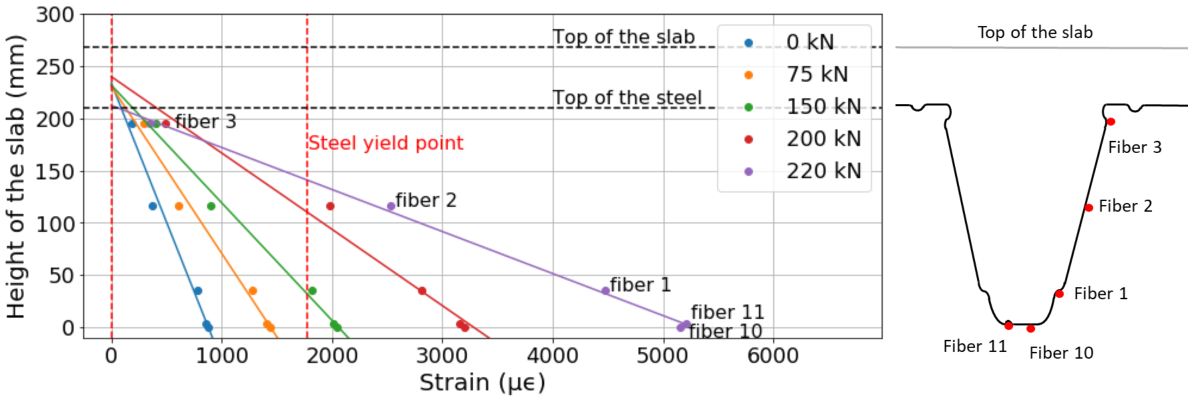

*Figure C.3. Strain distribution of the left middle side of Slab 6, with a fitted line through the measurements.*

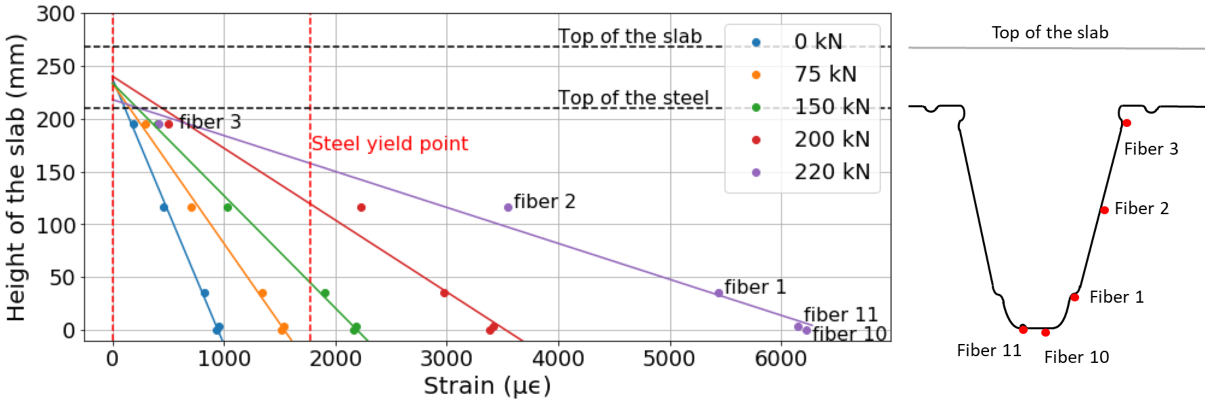

*Figure C.4. Strain distribution of the right middle side of Slab 6, with a fitted line through the measurements.*

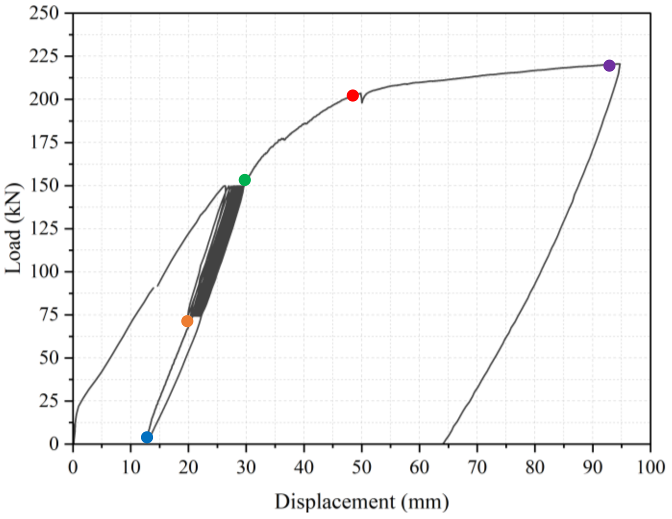

*Figure C.5. The load-displacement curve of Slab 6.*

### Slab 11

Slab 11 spans 3.6 meters and has no reinforcement rebars in its ribs. The strain distribution of five load levels in the static loading part is shown in Figure C.6 for the left middle side, and in Figure C.7 for the right middle side. The load levels are highlighted in the load-displacement curve in Figure C.8.

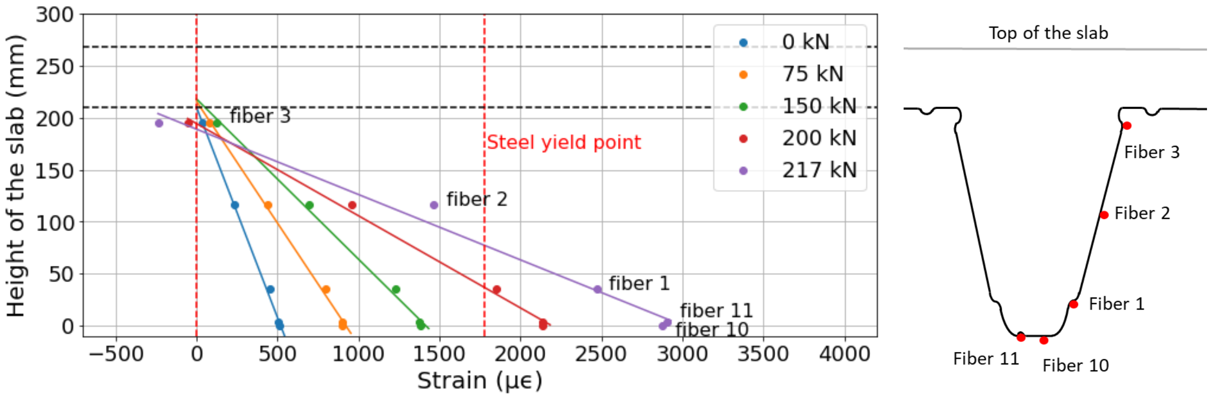

*Figure C.6. Strain distribution of the left middle side of Slab 11, with a fitted line through the measurements.*

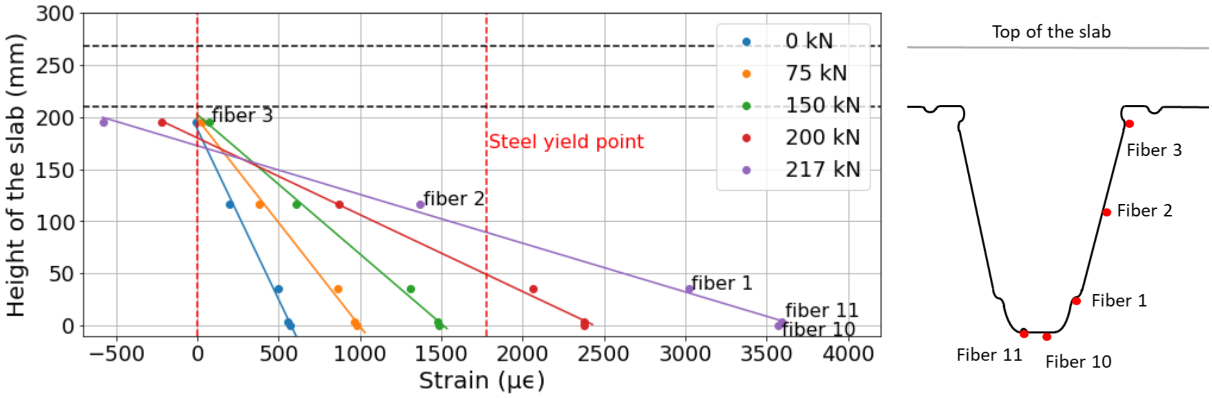

*Figure C.7. Strain distribution of the right middle side of Slab 11, with a fitted line through the measurements.*

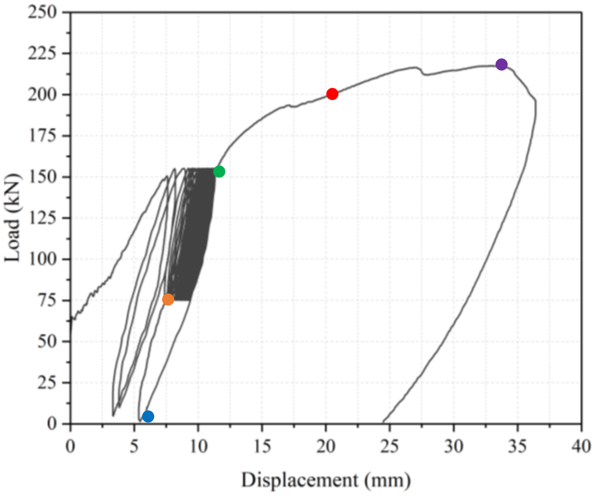

*Figure C.8. The load-displacement curve of Slab 11.*

## C.3. Oscillations in the top flange

This section shows Figures of the oscillations in the strain data of the top flange. This data is referenced in section 5.4.2: Elastic and plastic loading stage results.

**Slab 12**

The strain data of Fiber 4 that shows oscillations forming at the left side of Slab 12 is illustrated in Figure C.9. The load levels that are used are highlighted in the load-displacement curve in Figure C.10.

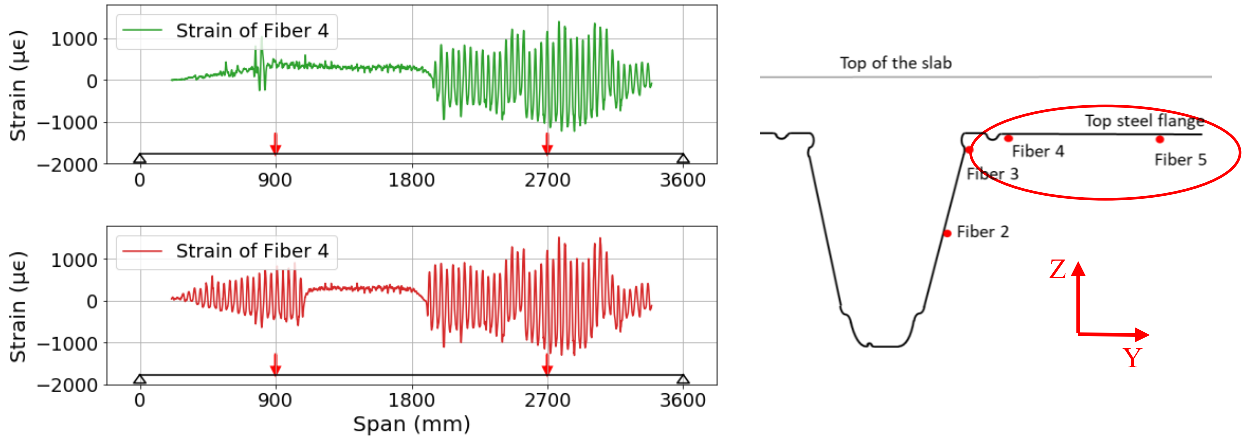

*Figure C.9. The strain data of Fiber 4 at two load levels of Slab 12 (left), and the cross-section of Slab 12 (right).*

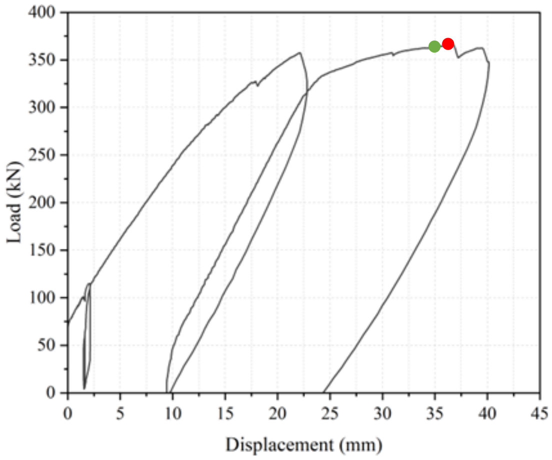

*Figure C.10. Load-displacement curve of Slab 12.*

The same has been done for Fiber 5, its strain data is shown in Figure C.11 at four load levels, the blue and orange graphs show the formation of oscillations on the right side and the green and red graphs show the formation of oscillations on the right side. The load levels are indicated in the load-displacement curve on the right of Figure C.11.

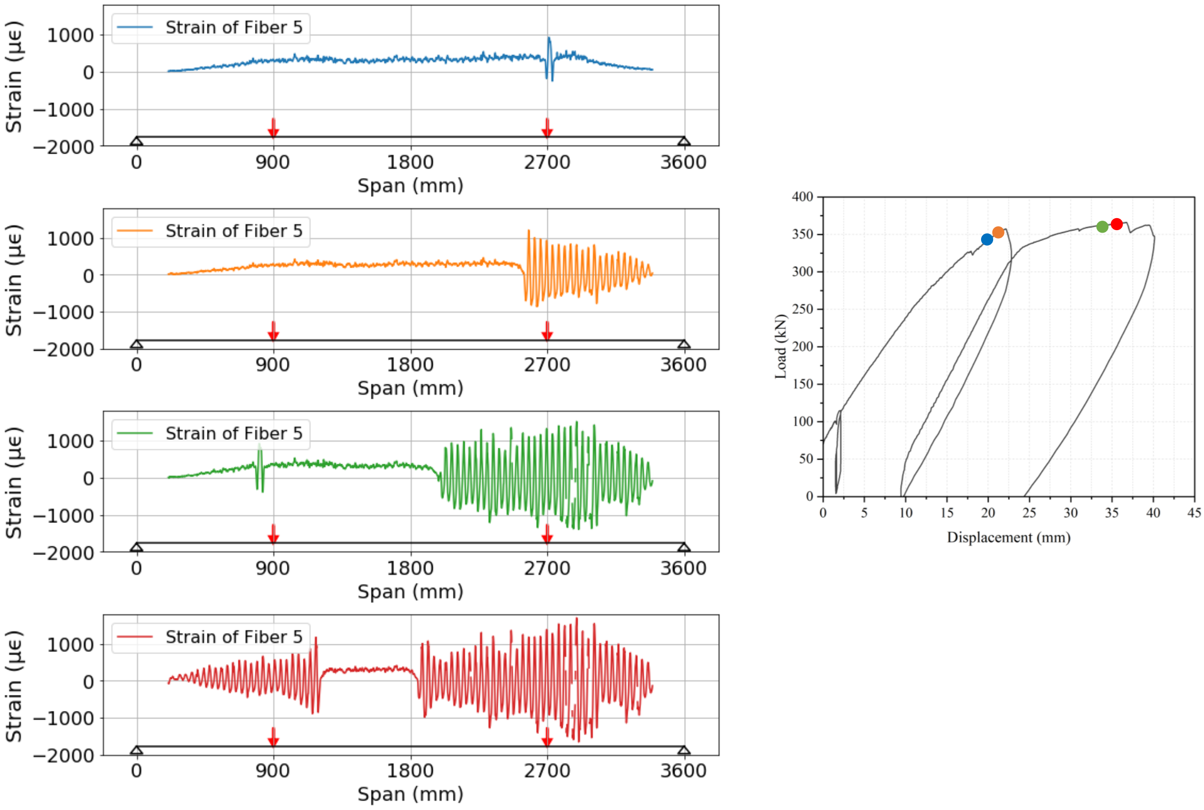

*Figure C.11. The strain data of Fiber 5 at four load levels of Slab 12 (left), and the load-displacement curve of Slab 12 (right).*

### Slab 11

The strain data of Fiber 4 that shows oscillations forming at the left and right sides of Slab 11 is illustrated in Figure C.12. The load levels used are highlighted in the load-displacement curve on the right. The blue graph shows the strain of Fiber 4 before the cyclic loading part and the orange graph shows it after the cyclic loading part. The green graph shows that the oscillations do not spread until the point of the red graph which is at 165 kN, which is approximately 75% of the peak load. The strain values of Fiber 5 at the same load levels are shown in Figure C.13.

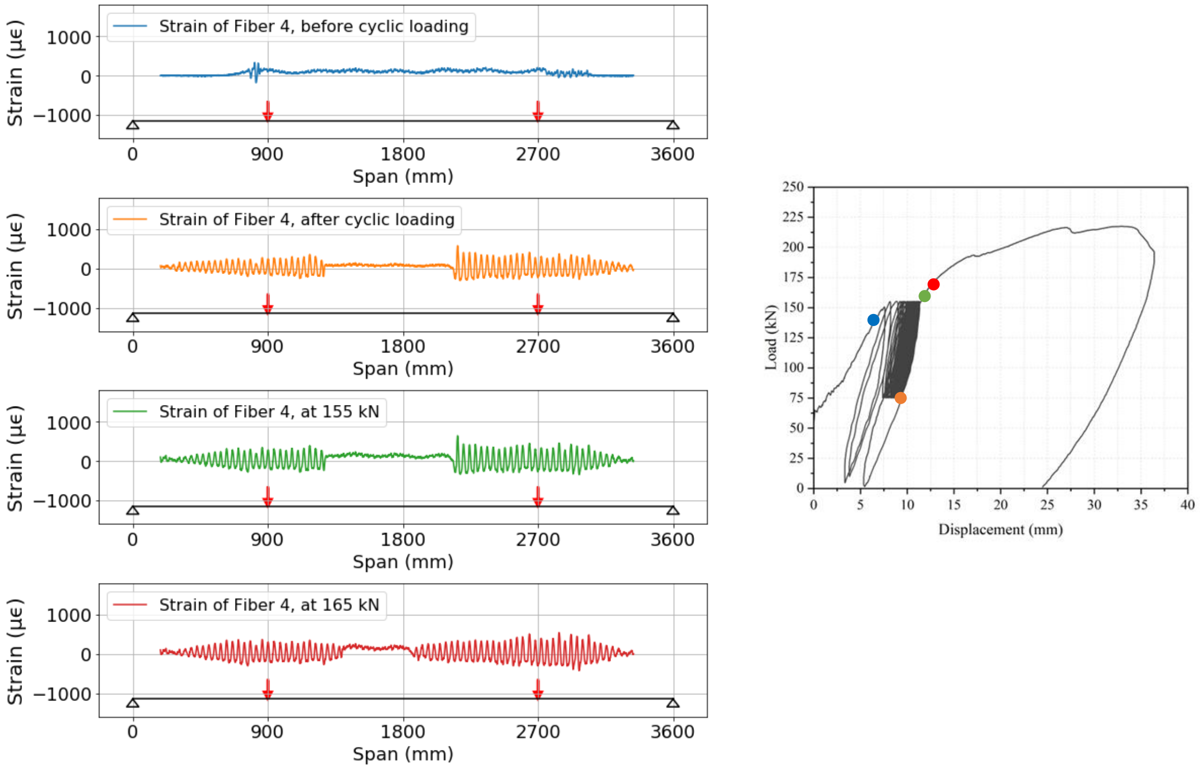

*Figure C.12. The strain data of Fiber 4 at four load levels of Slab 11 (left), and the load-displacement curve of Slab 11 (right).*

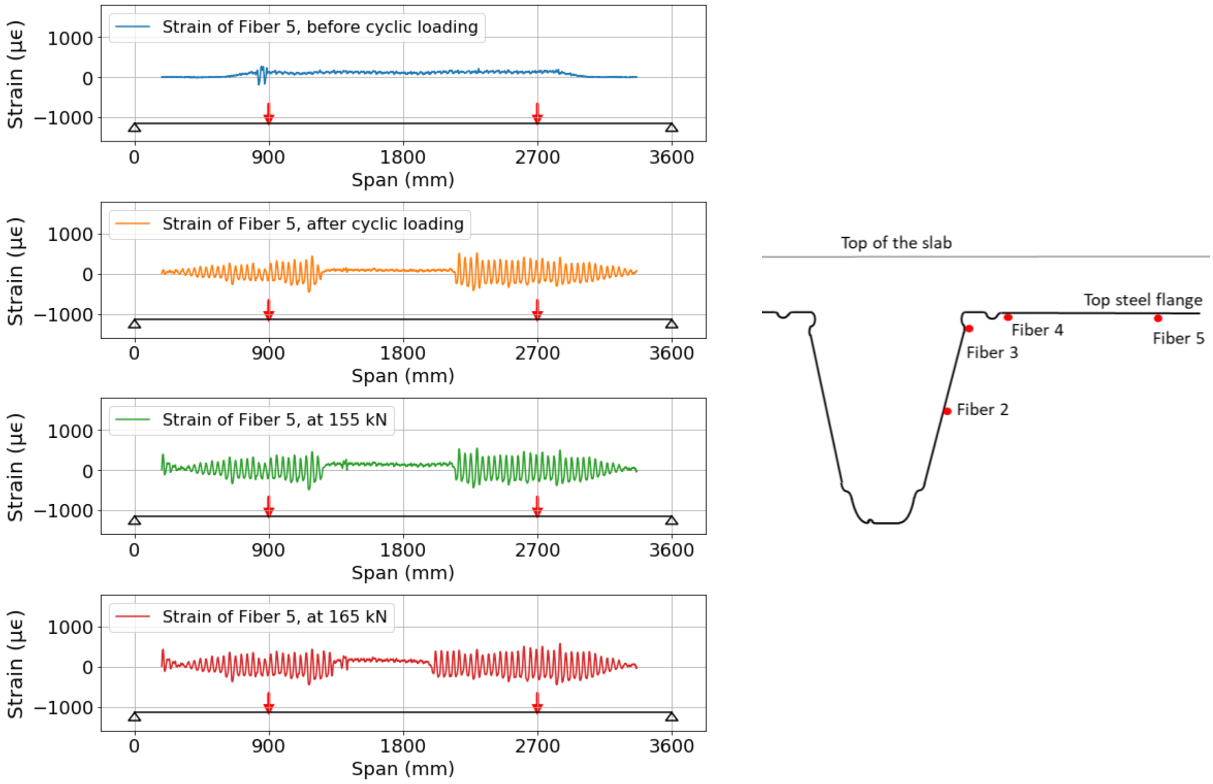

*Figure C.13. The strain data of Fiber 5 at four load levels of Slab 11.*

**Slab 6**

The strain data of Fiber 4 that shows oscillations forming at the left and right sides of Slab 6 is illustrated in Figure C.12. The load levels that are used are highlighted in the load-displacement curve on the right. The blue graph shows the strain of Fiber 4 at 175 kN which is approximately 80% of the peak load. There are some oscillations present at this load, as opposed to the other slabs. This difference is likely due to Slab 6 spanning 5.4 meters and Slabs 11 and 12 spanning 3.6 meters. The green graph shows that the oscillations change and become more uniform and increase in magnitude at both load points, this is at a load level of 185 kN which is 85% of the peak load. The strain values of Fiber 5 at the same load levels are shown in Figure C.15.

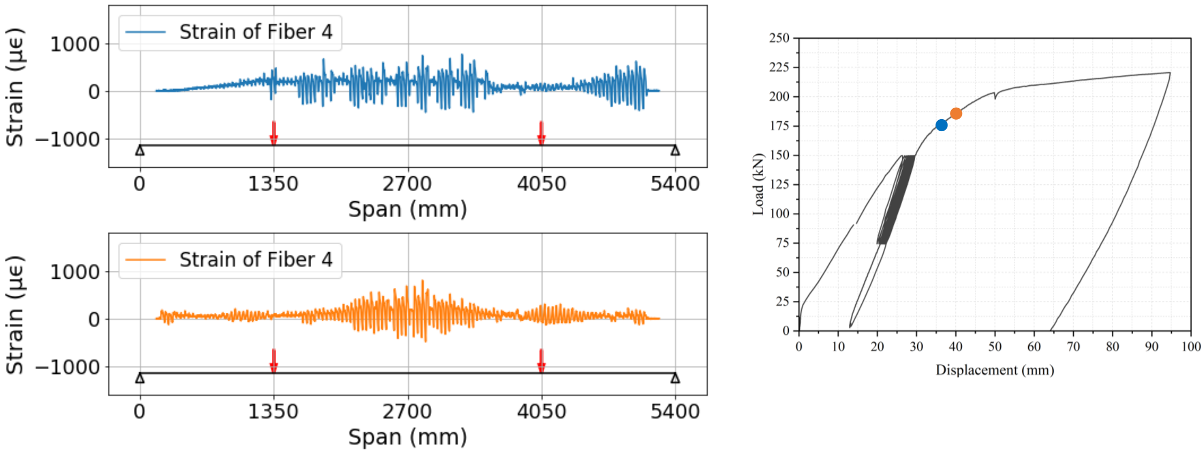

*Figure C.14. The strain data of Fiber 4 at two load levels of Slab 6 (left), and the load-displacement curve of Slab 6 (right).*

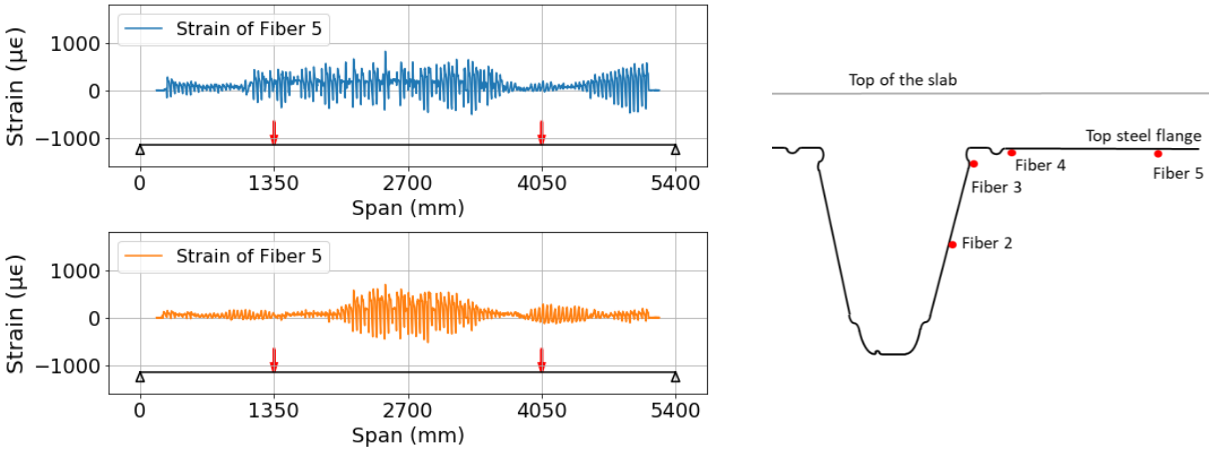

*Figure C.15. The strain data of Fiber 4 at two load levels of Slab 6.*

# D. Appendix: Crack detection

Firstly, the strain data of the left side of Slab 7 is illustrated in Figure D.1, it shows the strain data and the selected peaks of Fibers 11.1, 11.2, 11.3, 11.4, and 11.5. The locations of these fibers are highlighted in the cross-section of Slab 7 in Figure D.2.

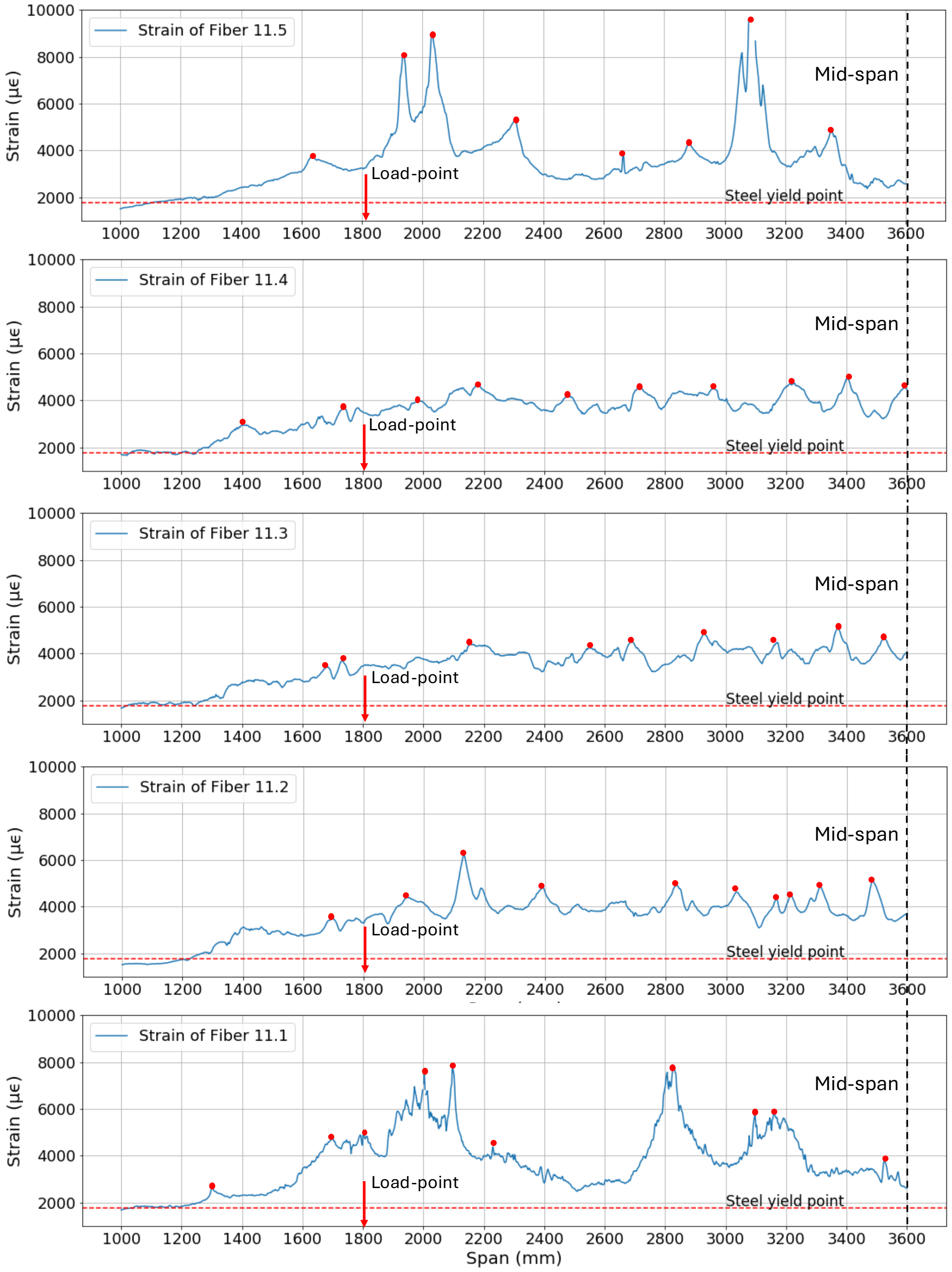

*Figure D.1. Peak detection of the left side of Slab 7, for Fibers 11.5, 11.4, 11.3, 11.2, and 11.1.*

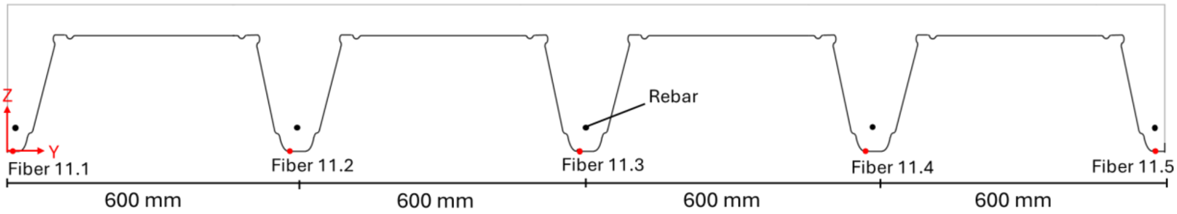

*Figure D.2. Cross-section of Slab 7.*

The peak detection of the right side of Slab 7 is illustrated in Figure D.3, it shows the strain data of Fibers 11.5, 11.4, and 11.3. It should be noted that the strain on the y-axis of Fiber 11.5 is larger than for Fibers 11.4 and 11.3, this is done to keep the peaks of Fibers 11.4 and 11.3 visible.

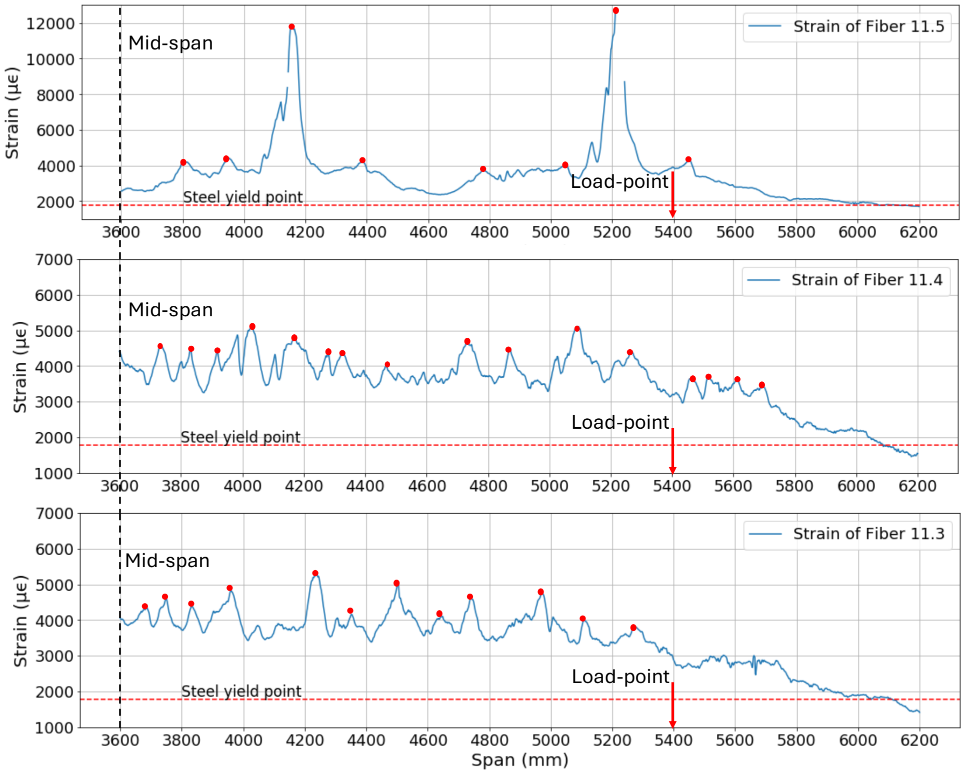

*Figure D.3. Visual peak detection of the right side of Slab 7, for Fibers 11.5, 11.4, and 11.3.*